Reading the climate signals hidden in bauxite

Beatrix Heller, Silvana Bressan Riffel, Thierry Allard, Guillaume Morin, Jean-Yves Roig, Renaud Couëffé, Geoffrey Aertgeerts, Alexis Derycke, Claire Ansart, Rosella Pinna-Jamme, et al.

Available online at www.sciencedirect.com

ScienceDirect

Geochimica et Cosmochimica Acta 323 (2022) 40–73

Geochimica et Cosmochimica Acta

www.elsevier.com/locate/gca

Reading the climate signals hidden in bauxite

Beatrix M. Heller [a,b,*], Silvana Bressan Riffel [a,c], Thierry Allard [b], Guillaume Morin [b], Jean-Yves Roig [d], Renaud Couëffé [d], Geoffrey Aertgeerts [e], Alexis Derycke [a], Claire Ansart [a], Rosella Pinna-Jamme [a], Cécile Gautheron [a]

[a] GEOPS, Université Paris Saclay, CNRS, Bat. 504, 91405 Orsay cedex, France
[b] IMPMC, UMR 7590, CNRS, Sorbonne Université, MNHN, IRD, 4 place Jussieu, 75252 Paris cedex 05, France
[c] UFRGS, Federal University of Rio Grande do Sul, Av. Bento Gonçalves, 9500, Institute of Geosciences, 91509-900 Porto Alegre, Brazil
[d] BRGM, 3 avenue Claude Guillemin, BP 6009, 45060 Orléans Cedex 2, France
[e] BRGM, Domaine de Suzini, BP 10552, 97333 Cayenne Cedex 2, France

Received 21 October 2021; accepted in revised form 15 February 2022; available online 22 February 2022

Abstract

The dynamics of tropical weathering through time with the formation and long-term evolution of laterite associated with climatic and geodynamic forcing is still a poorly explored issue. To better access this, we focused on lateritic-bauxitic duricrusts from the well-explored, 300 m high Kaw mountain in northeastern French Guiana. Macroscopically homogeneous Fe (oxyhydr)oxides-rich subsamples were separated from 10 bulk samples. Bulk- and subsamples were investigated by mineralogical and geochemical analyses and (U-Th)/He geochronology. The samples show a large heterogeneity on the macro- and microscopic scale reflecting different stages of duricrust formation and evolution through processes of dissolution and (re)precipitation of Fe (oxyhydr)oxides. The 284 (U-Th)/He ages obtained for goethite α-(Fe, Al)OOH and hematite α-Fe_2O_3 range from 30.5 ± 3.1 to < 0.8 Ma and show large variability within a sample. The oldest hematite and Al-poor goethite subsamples precipitated since 30 Ma and formed while kaolinite was stable. Precipitation of Fe-minerals increased since ~ 14–12 Ma but still happened under ferruginous lateritic, non-bauxitic conditions. The dissolution and (re)precipitation of Fe minerals, Al-substitution in goethite, and the overall enrichment in Th, as well as gibbsite precipitation indicate an intensification of weathering and a shift towards bauxitic conditions since the end of the Miocene. The Th-, U-, and Al-rich Fe phases formed in this late episode of intense weathering partially replace the oldest, often Th- and U-poor phases leading to a considerable age spread. We claim that this episode of intensified weathering, which had its peak at ca. 6–2 Ma, corresponds to the bauxitization of the lateritic cover of Kaw mountain.

Our proposed model of lateritization since at least 30 Ma and bauxitization since the late Miocene provides new constraints on the timescale and intensity of weathering at Kaw mountain. The onset of lateritization in French Guiana (Kaw region) is potentially older than ca. 30 Ma and was possibly synchronous with the development of bauxites in neighboring countries, and differences in the Paleogene weathering intensity might be due to different drainage capacities of the parental material. Late Neogene bauxitization suggests a regional increase in precipitations and drainage potentially linked to increased incision owing to local uplift.

* Corresponding author at: GEOPS, Université Paris Saclay, CNRS, Bat. 504, 91405 Orsay cedex, France.
E-mail address: b-m.heller@gmx.de (B.M. Heller).

https://doi.org/10.1016/j.gca.2022.02.017
0016-7037/

Finally, we confirm that a detailed combination of geochronological results coupled to mineralogical and geochemical analyses improves our understanding of tropical weathering processes and duricrust formation by placing mineralogical and geochemical processes into a temporal framework.

Keywords: Weathering; (U-Th)/He geochronology; Laterite; Supergene; Goethite; Hematite

1. INTRODUCTION

Lateritic bauxites are weathering products in which Al and Fe accumulated, often forming economically important Al-deposits (Valeton, 1972; Bardossy and Aleva, 1990; Patterson et al., 1994; Carvalho et al., 1997). While classical laterites, deep stratified weathering profiles, often capped by a ferruginous duricrust but without important Al enrichment, form under tropical and subtropical climatic conditions commonly found at the Earth's continental surface, more specific conditions are required for bauxite formation (Prasad, 1983; Bardossy and Aleva, 1990; Schellmann, 1994; Tardy and Roquin, 1998; Valeton, 1999). Extensive studies linked to exploration activities and global comparison have shown that suitable climatic conditions with monsoonal seasonal variations and high precipitations are necessary (Bardossy and Aleva, 1990; Tardy, 1997; Tardy and Roquin, 1998). Thus, the potential process leading to bauxites is favored in equatorial regime but they can be found in broader intertropical latitude (Bardossy and Aleva, 1990). Iron-rich/ferruginous laterites form preferentially under more seasonally contrasted monsoonal (sub) tropical climate, whereas aluminum-rich/ bauxitic laterites (referred to as bauxites) require generally a more humid, less contrasted tropical climate (Tardy et al., 1991; Tardy, 1997; Tardy and Roquin, 1998). In addition, specific drainage conditions with high permeability of the host rock and strong dissection of the surface are also essential for the formation of bauxites (Bardossy and Aleva, 1990). Ferruginous and bauxitic laterites are thus archives of past climate and landscape (Tardy and Roquin, 1998), containing information on the evolution of the continental surfaces, especially in areas of tectonic quiescence prone to weathering (e.g., Allard et al., 2018; Balan et al., 2005; Monteiro et al., 2014, 2018; Riffel et al., 2015; Vasconcelos et al., 2019, 1994).

However, several aspects of their genesis are not well understood and there is a lack of time constraints for their formation, evolution and relation with climatic change, mostly because absolute dating of bauxites remains a challenging task. Whenever ferruginous laterites and bauxites are covered by sediments, they can be dated indirectly by determining the age of the under- and overlying formations, whereas dating of uncovered weathering surfaces is more complicated.

The mineralogy of ferruginous laterites and bauxites is rather simple, consisting mainly of secondary minerals such as kaolinite, iron oxides and oxyhydroxides, and aluminum hydroxides. However, these minerals are not suitable for conventional geochronological methods. K-Ar and ^{40}Ar-^{39}Ar dating of manganese oxides was used in numerous studies of lateritic duricrusts (see e.g. Vasconcelos et al., 1994, 2015; Ruffet et al., 1996; Vasconcelos, 1999; Beauvais et al., 2008; Vasconcelos and Carmo, 2018). This method requires K-bearing phases such as some Mn oxides, but such minerals are rare in laterites, in contrast to Fe oxides sensu lato, kaolinite, or gibbsite. Paleomagnetic dating of the ferruginous parts of the profiles is possible but becomes very imprecise when the latitudinal shift of the target area was insignificant during the time interval of interest. Goethite and hematite, the main constituents of the Fe duricrust (Tardy, 1997), which is equally present in most bauxites (Bardossy and Aleva, 1990), can be dated using the (U-Th)/He method as they quantitatively retain He at Earth surface conditions as shown by ^{4}He and ^{4}He/^{3}He diffusion experiments and ab-initio calculations (Shuster et al., 2005; Heim et al., 2006; Vasconcelos et al., 2013; Reiners et al., 2014; Balout et al., 2017; Deng et al., 2017; Hofmann et al., 2017; Farley, 2018). This approach has been used by a growing number of studies over the last three decades, but uncertainty remains on some essential aspects such as the diffusion parameters of He in goethite (Lippolt et al., 1998; Pidgeon, 2003; Pidgeon et al., 2004; Shuster et al., 2012; Danišík et al., 2013; Vasconcelos et al., 2013; Monteiro et al., 2014, 2018; Riffel et al., 2016; Hofmann et al., 2017; Allard et al., 2018; Wells et al., 2019). In pedogenic iron duricrusts, the petrological relationship between the different phases is often very complex due to multiple cycles of dissolution of previously formed phases followed by reprecipitation (Nahon, 1991; Tardy, 1997). Geochronological analysis of this material thus requires an understanding of the relationships between the target phases (Monteiro et al., 2014).

The Kaw Mountain ridge in northeastern French Guiana is covered by a thick weathering profile first discovered in the 19th century (Leprieur, 1848). An extensive exploration campaign in the 1950s revealed the existence of a large, though uneconomic, bauxitic Al deposit with ca. 42 Mt of Al-ore with 42 wt% Al on average (Choubert, 1956). The area has been tectonically stable and in intertropical latitudes at least since the Cretaceous. Geomorphological studies estimate an Oligocene to Miocene age for this paleosurface (Choubert, 1957; Blancaneaux, 1981), and a paleomagnetic study indicates an Eocene age (Théveniaut and Freyssinet, 2002). Note however, that peneplanation, lateritization, and bauxitization might have happened over a long time interval (Bardossy and Aleva, 1990). In this context, the timing of the bauxitization of this surface remains unclear.

In this study we combine (U-Th)/He dating of iron (oxyhydr)oxides from the lateritic-bauxitic iron duricrust of

Kaw mountain with detailed high resolution mineralogical and geochemical analyses. Our data reveal a complex story of precipitation, dissolution, transformation, and mixing processes in a very active weathering system. Despite some substantial age spreading which will be discussed in detail, the careful analysis of the dataset allows determination of periods with enhanced Fe mineral precipitation, enables insights into variations of the weathering intensity and thereby into the bauxitization process.

2. GEOLOGICAL, GEOMORPHOLOGICAL AND CLIMATIC CONTEXT

2.1. Geological history of the Guiana shield

The Amazonian craton forms the core of the South American continent and is composed of two parts, a northern one called Guiana shield and a southern one, called Brazilian or Guaporé shield, that are divided by the Amazonas-Solimões Basin, which hosts the world's largest river, the Amazon (see Fig. 1A). Apart from minor Archean cores, most of the craton was formed during the Paleoproterozoic Trans-Amazonian orogeny (ca. 2.2–1.95 Ga) and later Paleo-, Meso-, and Neoproterozoic accretionary events on its southwestern border (Cordani and Teixeira, 2007). After the Panafrican/Brasiliano orogeny at the end of the Neoproterozoic, the Amazonian Craton was located next to the West African craton, where it remained until the Mesozoic opening of the Atlantic. During the Paleozoic, marine and terrestrial sediments were deposited in a huge E-W intracontinental rift known as the Amazonas-Solimões Basin which was episodically filled later, during Cretaceous and Cenozoic times.

Low-temperature thermochronological data from the Northeastern part of the Guiana shield indicate that the basement rocks have been near the surface since ca. 90 Ma (Derycke et al., 2021). In the Guiana basin, the coastal sedimentary basin at the northeastern rim of the shield, sediments started to deposit in the Cretaceous on top of the Precambrian basement (Wong, 1994). In the onshore part of this basin (coastal plains of Guyana, Suriname and French Guiana), Paleocene to Early Eocene sediments were deeply weathered during the Late Eocene and Oligocene, leading to the formation of the coastal bauxites (Hammen and Wymstra, 1964; Wymstra, 1971; Bardossy and Aleva, 1990; Wong, 1994; Monsels and Van Bergen, 2019), and producing the "Bauxite Hiatus" in the sedimentary sequence of the Guiana basin, but afterwards sedimentation continued during the Cenozoic.

West of the Guiana shield uplift of the Andes started in the early Cenozoic but mountain building first peaked by the Late Oligocene to Early Miocene (~23 Ma) and was most intense during Middle to Late Miocene (~12 Ma) and Early Pliocene (~4.5 Ma) (Hoorn et al., 2010; Sundell et al., 2019). Closure of the Panama Isthmus occurred at ~3.5 to 2.7 Ma (Coates, 1992; Bartoli et al., 2005). A large foreland basin developed where sediments from the Andes started to accumulate. However, until the Late Miocene the drainage system was different from todays and the Acre and Solimões basins were drained towards the Northwest. Establishment of the drainage towards the east, a process called transcontinentalisation, occurred definitively around ca. 9–8 Ma, leading to the development of the Amazon Fan located in the North of the mouth of the Amazon (e.g. Figueiredo et al., 2009; Hoorn et al., 2017). Since then, more than 4000 m of sediments accumulated in the Amazon fan, more than the half

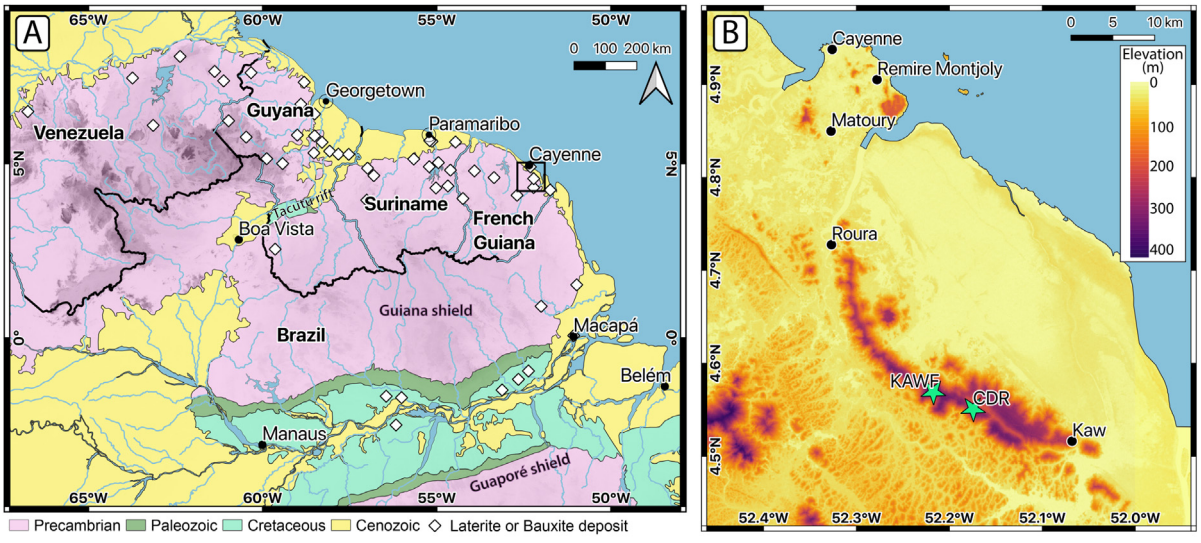

Fig. 1. (A) Geological map of the Guyana Shield (after Gómez et al. (2019) modified according to Mendes et al. (2012) and Baker et al. (2015)) with documented laterite and bauxite deposits (white diamonds, after Bardossy and Aleva (1990)). The underlying Digital Elevation model indicates the relief (dark = high). (B) Digital Elevation model of northeastern French Guiana with Kaw mountain ridge (between Roura and Kaw) and sampling locations (stars).

of them during the last 2.4 Myr, loading an enormous weight on the plate (Figueiredo et al., 2009).

2.2. Geomorphology of the Guiana Shield

The Guiana Shield has a slightly domed structure intersected by the Tacutu rift that separates an eastern and a western domain (Fig. 1). One of the geomorphological characteristics of the Guiana Shield is the occurrence of several planation surfaces, the most remarkable of these surfaces are the so called "tepuis" in Venezuela, flat table mountains with elevations of > 2000 m (Briceño and Schubert, 1990). All high elevation surfaces > 1000 m of the Guiana shield are only recognized west of the Tacutu rift. Geomorphological studies on the Guiana shield and the South American platform propose the existence of several surface planation levels with different ages of peneplanation from late Cretaceous to Quaternary (Choubert, 1957; King, 1962; McConnell, 1968; Blancaneaux, 1981; Aleva, 1984; Bardossy and Aleva, 1990). According to these models high elevation surfaces are supposed to be older than low elevation surfaces. A good summary of surfaces, elevations and assigned ages for the Guiana Shield can be found in Bardossy and Aleva (1990) and Théveniaut and Freyssinet (2002). Note that assignment of the ages and elevations of these surfaces appears to be sometimes inconsistent when comparing different authors (Choubert, 1957; King, 1962; McConnell, 1968; Blancaneaux, 1981; Aleva, 1984; Bardossy and Aleva, 1990).

2.3. Weathering age constraints

Age constraints on paleosurfaces are mainly of relative nature. Stratigraphic relationships with sedimentary deposits are provided in Central Amazonia where most bauxites rest on (and so postdate) the Alter do Chão Formation considered to be late Cretaceous and early Cenozoic (Putzer, 1984; Hoorn et al., 2010). In Cenozoic coastal basins of Suriname and Guyana, bauxites developed on top of Paleocene to Early Eocene sediments are overlain by Oligocene to Miocene sediments (Hammen and Wymstra, 1964; Aleva, 1981; Bardossy and Aleva, 1990). Age dating by paleomagnetism indicates Eocene to recent ages for a number of lateritic covers in northern French Guiana (Théveniaut and Freyssinet, 1999; Théveniaut and Freyssinet, 2002). No other studies exist in French Guiana and all published geochronological literature is on the southern part of the Guiana shield and on the Guaporé shield. Allard et al. (2018) dated ferruginous duricrusts in western Amazonia developed on top of Precambrian intrusive rocks and Neogene sediments. Using (U-Th)/He geochronology of Fe oxides as well as electron paramagnetic resonance dating of kaolinites, they obtained Mid to Late Neogene ages. Mathian et al. (2020) obtained late Neogene and Quarternary ages on kaolinites from ferralsols and acrisols from the same area whereas Balan et al. (2005), who studied weathering profiles north on Manaus, obtained Early Paleogene to late Neogene kaolinite ages in weathered Alter do Chao sediments and soils located north of Manaus.

Several studies on absolute age dating of supergene Fe and Mn minerals exist for the Guaporé Shield (Vasconcelos et al., 1994; Ruffet et al., 1996; Shuster et al., 2005; Shuster et al., 2012; Monteiro et al., 2018; dos Santos Albuquerque et al., 2020), most of them from the Carajás area. Results cover a wide range of ages, mainly from 80 Ma to recent and exhibit discrete periods of intense weathering : the most common data are indicative of the Eocene, Early Oligocene, Middle Miocene, Pliocene, and Pleistocene and some older ages in the case of dos Santos Albuquerque et al. (2020). A ^{3}He exposure age of 7 Ma for the Carajás plateau indicates very slow erosion rates for that area (Monteiro et al., 2018).

2.4. French Guiana climatic condition

Nowadays, French Guiana is located in the tropics north of the equator and most of the country (including the study area) has a tropical rainforest climate ("Af") after the Köppen climate classification (Beck et al., 2018), defined by > 60 mm precipitation in the driest month. At sea level the mean annual temperature is equal to or above 25 °C and the difference between mean temperatures of the warmest and coolest months does not exceed 5 °C. While temperatures are rather constant and similar over the Guianas, precipitation shows a large variability in this region (Bovolo et al., 2012). French Guiana has two rainy seasons, one from May to June/July and another one in December and January. The main dry season is from July to November; from February to April rain is reduced but French Guiana lacks a second dry period (Bovolo et al., 2012). The Northeast of French Guiana is the most humid area of the country with mean annual precipitations exceeding 3000 mm, locally, notably in the area of Kaw, exceeding 4000 mm (Groussin, 2001; Bovolo et al., 2012; Ringard et al., 2015).

3. KAW MOUNTAIN GEOLOGY AND SAMPLING

3.1. Kaw mountain study area: geology, geomorphology and paleomagnetic data

The Roura-Fourgassié-Kaw mountain ridge (in the following referred to as Kaw mountain) is a ~ 40 km long, 200–320 m elevation convex-shaped ridge in northeastern French Guiana (Fig. 1B). It stretches SE-NW parallel to the coastline at ~ 20 km inland. Its basement is composed of acid to intermediate metavolcanites of the Paleoproterozoic Paramaca unit (2.14–2.16 Ga) (Delor et al., 2003), metamorphosed under greenschist metamorphic conditions and affected by subvertical banding. The top of the ridge is capped by a thick lateritic-bauxitic cover which is very heterogeneous with strong variations in thickness, color, texture and composition (Choubert, 1956). The mean composition is 42 wt% Al_2O_3, 30 wt% Fe_2O_3, 4 wt% TiO_2, 1.7 wt% SiO_2, 22 wt% H_2O for the 42 Mt bauxite reserve, but extreme values of the Al-Fe rich crust range from white bauxite with 64 wt% Al_2O_3 and 1.5 wt% Fe_2O_3 to Fe-laterite with 6 wt% Al_2O_3 and 60 wt% Fe_2O_3 (Choubert, 1956; Blancaneaux, 1981). Gibbsite is the main Al-

mineral, whereas boehmite is rare. A drilling close to Camp Caiman revealed 20 m of bauxite overlying (at least) 50 m of clays and saprolite, and reached the altered rock at a depth of 70 m (bottom of the drilling). According to Choubert (1956), the mean thickness of the bauxitic crust is 5.5 m, but higher thicknesses up to 20 m were observed, especially close to the rim of the plateau, at cliffs, and at long angle slopes. Choubert (1956) observes a link between the schistosity and bauxite thickness, with thicker bauxitic crust perpendicular to the schistosity (i.e. steep schistosity). Flanks of the Kaw Mountain expose stair-like morphology with lateritic steps, cliffs, numerous rolled blocks and entire slid shields are described. Caves, generally situated below the duricrust, are common. In flat areas, bauxite often appears as floats sat on clays (Choubert, 1956).

Choubert (1957) and later Blancaneaux (1981) assign the flat surface of Kaw mountain to the "second peneplain" or "surface II" for which they consider – based on large-scale geomorphological models – an Oligocene to Lower Miocene age, equivalent to the Early Velhas level of King (1962) in northern Brazil. The first published attempt of dating of the lateritic surface has been undertaken by Théveniaut and Freyssinet (2002) who did paleomagnetic dating of the iron duricrust at the top of the ridge. The authors obtained an Eocene to Miocene age for the weathering surface. Their interpretation of the Eocene age and the Miocene age corresponds to the actual paleosurface and to strong uplift during the last 10 Ma, respectively.

3.2. Bulk samples

Ten ferruginous duricrust samples from two transects were collected for the purpose of this study (Fig. 2). Sample locations and descriptions can be found in Table 1. The first transect descends the northern flank of the mountain ridge; four samples collected in situ at the surface (CDR-01-04) were sampled along a path called "Sentier d'observation des Coqs de roche" at elevations of 307–220 m. The second transect is west of the "CDR" transect and descends the southern flank of the ridge starting at "Camp Caiman" (Fig. 2). Six samples (KAWF-1 to KAWF-5 and KAW18-10B) were collected at elevations of 300–220 m. Two samples (KAWF-5 and KAW18-10B2) were taken at the top of the ridge, one sample (KAWF-4) was collected in the bed of a small creek which runs over a massive duricrust (Fig. 2). Descending the flank further down from the sampling point of KAWF-4, the small creek runs continuously over the duricrust (Fig. A1A of the Electronic Supplement). Suddenly, at ca. 220 m elevation, the duricrust ends in a ca. 3.5 m high cliff producing a small waterfall with a

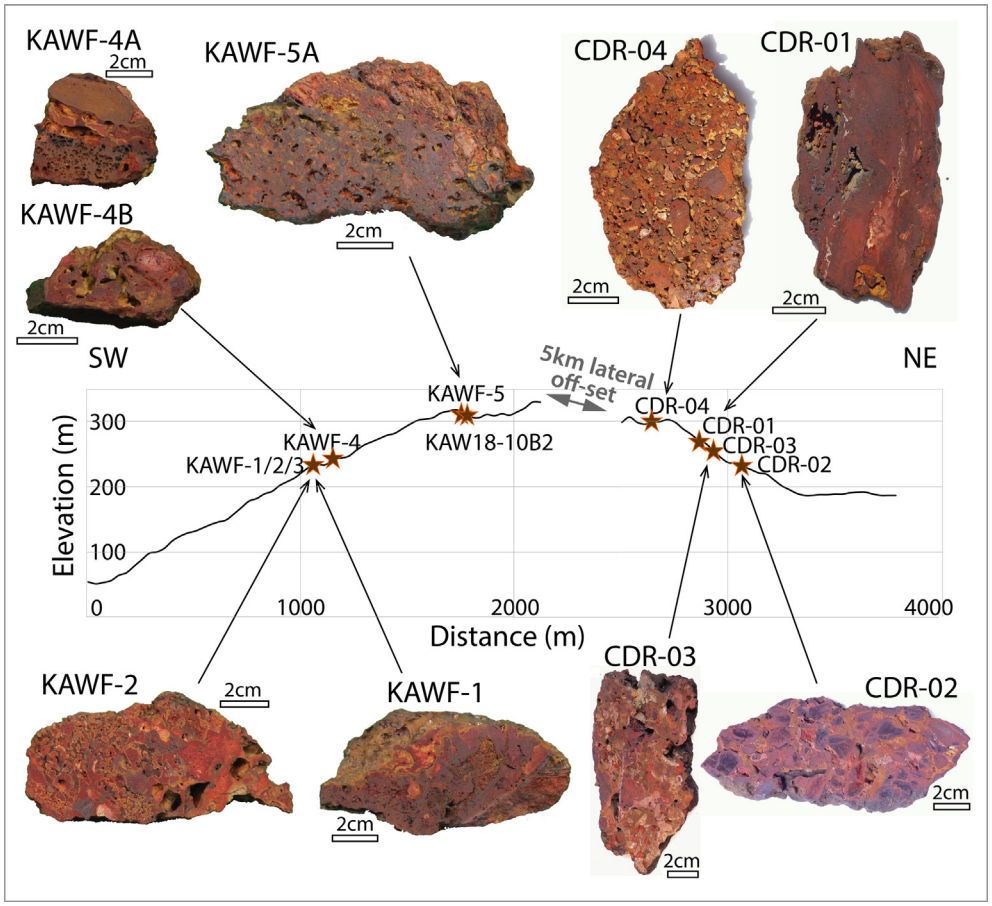

Fig. 2. Elevation profile of the two sampled transects on the northern (CDR) and southern (KAWF) flanks of the ridge (for locations see Fig. 1) with pictures of the analyzed samples.

Table 1
Sample locations and sample description.

Flank (transect)	Sample	Latitude (°)	Longitude (°)	Elevation (m)	Outcrop	Analyzed blocks	Description	Material used for bulk XRD and bulk chemistry
North (CDR)	CDR-01	4.55263	−52.17262	271	surface, in situ	CDR-01A CDR-01B	Massive, overall red sample. The matrix is fine grained, mainly dark red but locally beige-pink. Metallic, anthracite colored Fe minerals crystallized botryoidally in big voids. The outer surface of the sample is denser than the matrix and brownish black. The two blocks are very similar	slice of CDR-01A
North (CDR)	CDR-02	4.55482	−52.17158	222	surface, in situ	CDR-02	Composed of black cm-sized altered pisoliths cemented in a ochre-beige porous matrix. Towards their outer rim and along veins in their interior the pisoliths are often denser and more metallic. As for the other samples the outermost coating is denser and brown to black	slice of CDR-02
North (CDR)	CDR-03	4.55317	−52.17230	256	surface, in situ	CDR-03	Vermiform to massive, sometimes slightly pisolitic structure. The colors range from red-violet, to ochre, beige and greenish-beige. The beige parts of the matrix are often less consolidated than the rest of the sample. The densest parts of the sample are red-violet domains which are sometimes more blackish towards the rims and resemble similar ones observed in sample CDR-04C.	slice of CDR-03
North (CDR)	CDR-04	4.55095	−52.17452	307	surface, in situ	CDR-04A	Nodular/pisolitic structure. Red to blackish and orange nodules and pisoliths of varying size (0.1–2 cm) are cemented in an extremely porous fine-grained matrix colored from beige to ochre and brown. Sometimes the nodules are coated and cemented by a black glassy layer	slice of CDR-04A
						CDR-04C	More massive structure than CDR-04A, dominating color is red. Beige ochre fine grained domains coexist with red to red-violet finely porous matrix. Blackish denser veins and coatings crosscut the matrix and delimitate the different domains. Rarely reddish-black micropisoliths / nodules exist.	slice of CDR-04C
South (KAWF)	KAWF-1	4.56364	−52.21750	220	from side of giant bloc (ca. 4x6x3m) next to waterfall, ca. 1 m above ground	KAWF-1	Massive structure dominated by a red matrix. Locally the matrix is yellow or dark brown, clear boundaries are often not visible. Inside a small cavity, glassy black, at the surface yellow orange, botryoidal minerals crystallized	pieces of slice of KAWF-1
South (KAWF)	KAWF-2	4.56364	−52.21750	220	at cliff next to waterfall, ca. 2 m below surface, in situ	KAWF-2	Red-yellow sample with a rather nodular structure. mm-sized red dull nodules with a yellow rim are in a red to blackish red, sometimes red-whitish fine grained porous matrix. Locally red-blackish pisoliths or nodules of different size and porosity occur in the matrix. Big voids are often covered by a brown glassy coating.	slice of KAWF-2
South (KAWF)	KAWF-3	4.56364	−52.21750	220	surface, in situ, at head of waterfall	KAWF-3	The outer surface of the sample is made up by a thick dense dark gray coating with metallic luster. Inside it has a massive structure with dull red and yellow domains which resemble the "taches" described by Tardy (1993) for the "horizon tacheté" (mottled zone)	several cm-sized pieces of KAWF-3

South (KAWF)	KAWF-4	4.56406	−52.21775	250	surface, in situ, from bed of a small creek which runs over massive duricrust (material broke into small pieces during sampling)	KAWF-4A	Ochre-reddish and very porous sample containing pores of different sizes. Red bean shaped domains of different porosity and hardness, sometimes yellow at their rim alter with ochre brown domains of different forms. The latter are either more dense but not very hard or harder, very porous with many big pores (mm sized) and matrix-character. Some big voids are filled with white rather unconsolidated material.	several cm-sized pieces of KAWF-4
						KAWF-4B	Massive to slightly pisolitic structure with big voids. Sample is dominated by a red matrix with yellow veins and coatings. Locally the matrix is red-whitish and less consolidated.	
South (KAWF)	KAWF-5	4.56875	−52.21766	300	surface, in situ or big bloc	KAWF-5A	Sample 5A has one pisolitic part where small micropisoliths of ca. 0.1–0.3 cm size are cemented in a orange-ochre fine grained matrix. Locally they are additionally cemented by a black dense glassy phase. The pisolitic part of the sample grades into a matrix dominated part where a poorly consolidated fine grained orange-red-yellow matrix is crosscut by black glassy to metallic veins.	slice of KAWF-5A
						KAWF-5B	KAWF-5B is similar to the matrix dominated part of KAWF-5A. Towards the outer surface the material is black, massive hard and dense with some small pores and locally bright veins crosscutting.	slice of KAWF-5B
South (KAWF)	KAW18-10_B2	4.56897	−52.21697	300	10 cm below surface	KAW18-10_B2	Composed of 0.5–1.5 cm-sized black pisoliths sampled at 10 cm depth from a pisolith-nodule-soil mixture. Reddish more porous and edgy nodules were equally present in the same horizon but were not analyzed here. Two pisoliths which are black and dense at the surface and red-violet to orange at the inside were used for geochronological analyses. Three other pisoliths with the same outer aspect were used of mineralogical and geochemical analysis.	several pisoliths separated from matrix (not presented)

pond at its base (Fig. A1B of the Electronic Supplement). Two samples, KAWF-3 and KAWF-2, which represent different parts of the duricrust, were taken at this spot (Fig. 2 and Fig. A1B). Another sample, KAWF-1, was sampled at the other side of the pond from a giant duricrust block of ca. 4 m × 6 m × 3 m (Fig. 2). The sample was taken about 1 m above the ground. Although this block is probably not in situ we assume that due to its immense size it has not been turned around or transported very far.

4. METHODS

4.1. Bulk sample analyses

4.1.1. Petrological observations

For petrological observations and subsequent analyses, bulk sample blocks (mainly dm-sized) were sawed into several 1–2 cm thick slices. For samples where more than one block was analyzed, notably those which broke into smaller pieces during sampling in the field, each block was given a specific name (letter after sample number, e.g. KAWF-5*A*). The slices were observed using a hand lens and a binocular microscope and different mineralogical phases and subsamples of Fe-minerals (in the following always referred to as subsamples) were identified and described. Generally, one slice (or several small pieces in the case of broken samples) was used for bulk analyses. A schema visualizing the preparation procedure can be found in Fig. A2 of the Electronic Supplement.

4.1.2. X-ray diffraction

Sample slices/pieces were crushed in a steel and subsequently finely ground in an agate mortar. The material was loaded in hollowed inox sample holders (32 mm diameter and 3 mm depth) and the sample surface was leveled using a rough glass plate in order to limit preferential orientation. Powder X-ray diffraction (XRD) analyses were performed at the IMPMC laboratory, Paris, France, with a Panalytical™ XPert-Pro® Diffractometer equipped with an X'Celerator® detector. Powder data were collected in Bragg-Brentano geometry using Co-Kα radiation counting in continuous mode over the 3-110° 2θ range with an angular step of 0.01670° for 4 h. The powder XRD patterns were refined by the Rietveld method using the XND code including anisotropic pseudo-Voigt line-shape parameters (Berar and Baldinozzi, 1998). Crystal structures data reported by Blake et al. (1966), Forsyth et al. (1968), Saalfeld and Wedde (1974), Bish and Von Dreele (1989), Horn et al. (1972), Shintani et al. (1975), and Corbató et al. (1985) for hematite, goethite, gibbsite, kaolinite, anatase, rutile and boehmite respectively, were taken as starting parameters for the refinements. In the XND code, structure factors were corrected for anomalous scattering factors calculated from Cromer (1983). Scale factors and line-width parameters were refined for all phases, while unit-cell parameters were refined for goethite, hematite, anatase and rutile only. Although they were not further interpreted in the present study, anisotropic line-width parameters were freely refined for goethite and hematite in order to take into account for anisotropy of the crystallite shapes (Fritsch et al., 2005; Dublet et al., 2015), which was required to correctly match observed line-shapes. Once a satisfying fit (with small weighted profile R-factor (R_{wp}), see Toby (2006)) was obtained, the weight-fraction $w(p)$ of each phase p was calculated from its refined scale factor using the classical formalism by Snyder and Bish (1989) and assuming $\sum w(p) = 1$. The ratio of hematite to goethite (RHG) was calculated as RHG = hematite/(hematite + goethite). Al for Fe substitution rate in the goethite structure was calculated by applying the linear regression of Schulze (1984) to the Rietveld-refined value of the *c* unit-cell parameter (*Pbnm* space group), the *c* dimension being the less sensitive to non-stoichiometry in goethite (Schulze, 1984; Wolska and Schwertmann, 1993). Al-substitution rates of hematites were too low in the samples studied to be accurately determined from the *a* unit-cell parameter, owing to the effect of non-stoichiometry on the hematite unit-cell dimensions (Stanjek and Schwertmann, 1992). Although this parameter value was not interpreted in the present study, the site occupancy factor of the Fe site was freely refined for goethite and hematite to account for both Al for Fe substitution and non-stoichiometry, which was necessary to correctly match observed intensities (Stanjek and Schwertmann, 1992; Wolska and Schwertmann 1993). Uncertainties on our reported Al mol% values in goethite includes the uncertainty on the refined *c* value plus the ± 2.6 mol% uncertainty reported by Schulze (1984) on the regression.

4.1.3. Geochemical analyses

Major and trace elements including rare earth element content were obtained on bulk samples on the same material as used for the XRD analyses. The analyses were performed on 1–2 g of material ground to < 100 μm at the Service d'Analyse des Roches et des Mineraux (SARM), Vandoeuvre-Les-Nancy, France. Major elements (and Sc) were determined by ICP-OES iCap6500, trace elements by ICP-MS iCapQ after alkali fusion. Analytical uncertainties vary from < 2% to 25% for major element concentration from > 10 wt% to < 0.05 wt% and from < 5% to 20% for trace element concentrations between 100 μg/g and 0.1 μg/g. Further analytical details can be found at www.sarm.cnrs.fr.

4.2. Analyses on separated subsamples

In each bulk sample, several distinct facies, showing apparently homogeneous texture, color, hardness and porosity were identified. Those were separated by microdrilling using a Dremel multi tool, gently crushed in a steel mortar in order to obtain 0.1–2 mm sized fragments and then cleaned in ultrasound with MilliQ water and Ethanol. Single grains were then selected and handpicked under a binocular microscope for mineralogical and geochronological analyses. Each of these individual subsamples was assigned a systematic name consisting of the bulk sample (profile + number), the block of sample (if more than one piece was sampled), the type of phase, ranging from the assumed oldest to the assumed youngest (number) and a letter for the specific subsample. Individual subsample fragments are here referred to as grains. A table containing the

descriptions of all separated subsamples is reported in the Electronic Supplement (Table A1).

4.2.1. Scanning electron microscopy analyses and reflected light microscopy

Representative hematite and goethite grains of all subsamples were mounted in epoxy resin discs, polished, and investigated using reflected light and Scanning Electron microscopes (SEM). All subsamples were observed under reflected light. SEM analyses were performed using a Zeiss ULTRA55 microscope coupled to an EDS (Bruker QUANTAX) at the IMPMC, Paris. High resolution secondary electron and backscattered electron mappings (pixel size = 120 nm) were obtained from 30 subsamples using the software ATLAS (Zeiss). These mappings were used to identify the paragenesis, subsample texture and homogeneity of the Fe phases and to check systematically for mineral inclusions such as zircon or rutile. In selected areas major elements were quantified and element distribution maps were obtained using the EDS system.

4.2.2. Subsample XRD analysis

X-ray diffraction patterns of subsamples were obtained in two ways: i) by powder diffraction of finely crushed handpicked grains using the same measurement settings as described for the bulk samples (see above) but scanning over the 3-120° 2θ-range and counting for 6 h (done for 4 subsamples) and ii) by analyzing individual handpicked grains (done for 67 grains from 30 different subsamples) in Debye-Sherrer geometry using Mo $K\alpha$ radiation. For this latter analysis, a single grain of 250–700 μm size (ca. 20–100 μg) from selected subsamples was inseted into a boron silicate glass capillary (0.3–0.5 mm diameter) and analyzed at IMPMC laboratory, Paris, using a MM007HF RIGAKU rotating Mo anode (1.2 kV) delivering a 100 μm-width micro beam. For each subsample, 1 to 5 grains were analyzed. Two-dimensional XRD patterns were collected for 45–60 minutes in Debye-Scherrer geometry using a R-axis IV++imaging double plate detector (300 × 300 mm), the distance between the sample and the detector plate was 200 mm. Angle calibration and image integration to convert the 2D- into a 1D pattern were done using the FIT2D software (Hammersley, 2016). For 32 of the individual grains (generally one per subsample) the diffractograms were refined by the Rietveld method using the same XND code and procedure as described for the bulk samples. RHG and Fe-Al substitution in goethite were calculated as for the bulk samples.

4.2.3. (U-Th)/He geochronological analysis

Microscopically pure single grains of 250–700 μm size were handpicked under a binocular microscope and filled individually into 1x1 mm Nb capsules (purity 99.95%) for the (U-Th)/He analysis. 4 to 10 aliquots were analyzed per subsample. By weighing the empty and the filled Nb tubes the weight of the oxide grains was determined (10–250 μg, median = 63 μg). Degassing and analysis of the He content were conducted with two He extraction lines at GEOPS laboratory Orsay, France, coupled to (i) a Quadrupole mass spectrometer (QuadStar Pfeiffer, used for 237 of 284 analyses) and (ii) a VG5400 magnetic sector mass spectrometer, (used for 47 of 284 analyses). Each capsule was filled into a copper (Quadrupole line) or inox (VG line) planchet containing 49 positions (Gautheron et al., 2021). 8 capsules with fragments of the Durango apatite age standard and 3 capsules of a goethite internal standard, which serves as U and age standard, were measured with the oxides in each planchet, 1 Durango every 7 samples. Each capsule was heated during 30 minutes at a temperature < 1000 °C (up to a barely visible light glow of the capsule) using an IR diode laser. The temperature was regularly checked in order to avoid U volatilization as this has been described by Hofmann et al. (2020) and Vasconcelos et al. (2013). Examples indicating that no significant U loss seems to have affected our samples can be found in Fig. A3 of the Electronic Supplement. For details on the degassing protocol see Gautheron et al. (2021).

For U and Th analyses the iron oxyhydroxide grains (including the Nb capsules) were filled into Teflon vials and digested during 24 h on a 100 °C hot plate using an acid mixture of 50 μl of HNO_3 5 N, 50 μL of a ^{235}U, ^{230}Th and ^{149}Sm spike in HNO_3 5 N, 400 μL 48% HCl ultrapure and 100 μL 30% HF ultra-pure. Afterwards the solutions were evaporated to dryness (3 h at 100 °C) and redissolved in 1.9 mL HNO_3 1 N (1 h at 100 °C). 1.5 mL of solution were taken and transferred to polypropylene vials where they were re-diluted with 500 μL HNO_3 1 N. Durango fragments degassed with the Fe oxides were dissolved according to the protocol described by Gautheron et al. (2021).

U, Th and Sm analyses were performed on a ThermoFisher Element XR HR-ICPMS at GEOPS, Orsay, France or an Agilent ICP-QMS 7900 at IPGP, Paris, France and quantification was done by isotope dilution method. The analytical error for U, Th and He is 5% at 1 σ. For ages younger than ~ 0.8 Ma, the age determination is less accurate associated with the U-Th series disequilibrium that changes the He production rate (Farley, 2002). Because we used a ^{235}U and ^{230}Th spike adapted for the determination of age older than 0.8 Ma, no precise age can be calculated. We therefore only indicate that the ages are < 0.8 Ma (this concerns only 3 out of the 284 ages of our dataset).

As large fragments were used for (U-Th)/He dating, alpha ejection (loss of the alpha particles produced in the outer 15–25 μm of a crystal, for details see Farley et al. (1996)) is balanced by He implantation and no alpha ejection correction is necessary. The possible effect of He loss through ultrasonic cleaning was tested by comparing material of the same subsample cleaned for a long time (ca. 30 minutes or more) with material cleaned for a short time (2–5 minutes). There was no systematic difference in the obtained ages.

4.2.4. He diffusion loss correction

Supergene hematite and goethite are generally composed of crystallites that have a very small size in the 10 s to 100 s nm scale (e.g., Vasconcelos et al., 2013). Although several studies have shown, that, even for those small crystallite sizes, hematite and goethite can quantitatively retain He over geologic timescales (Shuster et al., 2005; Heim

et al., 2006; Vasconcelos et al., 2013; Balout et al., 2017; Deng et al., 2017; Hofmann et al., 2017; Farley, 2018), a certain proportion of the produced He is lost by diffusion. For microcrystalline hematite diffusive loss is expected to be ca. 2–5% (Balout et al., 2017; Farley, 2018), whereas microcrystalline goethite loses ca. 2–20% of its radiogenic He over short to moderate geological timescales (Shuster et al., 2005; Heim et al., 2006; Vasconcelos et al., 2013; Deng et al., 2017; Hofmann et al., 2017). As diffusion losses are different for hematite and goethite and not equally well characterized for the two minerals, we adapted the diffusion correction factor to the mineralogy of the subsamples. For subsamples composed mainly of hematite (RHG > 0.5), we applied a diffusion correction of 5% (i.e. adding 5% to the raw age) and an error of 10% (+analytical error if greater than this). For subsamples composed mainly of goethite (RHG < 0.5), we applied a diffusion correction of 10% as proposed by Shuster et al. (2005). We decided to use 15% error (+analytical error if greater than this) for goethite instead of 10% error proposed by Shuster et al. (2005), as the studies by Deng et al. (2017) and Hofmann et al. (2017) have shown that He diffusivity in goethite might be more complex than formerly expected and He losses might differ significantly between different types of goethite. Note that the applied errors largely exceed the analytical error of the He, U, Th, and Sm measurements (generally ca. 2–5%). Correction factors are given per aliquot in Table 3.

5. RESULTS

5.1. Mineralogy and geochemistry of bulk samples

The mineralogy quantification obtained with the XRD diffractograms is presented in Table 2. Sample KAW18-10B2 is left out, as the analyzed nodules do not represent the bulk sample. All samples contain hematite, goethite, gibbsite, and anatase in detectable amounts, while kaolinite, boehmite and rutile exist only in some of the samples in detectable quantities. The hematite-goethite ratio (RHG) ranges from 0.92 to 0.06 (Table 2). Gibbsite contents range from 2.9 to 34.4 wt%, anatase contents from 0.9 to 2.7 wt%. The widespread presence of gibbsite coupled to the absence of kaolinite indicates the bauxitic character of the samples. Al-substitutions in goethite range from 5 to 25 mol% (Table 2). Note that these are mean values for each sample and higher and lower values might occur in different parts of the samples. The amounts of hematite and goethite for the bulk samples are presented on Fig. 3A and highlight two distinct samples with extreme hematite or goethite amounts (CDR-01 and KAWF-5B, respectively).

The major element data of the analyzed samples are reported in Table 2. Fe_2O_3 and Al_2O_3 range from 55.1 to 81.2 wt% and 9.2 to 25.0 wt%, respectively, and are the major components. SiO_2 contents are very low, ranging from 0.3 to 4.4 wt%, similar to TiO_2 ranging from 0.9 to 3.1 wt%. P_2O_5 contents are up to 0.7 wt%, MnO contents up to 0.08 wt%. MgO, NaO and K_2O are generally below the limit of detection. The loss of ignition, mainly related to structural water of goethite, gibbsite and kaolinite ranges from 6.9 to 17.9 wt%. Fig. 3B shows the Fe_2O_3 and Al_2O_3 quantities of the analyzed samples, and a strong correlation between the Fe_2O_3 content and the Al_2O_3 content can be observed.

Analyses of U and Th can be found in Table 2, other trace elements and rare earth elements are reported in Table A2 of the Electronic Supplement.

5.2. SEM analyses

The SEM analyses reveal that some subsamples are relatively uniform (Fig. 4A-B), while many show complex textures, intergrowths, structures of redissolution, or different phases of precipitation (Fig. 4C-L). Selected typical SEM images are presented in Fig. 4 to illustrate the main petrological and mineralogical textures observed on the Kaw samples.

The SEM images show that in some subsamples all kaolinites have been dissolved and only phantoms of ancient kaolinites remain (Fig. 4D-E), while in other subsamples (especially those of KAWF-1) kaolinites of varying size are present and not dissolved (Fig. A4 of the Electronic Supplement). Hematite and goethite occur either as two separated phases seeming to have crystallized one after another (Fig. 4G-I) or are intimately connected eventually indicating processes of phase transformation (Fig. 4J-L). Element mapping shows that Al contents can vary a lot inside individual grains, with examples that are available in Fig. A5 of the Electronic Supplement. Some subsamples show minor zircon or rutile inclusions, but these minerals are generally rare and very small (up to 5 μm, mostly < 2 μm on the long axis). The eventual significance of these inclusions on the (U-Th)/He ages will be discussed further below.

SEM images and analyses reveal the complexity of the samples; what seems one phase at macroscopic scale is often a mixture of at least two phases and even more at microscopic scale. Often hematite and goethite, sometimes also anatase, kaolinite, and gibbsite appear in the same grains. Separation of these different phases for (U-Th)/He chronology is often not possible due to the small scale of the intergrowths. In these cases, mixed ages are expected to be obtained.

5.3. XRD analyses of subsamples

Results of the single grain XRD Rietveld analyses (Tables A3 and 3) show that the subsamples are in many cases composed of mixtures of hematite and goethite but pure phases also occur. Anatase is common in small amounts, whereas gibbsite, kaolinite, and rutile are rarely detectable in the selected subsamples. Al-substitutions in goethite range from 0 to 29 mol% and are similar to the values obtained for the bulk samples (Table 1).

5.4. (U-Th)/He dating

A total of 284 Fe oxyhydroxide grains were successfully dated by (U-Th)/He dating, with generally at least 4–5 aliquots per subsample. Data are reported on Tables 3 and A4

Table 2
Bulk compostion of the analysed duricrust samples.

		CDR-01	CDR-02	CDR-03	CDR-04A	CDR-04C	KAWF-1	KAWF-2	KAWF-3	KAWF-4	KAWF-5A	KAWF-5B
Hematite	wt%	75.5	62.1	39.4	19.5	33.5	32.3	33.2	36.1	33.6	17.0	5.0
abs. error	wt%	0.5	0.5	0.9	0.8	1.2	1.2	1.6	1.2	1.3	1.7	0.3
Goethite	wt%	7.0	26.5	34.4	70.5	29.8	54.5	39.4	42.1	54.3	53.8	82.6
abs. error	wt%	0.8	1.5	1.5	0.4	2.0	1.1	1.6	1.3	1.3	1.4	0.1
Gibbsite	wt%	14.7	8.8	23.5	7.0	34.4	2.9	23.7	17.0	9.5	27.7	11.9
abs. error	wt%	0.7	0.4	0.5	0.3	0.6	0.5	0.8	0.4	0.6	0.7	0.6
Anatase	wt%	2.8	2.7	2.8	0.9	2.4	1.4	1.2	1.5	1.4	1.5	0.6
abs. error	wt%	0.6	0.3	0.3	0.2	0.5	0.3	0.3	0.3	0.3	0.4	0.2
Kaolinite	wt%	bld	bld	bld	1.7	bld	8.9	2.5	2.1	0.3	bld	bld
abs. error	wt%	bld	bld	bld	0.3	bld	0.7	0.9	0.4	0.6	bld	bld
Rutile	wt%	bld	bld	bld	0.4	bld	bld	bld	0.8	0.6	bld	bld
abs. error	wt%	bld	bld	bld	7.2	bld	bld	bld	0.4	0.2	bld	bld
Boehmite	wt%	bld	bld	bld	0.1	bld	bld	bld	0.4	0.2	bld	bld
abs. error	wt%	bld	bld	bld	0.1	bld	bld	bld	0.4	0.2	bld	bld
RHG[1]	Hm/(Hm + Gt)	0.92	0.70	0.53	0.22	0.53	0.37	0.46	0.46	0.38	0.24	0.06
Gt *c* [2]	Å	3.0058	2.9906	2.9996	2.9920	3.0034	3.0048	2.9889	2.9813	2.9838	3.0150	3.0160
abs.error	Å	0.0179	0.0041	0.0042	0.0024	0.0053	0.0017	0.0038	0.0031	0.0029	0.0039	0.0024
Gt Al-substitution	mol%	11	19	14	19	12	11	20	25	23	5	5
abs. error	mol%	12.8	5.0	5.0	4.0	5.6	3.6	4.8	4.4	4.3	4.8	4.0
R^3_{wp}		0.018	0.013	0.017	0.010	0.022	0.015	0.015	0.013	0.014	0.019	0.017
Fe_2O_3	wt%	81.24	78.77	61.51	66.44	54.98	71.03	55.07	60.38	66.73	57.98	71.63
Al_2O_3	wt%	9.15	10.19	20.23	14.09	24.98	11.46	23.37	20.56	16.01	20.56	10.65
SiO_2	wt%	0.35	0.48	0.32	1.28	0.32	4.35	1.53	1.39	0.46	0.82	1.24
TiO_2	wt%	2.45	1.24	1.84	1.26	1.49	0.90	1.70	1.73	2.18	3.12	1.97
P_2O_5	wt%	0.10	0.15	0.15	0.23	0.15	0.73	0.14	0.17	0.17	0.22	0.38
MnO	wt%	0.02	bld	bld	0.07	bld	0.02	0.05	0.02	0.04	0.06	0.08
LOI[4]	wt%	6.86	9.37	15.59	16.46	17.92	12.25	18.26	16.20	14.56	17.35	14.60
U	µg/g	0.43	0.85	0.77	1.24	0.70	1.13	1.94	1.55	1.70	1.69	2.61
Th	µg/g	3.30	8.54	4.43	8.75	4.08	4.87	12.80	11.80	11.60	3.80	2.06

RHG[1]: ratio hematite goethite; Gt c^2: goethite unit cell c-parameter; R^2_{wp}: weighted profile R-factor (see Toby, 2006).

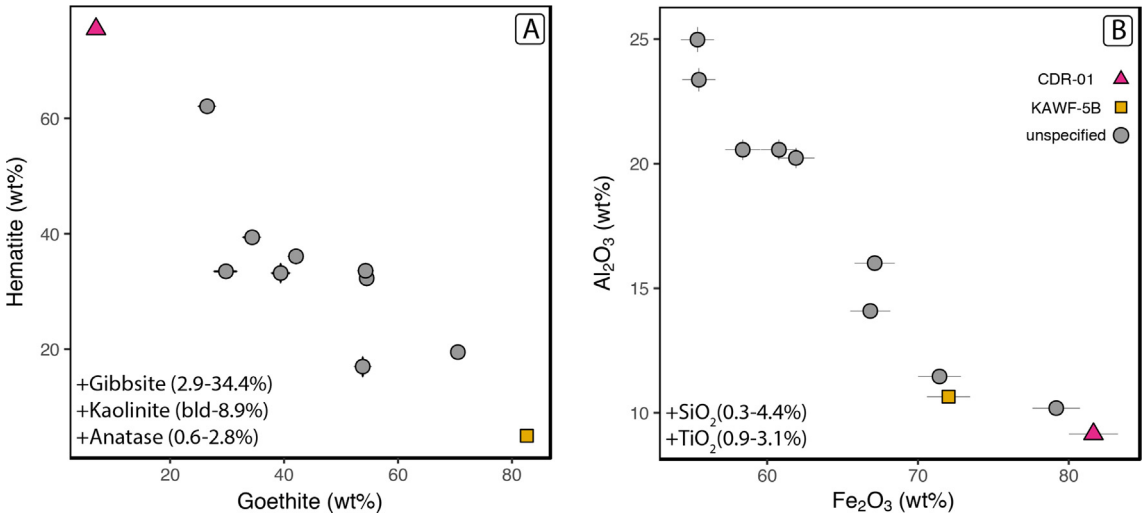

Fig. 3. Bulk data of the dated duricrust samples. (A) shows the amounts of hematite and goethite obtained through Rietveld refinement of the bulk XRD data, (B) shows the Fe_2O_3 and Al_2O_3 content from the geochemical analyses. The pink triangles correspond to sample CDR-01, the yellow squares to sample KAWF-5B, the grey circles to all other samples. For data see Table 2.

(Durango apatite data). In order to test the reproducibility of the results we dated up to 10 aliquots for some subsamples. Fig. 5 shows graphs of all obtained age data. The He ages corrected for diffusive loss range from 30.5 ± 3.1 to < 0.8 Ma and cover basically the entire range in between with a main peak at ca. 2 Ma. The oldest ages are all found on the northern flank of the mountain ridge with the oldest ages being obtained at the lowest elevation in sample CDR-02. On the southern flank the age distribution is more homogeneous with similar maximum ages of 12–15 Ma at all elevations.

For most analyzed (bulk) samples and subsamples, inter- and intra-subsample age range exceeds analytical uncertainty, varying from some to many percent (see Fig. 5A). Age distributions are different in every sample. U, Th, and Sm concentrations are generally low in the samples ranging from 0.05 to 5.2 ppm for U (median = 0.9 ppm), 0 to 33 ppm for Th (median = 6 ppm), and 0 to 6 ppm for Sm (median = 1 ppm). Fig. 5B and 5C present U and Th versus age graphs for the data set. A Th/U versus age graph for all samples as well as individual age vs U, Th and Th/U graphs for every sample can be found in Fig. A6A-D of the Electronic Supplement. Actinide concentration versus age trends differ in between the samples. While several samples (e.g., CDR-01, CDR-02, KAWF-4) show an enrichment in actinides towards younger ages this trend is inverted or more complex in other samples. Some subsamples show systematic variations of age with U or Th and selected examples will be presented in detail further down.

5.5. Detailed description of the (U-Th)/He, mineralogical and petrological results of two selected samples

The results of samples CDR-01 and KAWF-5 are presented in more detail, as those samples are characterized by extreme mineralogical, geochemical and geochronological features (Figs. 3 and 6). For all other samples, pictures of the samples indicating the dated subsamples and showing the obtained ages can be found in Fig. A7 of the Electronic Supplement.

5.5.1. CDR-01

Fig. 6A-D show a detailed portrait of sample CDR-01. Macroscopically this very hematitic (bulk analysis 75 wt% hematite, Table 2) sample is rather simple being composed of a fine-grained hematite-gibbsite matrix (subsamples CDR-01A_2 and CDR-01B_2, ratio hematite - gibbsite varies as macroscopically visible in color variations), some small cavities where botryoidal hematite crystallized (subsamples CDR-01A_3 and CDR-01B_3) and an outer coating composed of goethite (subsamples CDR-01A_1 and CDR-01B_1). The results from the two macroscopically very similar blocks are very coherent in terms of mineralogy (SEM), Th and U concentrations and (U-Th)/He ages and are thus treated together. Fig. 4A, 4D, 4I, and 4L show SEM images of the subsamples of sample CDR-01. The matrix is very fine-grained and rather homogeneous (Fig. 4D). Phantoms of kaolinite (i.e. holes with forms of kaolinite booklets indicating dissolved kaolinite) are visible suggesting that hematite formed while kaolinite was stable and possibly in equilibrium with kaolinite (Fig. 4D). In some voids large crystals of gibbsite crystallized seeming to post-date hematite crystallization. SEM images of the cavity fillings show that the botryoidal hematite that surrounds the matrix is very dense and pure (see Fig. 4A and 4I), and EDS analyses indicate that this botryoidal hematite contains less aluminum than the matrix. Some of the mounted grains of subsample CDR-01B_3 show a thin layer of fine-grained goethite coating the botryoidal hematite (see Fig. 4I).

Matrix and cavity filling (subsamples CDR-01A_2, CDR-01B_2, CDR-01A_3 and CDR-01B_3) yield similar, albeit rather spread, ages of mainly 25–10 Ma (Fig. 6A).

Geochemically they differ, with the cavity fillings being poorer in Th than the matrix. Note that it was very difficult to select pure grains of the botryoidal filling and often a small fraction of matrix was attached in the analyzed aliquots. The outermost coating (subsamples CDR-01A_1 and CDR-01B_1) yields clearly younger ages of 5.8 to 1.3 Ma and shows an enrichment in Th and U compared to matrix and cavity with a Th/U ratio similar to the matrix though (Fig. 6B-C-D). One aliquot from the matrix yields an age of 4.4 ± 0.7 Ma and has an U content more similar to subsample 1 (coating). The aliquots of subsamples CDR-01A_3 and CDR-01B_3 show an increase in Th towards younger ages (Fig. 6C and A8D), indicating either continuous precipitation under changing conditions or mixture with a younger phase richer in Th. We remark that that inside subsample 1 (coating) there is a tendency towards higher Th contents with younger age. The sample shows an overall increase in Th and U concentration towards younger ages (Fig. 6C, calculated correlation coefficients are given in Fig. A8 of the Electronic Supplement).

5.5.2. KAWF-5

Different from sample CDR-01, KAWF-5 contains very little hematite and is composed mainly of goethite and gibbsite (see Table 2 and Fig. 3A). Fig. 6E presents the two analyzed blocks which differ slightly in texture and bulk composition (see Tables 1 and 2). Fig. 4J and 4K show SEM images of subsample KAWF-5B_2AII. This subsample yields reproducible ages of 12.7 ± 2.0 to 10.0 ± 1.6 Ma. Interestingly the subsample is not very homogeneous on the microscopic scale. Anatase is common in this subsample (Table A3) and many of the analyzed grains present small concentric hematite pisoids which occur inside dense goethite or along phase boundaries (Fig. 4J and 4K). On the polished surface they appear as small craters which could either indicate a volume loss compared to the goethite or a polishing effect. They probably result from hydration of hematite into goethite. Al substitution in these goethite subsamples is low with ca. 5 mol% Al but higher than in the small hematite pisoids according to EDS analyses (Fig. A5B of the Electronic Supplement). Scarce kaolinite dissolution structures are visible in the goethite. The pisolith subsamples (KAWF-5A_1A and KAWF-5A_1B) are generally very fine-grained (Fig. 4C). They vary in porosity in between them but have rather homogeneous structures. Spherical textures are common and resemble those observed in other pisoliths of the other samples. Voids are filled with later hematite and goethite phases, and fragments containing parts of the pisolith cortex show transformation into goethite. Subsample KAWF-5B_1B shows very chaotic features. While some areas resemble those of the massive goethite grains, others have brecciated structures which are cemented by a fine-grained hematite matrix (Fig. 4H). Sporadically fine-grained porous hematite matrix is intergrown with fine grained gibbsite.

Fig. 6E-H show details of the dated subsamples from the two blocks of this sample. The ages range from 15 to 1 Ma but show some systematic differences from sample CDR-01. The oldest ages (8–15 Ma) occur all in goethite from more or less massive veins or coatings (KAWF-5A_3AII, KAWF-5B_2AII and KAWF-5B_3B). Pisoliths composed of hematite or a hematite-goethite mix yield younger ages ranging from 6.7 ± 0.7 to 2.5 ± 0.9 Ma (KAWF-5A_1A and KAWF-5A_1B). The youngest occur in vitreous goethite which cements /coats the hematite pisoliths (KAWF-5A_2A). Note that this vitreous goethite has different U and Th content than the older goethite subsamples. Different from most other samples, U contents decrease from old to young whereas Th contents cover the same range for all ages but are rather constant for each subsample (except KAWF-5A_2) (Table 3). Subsamples KAWF-5A_2B (slightly more brownish and less vitreous than KAWF-5A_2A) and KAWF-5A_2C (more metallic and porous, rather resembling pisolith material) were picked from the same separate as KAWF-5A_2A and might be mixtures between older massive veins, the pisoliths and the late vitreous goethite. The age versus U and age versus Th/U graphs (Fig. 6F and 6H and Fig. A9 of the Electronic Supplement) support this assumption.

Examples of age vs U and Th correlations of other (sub) samples are presented in Figs. A10 and A11 of the Electronic Supplement.

5.6. Relation of micro-XRD with chemistry and (U-Th)/ages

The micro-XRD results obtained on individual grains are compared to the U, Th and age data (bulk and from (U-Th)/He data) and reported in Fig. 7. The highest U contents occur in samples and subsamples with a RHG close to 0 (pure goethite), and subsamples with RHG close to 1 (pure hematite) have very low U contents (Fig. 7A, but note that there is also U-poor goethite). Th content correlates with Al-substitution in goethite with high Th concentrations occurring in Al-rich goethite (Figs. 7B and A12). Bulk samples and subsamples/grains show the same trends for U versus RHG and Th versus goethite Al-substitution.

The oldest ages correspond to rather pure hematite (RHG = 1) and, to a minor degree, goethite (RHG = 0) subsamples, whereas mixed subsamples (RHG around 0.5) are generally young (Fig. 7C and Table 3). Age correlates with the Al-content of goethite; towards younger ages goethite gets increasingly richer in Al (Fig. 7D and Table 3, one clear exception is botryoidal goethite from subsample KAWF-5CII which has ages of 9–5 Ma and lacks any Al).

Note that geochronological and mineralogical data were not obtained on the same aliquots. The mineralogical characterization by Rietveld refinement used 1–2 grains per subsample whereas (U-Th)/He data correspond to several (3–10) aliquots of each subsample. Therefore, the micro-XRD data does not represent the same diversity as the (U-Th)/He data which leads to the sometimes poorer correlation of the subsample/grain data compared to the bulk analyses.

6. DISCUSSION

6.1. (U-Th)/He age distribution

The (U-Th)/He ages obtained on the lateritic duricrust samples show a very broad distribution entirely covering

the range from the 30.5 ± 3.1 to < 0.8 Ma (Table 3), illustrating a long history of hematite and goethite precipitation. Interestingly, the ages often correlate with U and Th (Figs. 6, A6, A8-A11), which show a considerable variation. This indicates on one hand the existence of different populations of hematite and goethite and, on the other hand, the eventual mixing of the latter. Our geochronological data set shows substantial intra- and inter-subsample age ranges which largely exceed analytical uncertainty (Figs. 5 and A6). In order to extract geological meaningful information from these data we will therefore discuss the possible reasons of this data distribution and their importance.

Loss or gain of either He or actinide elements can impact the (U-Th)/He ages and in the following different parameters, such as rich U-Th mineral inclusions, He loss due to diffusion, porosity, or wildfire, that can lead to uninterpretable ages, are discussed. Firstly, too old ages can result from neighboring or inclusion of actinide rich minerals such as zircon that will increase the He budget without impacting the U-Th contents (Vasconcelos et al., 2013;

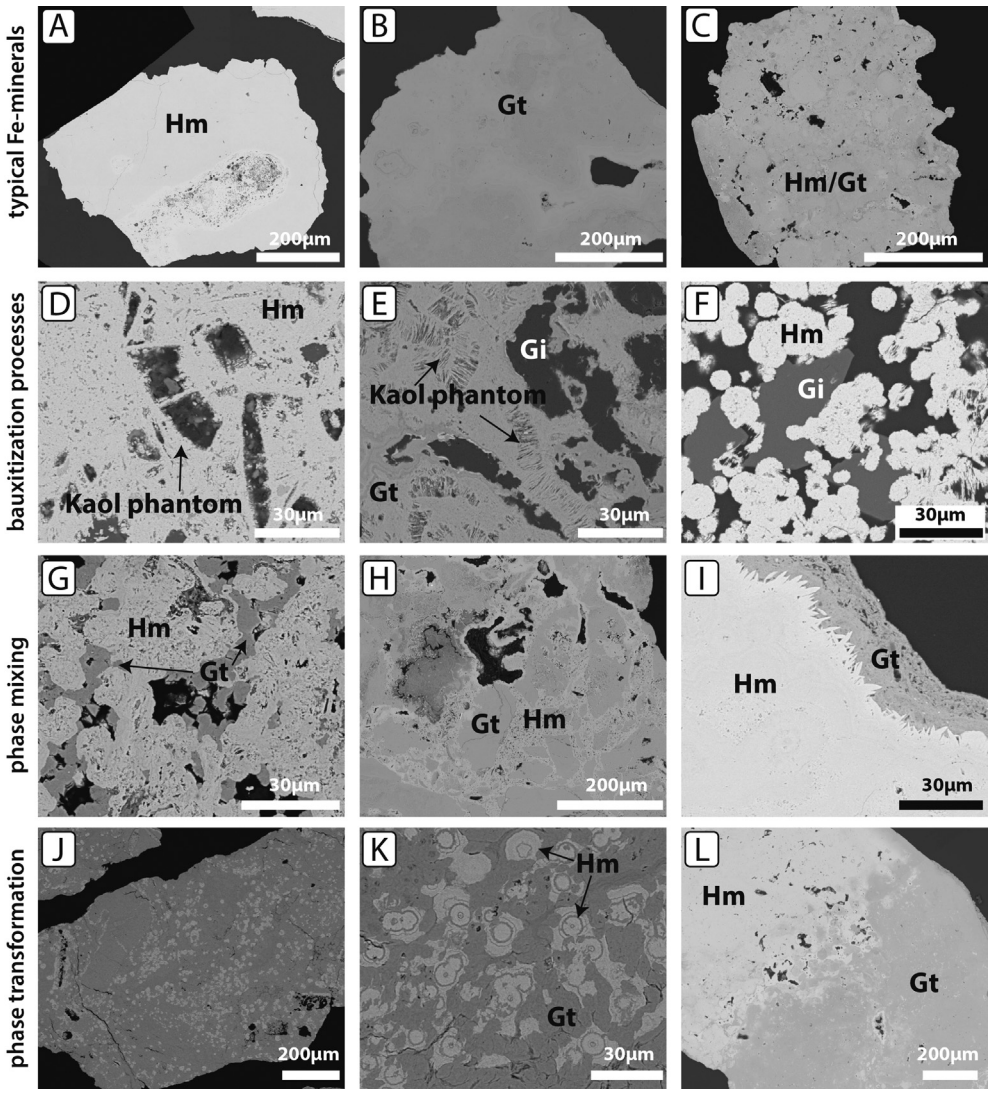

Fig. 4. Scanning Electron microscopy images of representative grains of hematite and goethite. (A) Well-crystallized, botryoidal hematite coating less pure and porous matrix (CDR-01B_3). (B) Well-crystallized glassy black goethite (KAWF-1A_5CII). (C) Typical texture of a porous pisolith composed mainly of hematite (KAWF-5A_1A).(D) Internal hollows created by the dissolution of kaolinite (arrow) (CDR-01A_2). (E) Goethite grain with kaolinite dissolution features (“phantoms”, black arrows) and late stage gibbsite (Gi) filling porosity (KAWF-4A_3A). (F) Micro-nodules of hematite with late stage µm-sized gibbsite (CDR-02_D2). (G-I) phase mixing of hematite (Hm) and goethite (Gt). (G) Goethite crystallized in voids cementing hematite aggregates (CDR-02_E2). (H) Goethite showing brecciated texture cemented by late-stage hematite (KAWF-5B_1B). (I) Pure and well-crystallized hematite coated by late-stage porous Al-rich goethite (CDR-01B_3). (J) Goethite (dark gray) grain with many small hematite spots (bright gray) (KAWF-5B_2AII). (K) Zoomed image of (J), showing concentric hematite pisoids in a goethite matrix partly overlapping the pisoids. We interpret these features as hydration features representing the transformation of hematite into goethite. (L) Grain composed of hematite and goethite from the outermost coating of sample CDR-01 showing the progressive hydration of the hematite (CDR-01A_1).

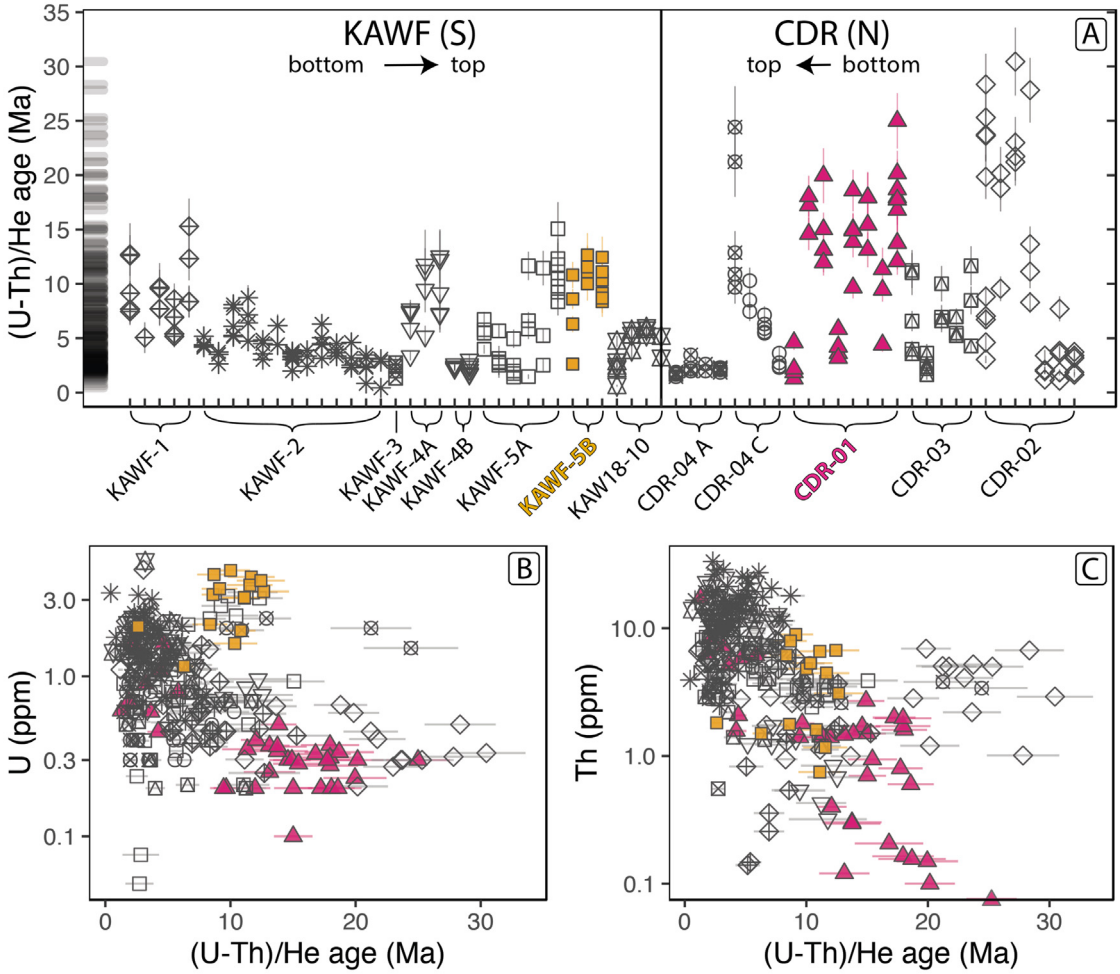

Fig. 5. Representation of all obtained (U-Th)/He ages from the Kaw mountain ridge. (A) shows the ages for every individual subsample (n = 284). Every vertical line is one subsample, color and shape represent the different bulk samples which are ordered from South to North. Grey bars at the left hand side indicate the overall data density. (B) and (C) show the ages for every sample relative to their U and Th concentrations (y-scales are logarithmic). Colors and shapes are as in A according to the samples. Several samples show correlations ages with U or Th concentrations but clear differences are visible between the different samples. For data see Table 3, individual plots for every sample can be found in Fig. A6 of the Electronic Supplement.

Monteiro et al., 2014) or through loss of U by volatilization during degassing as described by Vasconcelos et al. (2013) and Hofmann et al. (2020). We carefully checked many of the subsamples by SEM and only little very small (<5 μm often < 2 μm) zircon and rutile inclusions were found. As rutile has generally low U and Th contents (Meinhold, 2010) similar to those observed in our subsamples, such small inclusions are not supposed to significantly increase the ages. Zircon inclusions could be problematic, but according to Vermeesch et al. (2007) and Gautheron et al. (2012) the error, which can result from inclusions of such small size (compared to the ca. 500 μm aliquots), is in the range of 0–20% depending on the amount of zircon crystals and their U and Th content. Zr content in the bulk samples shows no enrichment (100–260 ppm) compared to the mean upper continental crust (193 ppm, Rudnick and Gao, 2013) indicating no major presence of zircon in our samples.

Secondly, the U content is consistent between the dated subsamples and the bulk samples (Fig. 7A) indicating no detectable loss of U during the degassing procedure. Fig. A3 of the Electronic Supplement shows examples of several subsamples with age-U relationships showing a positive or no correlation of (U-Th)/He ages and U, indicating that no major U loss leading to erroneously old ages affected the samples. Furthermore, the heating temperature during degassing was controlled and an internal goethite standard was systematically analyzed with the samples. It is therefore little probable that our data set contains erroneously old ages. Note at this point that the three oldest ages come from three different subsamples (CDR-02_2A, CDR-02_2D and CDR-02_2E) of the same bulk sample but overlap within error.

Thirdly, He loss can lead to erroneously young ages, associated with He lost (ca. 2–20%) due to the polycrys-

talline nature of hematite and goethite (Shuster et al., 2005; Heim et al., 2006; Vasconcelos et al., 2013; Balout et al., 2017; Deng et al., 2017; Hofmann et al., 2017; Farley, 2018). However, our adapted He loss diffusion correction and the large error applied allows one to correct for this issue, even if this correction does not include eventual He loss due to porosity or poor crystallinity. The Fe-minerals dated here are often porous (e. g. Fig. 4C, 4F, 4G). If pores are empty, alpha-particles are not stopped when going through them, ejection is thus not a problem. However, if the pores are filled with water, the alpha particles will be slowed down or stopped. The mean distance of alpha particles in water is $\sim$ 35 μm (Palmer and Akhavan-Rezayat, 1978) (versus $\sim$ 15 μm in hematite and goethite, Ketcham et al. (2011)). In water filled pores $>$ 35 μm all alpha particles will therefore be stopped, whereas only some alpha particles will be stopped in pores $<$ 35 μm (depending on their incident energy and the size of the pore). Porosity and intergrown unretentive phases have no impact on He diffusivity if the pores (or unretentive phases) are small and unconnected. However, interconnected porosity (or large unretentive phases) can accelerate diffusion as He might escape along these fast diffusion pathways and be lost.

The above analysis shows that there are only few factors that can lead to erroneously old ages (zircon inclusions and U evaporation) and we do not consider that they have had a major influence on our dataset. Even if uncontrolled He loss by diffusion through interconnected porosity and unretentive phases might also play a role, we believe that measured U, Th, Sm, and He content of this study are robust and that the (U-Th)/He ages are mainly related to weathering processes, i.e. iron oxyhydroxide precipitation, dissolution and reprecipitation. For discussion of the mechanisms of these processes in lateritic iron crusts see Monteiro et al. (2014). Thus, gain of U and Th can mainly occur by later addition of Th and U bearing phases. When addition happens significantly after initial precipitation this will lead to mixed ages between the initial and the later phase. The effect of this mixing upon the measured ages will depend on the endmember ages, respective concentrations of U and Th in the initial and the added phases and the proportions of the latter. As shown in Fig. 4, the dated subsamples are often not homogeneous at microscopic scale and some of the dated aliquots represent a small-scale mixture of several phases of the same or different mineralogy. The commonly observed trends of age with U or Th support this assumption (Figs. 5 and 6). To test the mixing of minerals with different U-Th content and ages, a simple mixing model has been performed and results for different phase mixing scenarios of a 20 Ma old phase with a 2 Ma old phase with various actinide content are reported in Fig. 8 as well as Fig. A13 and Table A5 of the Electronic Supplement. Depending on the actinide concentrations in the two phases, the apparent mixed age, i.e. age that would be obtained from the measured amount of He, U and Th, varies a lot. The order of magnitude of change will depend on the two endmembers age value. If the older phase has low actinide concentrations and the younger one high concentrations, the mixed age gets considerably younger even when containing small amounts of the younger phase. For example, in scenario 1 (phase 1 = 20 Ma, 0.3 ppm U, and 0.3 ppm Th and phase 2 = 2 Ma, 2 ppm U, and 10 ppm Th, pink squares in Fig. 8), a mixing of 90% : 10% leads to an extreme rejuvenation of the age (mixed age ca. 10 Ma). On the contrary, scenario 2 (phase 1 = 20 Ma, 2 ppm U, and 10 ppm Th and phase 2 = 2 Ma, 0.3 ppm U and 0.3 ppm Th, yellow circles in Fig. 8) with a 40% : 60% mixing produced an age at still 18 Ma. However, in the latter case small amounts of the old phase mixed in the young phase led to significantly older ages. For more extreme concentration differences, the age varies even more abruptly. For equal concentrations in both phases the age changes linearly with the proportion of the phases (grey triangles in Fig. 8).

The mixing examples show, how even small amounts of a second phase can significantly change the measured ages. If old phases are actinide-poor, as it is the case for most of our samples (Fig. 5B and 5C), small amounts of an actinide-rich younger phase can considerably lower and spread the ages. On the other hand, the mixing scenario 2 shows that an old phase which is actinide rich can incorporate large amounts of an actinide poor younger phase without this leading to a spread of the data. This could explain the rather homogeneous ages observed in the older subsamples of sample KAWF-5 (Fig. 6). In addition, the complex age versus U/Th relations observed in our dataset coupled to the SEM microscale petrological images indicate that in our samples and probably also in some of the individual subsamples, more than 2 phases are being mixed. The impact of the mixing onto the ages depends strongly on the actinide concentrations. The fact that in most samples the youngest subsamples are actinide rich might be one principal reason for the large age range observed in our dataset.

We assume that most age spreading inside individual subsamples is due to mixing of phases related to multiple redissolution/reprecipitation processes. Depending on the proportions of the mixed phases, maximum and minimum ages of each subsample might be of smaller or greater importance. For old subsamples, the oldest ages are endmembers with potential geological significance. In contrast, the younger ages of the same subsamples might probably be a product of phase mixing related to later overgrowths or posterior precipitation of material in voids. Overlapping maximum ages in similar subsamples – such as subsamples CDR-02_2A, CDR-02_2D and CDR-02_2E which yield the three oldest ages of our dataset (Fig. 5 and Table 3) – indicate that these ages have probably a geologic significance (see also Monteiro et al. (2014)). For the youngest subsamples, the situation is slightly different as mixing of previously existing material with the new material might lead to older ages. This could probably be the case when a coating forms on top of an ancient matrix by hydration of the latter as for example in CDR-01A_1 (see also Fig. 4L). We should therefore regard both maximum and minimum ages of the dated subsamples in order to extract geologically significant information from the present data set (Fig. 9A-B). Maximum ages are more relevant in the older subsamples while minimum ages might give insight into the last event(s) that affected the samples.

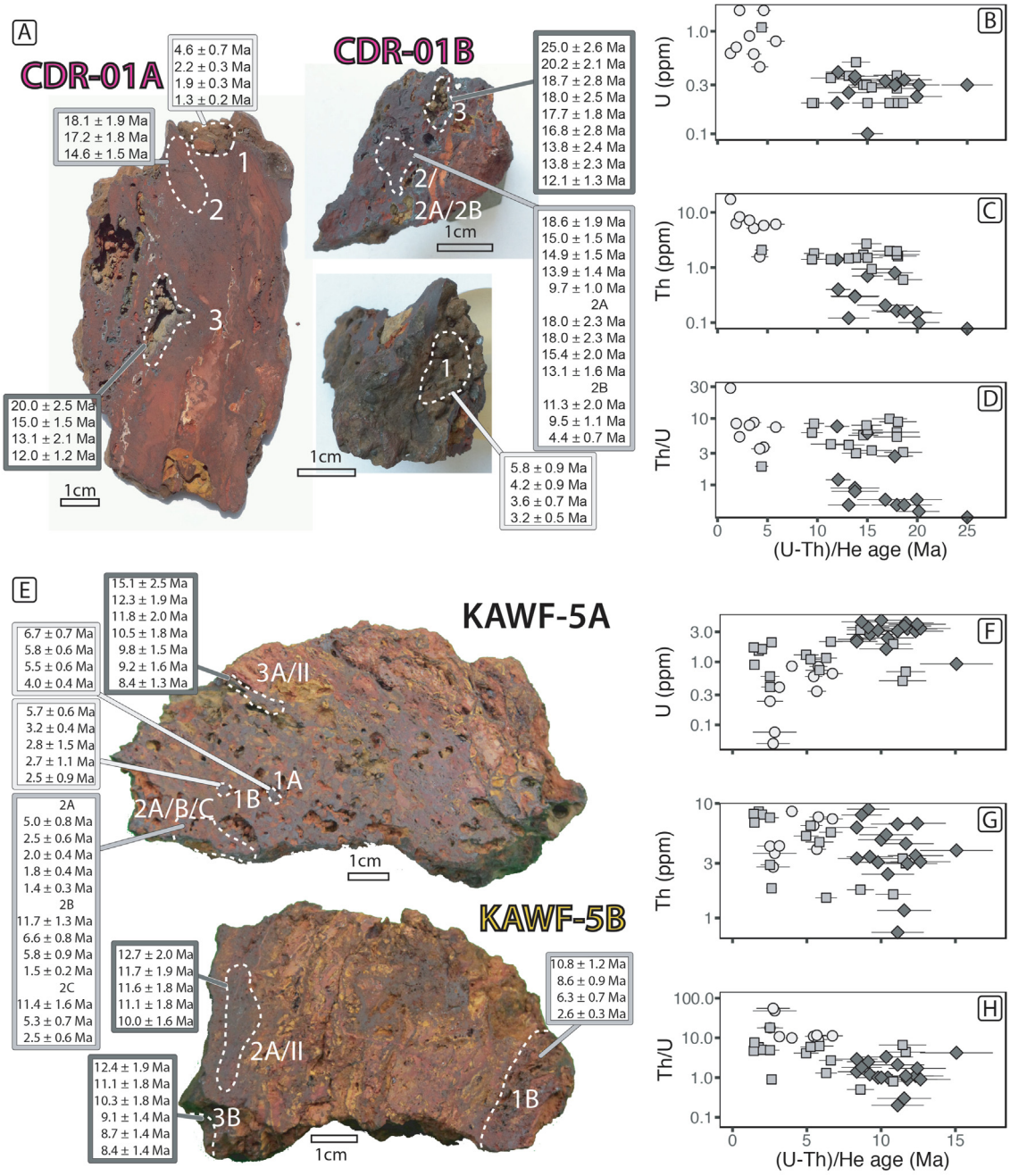

Fig. 6. Samples CDR-01 (A-D) and KAWF-5 (D-H). (A) shows a picture of the two analyzed blocks of sample CDR-01 with the locations of the separated subsamples and the obtained (U-Th)/He ages. (B-D) show the ages relative to their corresponding U and Th concentrations and the Th/U ratios. Colors are as boxes in A, shapes refer to specific subsamples. The sample and some of the subsamples such as A3 and B3 show a clear increase in U and Th concentrations towards younger ages (y-scales are logarithmic). For calculated regressions see Fig. A8 of the Electronic Supplement. (E) shows a picture of the two analyzed blocks of the sample KAWF-5 with the locations of the separated subsamples and the obtained (U-Th)/He ages. Subsamples 2 A, B, C were sampled at the same locations but differ in terms of color and texture (2A: black glassy gt, 2B: brown reddish Gt/Gt-Hm mix, 2C: metallic porous fragments, similar to pisoliths).(F-H) show the ages relative to their corresponding U and Th concentrations and the Th/U ratios. Colors are as in E, subsamples were grouped into of Al-poor Gt (dark gray diamonds), pisoliths (bright gray circles) and rather mixed phases (medium gray squares). U concentrations (F) are higher in the older subsamples and decrease towards younger ages with a slight re-increase for the youngest ages (subsample KAWF-5A_2A). Th concentrations (G) cover the same range for all ages but aliquots of the same subsample have often similar concentrations. Th/U ratios (H) increase towards younger ages mainly due to U decrease (see F) and vary by two orders of magnitude. The small hematite pisoliths (subsamples KAWF-5A_1A and 1B) have clearly higher Th/U ratios than the older goethite subsamples. For calculated regressions see Fig. A9 of the Electronic Supplement.

Table 3
(U-Th)/He data of all analyzed samples. For subsamples analyzed by μ-XRD the hematite goethite ratio (RHG) is given, for those subsamples containing more than 20% goethite (RHG < 0.8), the Fe-Al-substitution of the goethite is equally given. For calculation details see section 4, for complementary mineralogical results and errors of the mineralogical data see Table A3 of the Electronic Supplement.

Sample	Subsample	Aliquot	Weight	^{4}He	^{4}He	^{238}U	^{232}Th	^{147}Sm	^{238}U	^{232}Th	^{147}Sm	Sm (total)	Th/U	Raw age	Corrected age	Error corrected age	Diffusion correction factor	Predominant mineral	RHG	Goethite Fe-Al-substitution
			μg	mol	mol/g	ng	ng	ng	ppm	ppm	ppm	ppm		Ma	Ma	Ma	%			mol%
CDR-01A	CDR-01A_1	C1A110	240	7.08E-15	2.95E-11	0.15	4.15	0.030	0.61	17.29	0.13	0.87	28.6	1.2	1.3	0.2	10	Gt	0.19	19.2
CDR-01A	CDR-01A_1	CDR#01A1_g1	123	2.55E-15	2.07E-11	0.09	0.77	0.020	0.70	6.30	0.10	0.67	8.4	1.7	1.9	0.3	10	Gt	0.19	19.2
CDR-01A	CDR-01A_1	CDR#01A1_g4	158	1.06E-14	6.69E-11	0.25	0.91	0.040	1.60	5.80	0.20	1.33	3.7	4.2	4.6	0.7	10	Gt	0.19	19.2
CDR-01A	CDR-01A_1	CDR#01A1_g6	41	1.54E-15	3.77E-11	0.06	0.34	0.010	1.60	8.30	0.20	1.33	5.3	2.0	2.2	0.3	10	Gt	0.19	19.2
CDR-01A	CDR-01A_2	CDR#01A2_g6	103	6.02E-15	5.85E-11	0.02	0.20	0.010	0.20	2.00	0.10	0.67	9.9	16.4	17.2	1.8	5	Ht		
CDR-01A	CDR-01A_2	CDR#01A2_g7	67	3.53E-15	5.27E-11	0.01	0.11	0.010	0.20	1.60	0.10	0.67	8.9	17.2	18.1	1.9	5	Ht		
CDR-01A	CDR-01A_2	CDR#01A2_g8	119	6.38E-15	5.36E-11	0.04	0.20	0.020	0.30	1.70	0.20	1.33	5.6	13.9	14.6	1.5	5	Ht		
CDR-01A	CDR-01A_3	C1A310	78	1.48E-15	1.89E-11	0.02	0.01	0.000	0.25	0.12	0.01	0.05	0.5	12.5	13.1	2.1	5	Ht	1.00	
CDR-01A	CDR-01A_3	C1A311	114	3.12E-15	2.74E-11	0.03	0.02	0.000	0.23	0.15	0.01	0.05	0.6	19.0	20.0	2.5	5	Ht	1.00	
CDR-01A	CDR-01A_3	CDR#01A3_g10	194	6.25E-15	3.22E-11	0.04	0.28	0.010	0.20	1.40	0.00	0.00	7.6	11.4	12.0	1.2	5	Ht	1.00	
CDR-01A	CDR-01A_3	CDR#01A3_g9	207	4.64E-15	2.24E-11	0.02	0.15	0.010	0.10	0.70	0.00	0.00	6.0	14.3	15.0	1.5	5	Ht	1.00	
CDR-01B	CDR-01B_1	C1B110	50	1.61E-15	3.23E-11	0.03	0.26	0.010	0.60	5.16	0.15	1.00	8.7	3.3	3.6	0.7	10	Gt		
CDR-01B	CDR-01B_1	C1B111	99	1.68E-15	1.70E-11	0.04	0.16	0.010	0.45	1.57	0.06	0.40	3.5	3.8	4.2	0.9	10	Gt		
CDR-01B	CDR-01B_1	CDR#01B1_g2	56	3.63E-15	6.49E-11	0.05	0.34	0.010	0.80	6.10	0.10	0.67	7.4	5.3	5.8	0.9	10	Gt		
CDR-01B	CDR-01B_1	CDR#01B1_g3	48	1.96E-15	4.08E-11	0.04	0.34	0.000	0.90	7.20	0.10	0.67	7.9	2.9	3.2	0.5	10	Gt		
CDR-01B	CDR-01B_2	CDR#01B2_g1	116	7.05E-15	6.08E-11	0.06	0.17	0.010	0.50	1.50	0.10	0.67	3.0	13.2	13.9	1.4	5	Ht	0.82	
CDR-01B	CDR-01B_2	CDR#01B2_g2	187	8.39E-15	4.49E-11	0.04	0.28	0.050	0.20	1.50	0.30	2.00	6.7	14.3	15.0	1.5	5	Ht	0.82	
CDR-01B	CDR-01B_2	CDR#01B2_g3	173	5.93E-15	3.43E-11	0.04	0.11	0.000	0.20	0.60	0.00	0.00	3.1	17.7	18.6	1.9	5	Ht	0.82	
CDR-01B	CDR-01B_2	CDR#01B2_g4	80	2.61E-15	3.26E-11	0.02	0.15	0.030	0.20	1.80	0.40	2.67	8.4	9.2	9.7	1.0	5	Ht	0.82	
CDR-01B	CDR-01B_2	CDR#01B2_g5	158	1.20E-14	7.62E-11	0.05	0.43	0.090	0.30	2.70	0.60	4.00	7.9	14.2	14.9	1.5	5	Ht	0.82	
CDR-01B	CDR-01B_2A	C1B2A10	51	3.22E-15	6.31E-11	0.01	0.09	0.024	0.28	1.71	0.46	3.09	6.2	17.1	18.0	2.3	5	Ht		
CDR-01B	CDR-01B_2A	C1B2A11	76	3.64E-15	4.79E-11	0.03	0.11	0.003	0.37	1.46	0.04	0.25	4.0	12.5	13.1	1.6	5	Ht		
CDR-01B	CDR-01B_2A	C1B2A12	64	2.58E-15	4.03E-11	0.02	0.06	0.005	0.28	0.94	0.07	0.47	3.3	14.7	15.4	2.0	5	Ht		
CDR-01B	CDR-01B_2A	C1B2A13	35	2.71E-15	7.75E-11	0.01	0.07	0.015	0.37	1.97	0.43	2.87	5.3	17.1	18.0	2.3	5	Ht		
CDR-01B	CDR-01B_2B	C1B2B15	47	1.66E-15	3.54E-11	0.05	0.10	0.017	1.09	2.08	0.37	2.47	1.9	4.2	4.4	0.7	5	Ht		
CDR-01B	CDR-01B_2B	C1B2B16	28	1.11E-15	3.97E-11	0.01	0.04	0.000	0.35	1.41	0.02	0.13	4.1	10.8	11.3	2.0	5	Ht		
CDR-01B	CDR-01B_2B	C1B2B18	180	4.91E-15	2.73E-11	0.04	0.25	0.000	0.20	1.40	0.00	0.00	6.1	9.0	9.5	1.1	5	Ht		
CDR-01B	CDR-01B_3	C1B310	39	1.27E-15	3.25E-11	0.01	0.01	0.000	0.33	0.21	0.01	0.06	0.6	16.0	16.8	2.8	5	Ht	0.98	
CDR-01B	CDR-01B_3	C1B311	38	1.11E-15	2.92E-11	0.01	0.01	0.000	0.34	0.30	0.01	0.07	0.9	13.1	13.8	2.4	5	Ht	0.98	
CDR-01B	CDR-01B_3	C1B312	65	2.09E-15	3.21E-11	0.02	0.01	0.000	0.31	0.16	0.01	0.07	0.5	17.1	18.0	2.5	5	Ht	0.98	
CDR-01B	CDR-01B_3	C1B313	40	1.22E-15	3.06E-11	0.01	0.01	0.000	0.36	0.30	0.01	0.06	0.8	13.1	13.8	2.3	5	Ht	0.98	
CDR-01B	CDR-01B_3	C1B314	49	1.76E-15	3.59E-11	0.02	0.01	0.000	0.34	0.16	0.01	0.05	0.5	17.8	18.7	2.8	5	Ht	0.98	
CDR-01B	CDR-01B_3	CDR#01B3_g1	183	6.20E-15	3.39E-11	0.05	bld	0.000	0.30	bld	0.00	0.00		23.8	25.0	2.6	5	Ht	0.98	
CDR-01B	CDR-01B_3	CDR#01B3_g2	123	5.26E-15	4.28E-11	0.03	0.10	0.020	0.30	0.80	0.10	0.67	2.7	16.9	17.7	1.8	5	Ht	0.98	
CDR-01B	CDR-01B_3	CDR#01B3_g3	165	5.44E-15	3.30E-11	0.05	0.02	0.000	0.30	0.10	0.00	0.00	0.4	19.2	20.2	2.1	5	Ht	0.98	
CDR-01B	CDR-01B_3	CDR#01B3_g5	157	4.51E-15	2.87E-11	0.06	0.07	0.000	0.40	0.40	0.00	0.00	1.2	11.5	12.1	1.2	5	Ht	0.98	
CDR-02	CDR-02_1A	CDR#02A1_g10	92	2.10E-15	2.28E-11	0.09	0.50	0.010	1.00	5.40	0.10	0.67	5.7	1.9	2.1	0.3	10	Gt	0.16	25.5
CDR-02	CDR-02_1A	CDR#02A1_g2	67	1.10E-15	1.64E-11	0.07	0.46	0.010	1.10	6.80	0.10	0.67	6.1	1.1	1.2	0.2	10	Gt	0.16	25.5
CDR-02	CDR-02_1A	CDR#02A1_g7	104	2.68E-15	2.57E-11	0.13	0.57	0.010	1.30	5.50	0.10	0.67	4.2	1.8	2.0	0.3	10	Gt	0.16	25.5
CDR-02	CDR-02_1A	CDR#02A1_g8	173	7.05E-15	4.07E-11	0.25	0.75	0.020	1.40	4.30	0.10	0.67	3.0	3.1	3.4	0.5	10	Gt	0.16	25.5
CDR-02	CDR-02_1A	CDR#02A1_g9	79	2.45E-15	3.10E-11	0.14	0.44	0.010	1.70	5.50	0.10	0.67	3.2	1.9	2.1	0.3	10	Gt	0.16	25.5
CDR-02	CDR-02_2A	C2A210	49	1.94E-15	3.96E-11	0.02	0.14	0.017	0.40	2.90	0.35	2.33	7.2	6.7	7.0	1.0	5	Ht	0.82	

CDR-02	CDR-02_2A	C2A211	62	5.51E-15	8.89E-11	0.29	0.26	0.002	4.64	4.11	0.04	0.27	0.9	2.9	3.0	0.4	5	Ht	0.82	
CDR-02	CDR-02_2A	C2A212	71	2.21E-15	3.11E-11	0.05	0.20	0.002	0.66	2.79	0.03	0.21	4.2	4.4	4.6	0.6	5	Ht	0.82	
CDR-02	CDR-02_2A	C2A213	74	3.23E-15	4.36E-11	0.06	0.13	0.001	0.85	1.75	0.01	0.08	2.1	6.4	6.7	0.9	5	Ht	0.82	
CDR-02	CDR-02_2A	C2A214	116	2.62E-14	2.26E-10	0.07	0.80	0.003	0.59	6.90	0.03	0.17	11.7	18.9	19.8	2.0	5	Ht	0.82	
CDR-02	CDR-02_2A	C2A215	151	6.85E-15	4.54E-11	0.06	0.39	0.003	0.39	2.60	0.02	0.11	6.7	8.4	8.8	1.0	5	Ht	0.82	
CDR-02	CDR-02_2A	CDR#02A2_g1	72	1.32E-14	1.83E-10	0.02	0.37	0.000	0.30	5.20	0.00	0.00	18.8	22.6	23.7	2.4	5	Ht	0.82	
CDR-02	CDR-02_2A	CDR#02A2_g3	164	4.86E-14	2.97E-10	0.08	1.10	0.000	0.50	6.70	0.00	0.00	14.3	27.0	28.4	2.8	5	Ht	0.82	
CDR-02	CDR-02_2A	CDR#02A2_g4	132	2.49E-14	1.88E-10	0.03	0.66	0.000	0.30	5.00	0.00	0.00	19.2	24.1	25.3	2.5	5	Ht	0.82	
CDR-02	CDR-02_2A	CDR#02A2_g5	143	1.37E-14	9.55E-11	0.04	0.31	0.000	0.30	2.20	0.00	0.00	8.2	22.5	23.6	2.4	5	Ht	0.82	
CDR-02	CDR-02_2B	C2B22	78	4.17E-15	5.34E-11	0.04	0.21	0.003	0.46	2.68	0.04	0.25	5.8	9.1	9.6	1.1	5	Ht		
CDR-02	CDR-02_2B	C2B23	47	6.03E-15	1.28E-10	0.03	0.13	0.004	0.66	2.83	0.09	0.58	4.3	17.9	18.8	2.1	5	Ht		
CDR-02	CDR-02_2B	C2B24	77	3.90E-15	5.06E-11	0.02	0.09	0.000	0.21	1.20	0.01	0.03	5.9	19.2	20.2	2.4	5	Ht		
CDR-02	CDR-02_2D	C2D21	173	2.76E-14	1.59E-10	0.06	0.50	0.008	0.33	2.92	0.04	0.29	8.8	29.0	30.5	3.1	5	Ht	0.96	
CDR-02	CDR-02_2D	C2D22	146	2.62E-14	1.79E-10	0.07	0.74	0.001	0.45	5.05	0.01	0.06	11.2	20.2	21.2	2.2	5	Ht	0.96	
CDR-02	CDR-02_2D	C2D23	158	2.31E-14	1.46E-10	0.04	0.65	0.001	0.27	4.09	0.01	0.04	15.0	21.9	23.0	2.4	5	Ht	0.96	
CDR-02	CDR-02_2D	C2D24	121	2.15E-14	1.77E-10	0.05	0.60	0.001	0.41	5.00	0.01	0.07	12.3	20.7	21.7	2.3	5	Ht	0.96	
CDR-02	CDR-02_2E	C2E21	66	4.76E-15	7.21E-11	0.10	0.06	0.002	1.48	0.94	0.03	0.19	0.6	7.9	8.3	1.0	5	Ht		
CDR-02	CDR-02_2E	C2E22	68	4.23E-15	6.22E-11	0.04	0.07	0.011	0.65	1.00	0.16	1.06	1.5	13.0	13.7	1.6	5	Ht		
CDR-02	CDR-02_2E	C2E23	72	2.35E-15	3.26E-11	0.02	0.08	0.003	0.30	1.12	0.05	0.31	3.7	10.6	11.1	1.5	5	Ht		
CDR-02	CDR-02_2E	C2E24	143	1.13E-14	7.91E-11	0.04	0.14	0.017	0.31	1.01	0.12	0.81	3.2	26.5	27.8	3.0	5	Ht		
CDR-02	CDR-02_3A	CDR#02A3_g1	108	3.35E-15	3.10E-11	0.20	0.66	0.010	1.90	6.10	0.00	0.00	3.3	1.7	1.9	0.3	10	Gt	0.01	18.7
CDR-02	CDR-02_3A	CDR#02A3_g2	67	4.64E-15	6.93E-11	0.12	0.60	0.020	1.80	8.90	0.30	2.00	4.9	3.3	3.6	0.6	10	Gt	0.01	18.7
CDR-02	CDR-02_3A	CDR#02A3_g3	86	1.17E-14	1.36E-10	0.10	0.91	0.000	1.10	10.60	0.00	0.00	9.5	7.0	7.7	1.2	10	Gt	0.01	18.7
CDR-02	CDR-02_3A	CDR#02A3_g5	111	6.96E-15	6.27E-11	0.23	0.62	0.020	2.00	5.60	0.20	1.33	2.7	3.5	3.9	0.6	10	Gt	0.01	18.7
CDR-02	CDR-02_3A	CDR#02A3_g6	74	1.20E-15	1.63E-11	0.10	0.49	0.010	1.40	6.60	0.20	1.33	4.9	1.0	1.1	0.2	10	Gt	0.01	18.7
CDR-02	CDR-02_4A	CDR#02A4_g1	155	1.20E-14	7.77E-11	0.37	1.24	0.030	2.40	8.00	0.20	1.33	3.4	3.4	3.7	0.6	10	Gt		
CDR-02	CDR-02_4A	CDR#02A4_g2	98	2.40E-15	2.45E-11	0.13	0.56	0.010	1.30	5.70	0.10	0.67	4.3	1.7	1.9	0.3	10	Gt		
CDR-02	CDR-02_4A	CDR#02A4_g3	138	6.83E-15	4.95E-11	0.26	0.73	0.010	1.90	5.30	0.10	0.67	2.8	2.9	3.2	0.5	10	Gt		
CDR-02	CDR-02_4A	CDR#02A4_g4	112	3.17E-15	2.83E-11	0.25	0.59	0.020	2.20	5.30	0.10	0.67	2.4	1.5	1.7	0.3	10	Gt		
CDR-02	CDR-02_4A	CDR#02A4_g5	89	6.29E-15	7.07E-11	0.24	0.57	0.020	2.70	6.40	0.20	1.33	2.4	3.1	3.4	0.5	10	Gt		
CDR-03	CDR-03A_1	CDR#03A1_g2	92	5.35E-15	5.82E-11	0.11	0.63	0.030	1.10	6.80	0.30	2.00	5.9	3.9	4.3	0.7	10	Gt		
CDR-03	CDR-03A_1	CDR#03A1_g3	108	6.87E-15	6.36E-11	0.04	0.53	0.000	0.40	4.90	0.00	0.00	13.3	7.7	8.5	1.3	10	Gt		
CDR-03	CDR-03A_1	CDR#03A1_g4	23	2.08E-15	9.06E-11	0.02	0.09	0.000	0.70	3.80	0.00	0.00	5.7	10.6	11.7	1.8	10	Gt		
CDR-03	CDR-03_3	C331	29	9.15E-16	3.16E-11	0.01	0.04	0.000	0.21	1.45	0.04	0.27	6.8	10.5	11.0	2.1	5	Ht		
CDR-03	CDR-03_3	C332	72	7.58E-16	1.05E-11	0.01	0.10	0.000	0.20	1.40	0.00	0.00	7.5	3.8	4.0	0.8	5	Ht		
CDR-03	CDR-03_3	C333	60	8.92E-16	1.49E-11	0.02	0.13	0.010	0.30	2.20	0.10	0.67	6.9	3.4	3.6	0.6	5	Ht		
CDR-03	CDR-03_3	C334	60	1.74E-15	2.90E-11	0.01	0.07	0.000	0.20	1.20	0.00	0.00	5.0	10.7	11.2	1.6	5	Ht		
CDR-03	CDR-03_3	C335	113	1.99E-15	1.76E-11	0.02	0.15	0.000	0.21	1.34	0.04	0.27	6.5	6.3	6.6	0.9	5	Ht		
CDR-03	CDR-03_4	C341	58	1.20E-15	2.08E-11	0.04	0.30	0.010	0.70	5.10	0.20	1.33	7.4	2.0	2.2	0.5	10	Gt		
CDR-03	CDR-03_4	C342	47	8.92E-16	1.90E-11	0.02	0.15	0.010	0.30	3.20	0.10	0.67	9.5	3.3	3.6	0.8	10	Gt		
CDR-03	CDR-03_4	C343	60	5.35E-16	8.92E-12	0.03	0.17	0.000	0.50	2.90	0.00	0.00	6.4	1.5	1.7	0.5	10	Gt		
CDR-03	CDR-03_4	C344	43	7.61E-16	1.77E-11	0.03	0.15	0.000	0.69	3.48	0.08	0.53	5.1	2.2	2.4	0.6	10	Gt		
CDR-03	CDR-03_4	C345	21	4.39E-16	2.09E-11	0.01	0.10	0.000	0.52	4.55	0.11	0.73	8.8	2.4	2.7	0.9	10	Gt		
CDR-03	CDR-03_5A	C35A1	68	5.35E-15	7.87E-11	0.05	0.26	0.010	0.70	3.90	0.10	0.67	5.3	9.1	10.0	1.6	10	Gt		
CDR-03	CDR-03_5A	C35A2	144	7.58E-15	5.27E-11	0.11	0.54	0.010	0.80	3.70	0.10	0.67	4.9	6.0	6.6	1.1	10	Gt		
CDR-03	CDR-03_5A	C35A3	100	5.80E-15	5.80E-11	0.08	0.40	0.010	0.80	4.00	0.10	0.67	5.1	6.3	6.9	1.1	10	Gt		
CDR-03	CDR-03_5B	C35B1	74	4.91E-15	6.63E-11	0.05	0.52	0.010	0.70	7.00	0.10	0.67	9.8	5.2	5.5	0.6	5	Gt-Ht-mix		
CDR-03	CDR-03_5B	C35B2	109	6.69E-15	6.14E-11	0.08	0.72	0.010	0.80	6.60	0.10	0.67	8.5	5.0	5.3	0.6	5	Gt-Ht-mix		
CDR-03	CDR-03_5B	C35B4	88	7.87E-15	8.94E-11	0.08	0.58	0.010	0.92	6.65	0.13	0.87	7.2	6.6	7.0	0.8	5	Gt-Ht-mix		
CDR-04A	CDR-04A_2A	C4A2A1	94	3.35E-15	3.56E-11	0.06	1.27	0.030	0.60	13.50	0.30	2.00	21.3	1.7	1.8	0.2	5	Ht	0.82	
CDR-04A	CDR-04A_2A	C4A2A2	87	3.26E-15	3.74E-11	0.05	1.22	0.020	0.50	14.10	0.30	2.00	26.3	1.8	1.9	0.2	5	Ht	0.82	

(*continued on next page*)

Table 3 (*continued*)

Sample	Subsample	Aliquot	Weight	^{4}He	^{4}He	^{238}U	^{232}Th	^{147}Sm	^{238}U	^{232}Th	^{147}Sm	Sm (total)	Th/U	Raw age	Corrected age	Error corrected age	Diffusion correction factor	Predominant mineral	RHG	Goethite Fe-Al-substitution
			μg	mol	mol/g	ng	ng	ng	ppm	ppm	ppm	ppm		Ma	Ma	Ma	%			mol%
CDR-04A	CDR-04A_2A	C4A2A3	111	3.35E-15	3.01E-11	0.07	1.61	0.030	0.60	14.50	0.30	2.00	24.5	1.4	1.5	0.2	5	Ht	0.82	
CDR-04A	CDR-04A_2A	C4A2A4	27	1.25E-15	4.63E-11	0.02	0.52	0.030	0.80	19.10	1.00	6.67	24.5	1.6	1.7	0.3	5	Ht	0.82	
CDR-04A	CDR-04A_2B	C4A2B1	71	1.25E-15	1.76E-11	0.02	0.20	0.000	0.30	2.90	0.10	0.67	9.4	3.3	3.5	0.6	5	Ht	1.00	
CDR-04A	CDR-04A_2B	C4A2B2	81	8.48E-16	1.05E-11	0.02	0.26	0.000	0.30	3.20	0.10	0.67	10.7	1.9	2.0	0.4	5	Ht	1.00	
CDR-04A	CDR-04A_2B	C4A2B3	46	4.33E-16	9.41E-12	0.01	0.13	0.000	0.30	2.80	0.00	0.00	10.9	1.9	2.0	0.6	5	Ht	1.00	
CDR-04A	CDR-04A_2B	C4A2B4	57	7.58E-16	1.33E-11	0.02	0.20	0.000	0.40	3.50	0.10	0.67	9.2	2.1	2.2	0.4	5	Ht	1.00	
CDR-04A	CDR-04A_2BB	C4A2BB1	33	8.92E-16	2.70E-11	0.01	0.23	0.030	0.40	7.00	0.80	5.33	18.4	2.5	2.6	0.5	5	Ht		
CDR-04A	CDR-04A_2BB	C4A2BB2	29	3.35E-16	1.15E-11	0.01	0.09	0.010	0.40	3.10	0.30	2.00	7.6	1.9	2.0	0.7	5	Ht		
CDR-04A	CDR-04A_3A	C4A3A1	54	1.96E-15	3.64E-11	0.05	0.68	0.000	0.90	12.60	0.10	0.67	13.8	1.7	1.9	0.4	10	Gt	0.05	15.7
CDR-04A	CDR-04A_3A	C4A3A2	53	2.94E-15	5.56E-11	0.05	0.91	0.010	1.00	17.10	0.10	0.67	18.0	2.0	2.2	0.4	10	Gt	0.05	15.7
CDR-04A	CDR-04A_3A	C4A3A3	72	2.19E-15	3.04E-11	0.07	0.61	0.010	1.00	8.40	0.20	1.33	8.6	1.9	2.1	0.4	10	Gt	0.05	15.7
CDR-04A	CDR-04A_3A	C4A3A4	46	1.87E-15	4.07E-11	0.05	0.48	0.010	1.10	10.50	0.30	2.00	9.3	2.1	2.3	0.4	10	Gt	0.05	15.7
CDR-04A	CDR-04A_3A	C4A3A5	63	1.92E-15	3.05E-11	0.05	0.54	0.000	0.80	8.50	0.10	0.67	10.8	2.0	2.2	0.4	10	Gt	0.05	15.7
CDR-04A	CDR-04A_3B	C4A3B1	55	1.52E-14	2.76E-10	0.08	0.19	0.020	1.50	3.40	0.40	2.67	2.3	22.2	24.4	3.8	10	Gt	0.00	2.7
CDR-04A	CDR-04A_3B	C4A3B2	94	1.74E-14	1.85E-10	0.22	0.24	0.050	2.30	2.60	0.60	4.00	1.1	11.7	12.9	2.0	10	Gt	0.00	2.7
CDR-04A	CDR-04A_3B	C4A3B3	90	2.72E-14	3.02E-10	0.18	0.34	0.030	2.00	3.80	0.30	2.00	1.9	19.3	21.2	3.2	10	Gt	0.00	2.7
CDR-04A	CDR-04A_3B	C4A3B4	112	1.43E-14	1.27E-10	0.23	0.32	0.030	2.00	2.90	0.30	2.00	1.4	8.8	9.7	1.5	10	Gt	0.00	2.7
CDR-04A	CDR-04A_3B	C4A3B6	45	6.19E-15	1.38E-10	0.09	0.12	0.010	1.94	2.69	0.22	1.47	1.4	9.9	10.9	1.8	10	Gt	0.00	2.7
CDR-04C	CDR-04C_3A	C4C3A1	40	3.88E-15	9.70E-11	0.04	0.28	0.020	0.90	6.90	0.50	3.33	7.8	7.1	7.5	0.9	5	Ht	0.84	
CDR-04C	CDR-04C_3A	C4C3A2	86	7.14E-15	8.30E-11	0.04	0.52	0.030	0.50	6.00	0.30	2.00	11.8	8.1	8.5	0.9	5	Ht	0.84	
CDR-04C	CDR-04C_3A	C4C3A3	44	4.33E-15	9.84E-11	0.03	0.23	0.020	0.60	5.30	0.50	3.33	8.4	9.8	10.3	1.2	5	Ht	0.84	
CDR-04C	CDR-04C_3B	C4C3B1	115	6.25E-15	5.43E-11	0.05	0.68	0.020	0.40	5.90	0.20	1.33	14.8	5.6	5.9	0.7	5	Ht		
CDR-04C	CDR-04C_3B	C4C3B2	119	4.91E-15	4.12E-11	0.04	0.58	0.010	0.30	4.90	0.10	0.67	14.9	5.3	5.6	0.6	5	Ht		
CDR-04C	CDR-04C_3B	C4C3B3	81	3.70E-15	4.57E-11	0.03	0.44	0.010	0.40	5.50	0.10	0.67	15.5	5.2	5.5	0.7	5	Ht		
CDR-04C	CDR-04C_3B	C4C3B4	96	4.46E-15	4.65E-11	0.03	0.46	0.010	0.30	4.80	0.10	0.67	14.5	6.0	6.3	0.7	5	Ht		
CDR-04C	CDR-04C_3B	C4C3B5	63	5.80E-15	9.21E-11	0.09	0.31	0.020	1.40	5.00	0.40	2.67	3.5	6.8	7.1	0.8	5	Ht		
CDR-04C	CDR-04C_4A	C4C4A1	54	2.01E-15	3.72E-11	0.04	0.31	0.010	0.80	5.70	0.20	1.33	7.5	3.3	3.6	0.7	10	Gt		
CDR-04C	CDR-04C_4A	C4C4A2	44	1.38E-15	3.14E-11	0.04	0.28	0.010	0.90	6.30	0.20	1.33	7.3	2.5	2.8	0.6	10	Gt		
CDR-04C	CDR-04C_4A	C4C4A3	77	1.92E-15	2.49E-11	0.05	0.53	0.010	0.60	6.90	0.10	0.67	11.1	2.1	2.3	0.5	10	Gt		
CDR-04C	CDR-04C_4A	C4C4A4	44	1.34E-15	3.04E-11	0.04	0.32	0.010	0.90	7.30	0.20	1.33	8.3	2.2	2.4	0.5	10	Gt		
KAW18-10B2	KAW18-10B2_AA	10B2AA1	112	1.70E-15	1.52E-11	0.16	1.55	0.025	1.41	13.81	0.23	1.51	9.8	< 0.8	<0.8			Ht		
KAW18-10B2	KAW18-10B2_AA	10B2AA2	69	5.68E-15	8.23E-11	0.16	1.42	0.019	2.28	20.61	0.28	1.87	9.1	2.1	2.2	0.4	5	Ht		
KAW18-10B2	KAW18-10B2_AA	10B2AA2	69	5.68E-15	8.23E-11	0.11	1.20	0.015	1.62	17.45	0.22	1.47	10.7	2.7	2.8	0.5	5	Ht		
KAW18-10B2	KAW18-10B2_AA	10B2AA4	78	3.97E-15	5.09E-11	0.09	0.95	0.015	1.17	12.20	0.20	1.30	10.4	2.3	2.4	0.3	5	Ht		
KAW18-10B2	KAW18-10B2_AA	10B2AA5	38	4.30E-15	1.13E-10	0.04	0.59	0.010	1.05	15.50	0.20	1.36	14.8	4.5	4.7	0.5	5	Ht		
KAW18-10B2	KAW18-10B2_AB	10B2AB1	60	4.67E-15	7.79E-11	0.11	0.60	0.012	1.80	9.92	0.20	1.32	5.5	3.5	3.9	0.6	10	Gt		
KAW18-10B2	KAW18-10B2_AB	10B2AB2	31	4.00E-15	1.29E-10	0.07	0.37	0.007	2.16	11.86	0.23	1.56	5.5	4.8	5.3	0.9	10	Gt		
KAW18-10B2	KAW18-10B2_AB	10B2AB3	19	2.01E-15	1.06E-10	0.03	0.18	0.000	1.51	9.61	0.21	1.37	6.4	5.2	5.7	0.9	10	Gt		
KAW18-10B2	KAW18-10B2_BA	10B2BA1	52	7.16E-15	1.38E-10	0.07	0.83	0.010	1.32	16.03	0.22	1.45	12.1	5.0	5.3	0.5	5	Ht		
KAW18-10B2	KAW18-10B2_BA	10B2BA2	47	6.27E-15	1.33E-10	0.06	0.62	0.010	1.21	13.10	0.29	1.94	10.8	5.7	6.0	0.6	5	Ht		
KAW18-10B2	KAW18-10B2_BA	10B2BA3	43	8.70E-15	2.02E-10	0.07	0.95	0.010	1.55	22.21	0.24	1.60	14.3	5.5	5.8	0.6	5	Ht		
KAW18-10B2	KAW18-10B2_BB	10B2BB2	35	4.54E-15	1.30E-10	0.06	0.52	0.010	1.62	14.87	0.23	1.53	9.2	4.7	5.2	0.8	10	Gt		
KAW18-10B2	KAW18-10B2_BB	10B2BB3	23	2.88E-15	1.25E-10	0.12	0.26	0.010	5.21	11.30	0.26	1.73	2.2	2.9	3.2	0.5	10	Gt		
KAWF-1A	KAWF-1A_2BII	K12BII5	15	1.43E-15	9.52E-11	0.01	0.12	0.010	0.60	8.10	0.60	4.00	13.9	7.1	7.5	1.1	5	Ht	0.81	
KAWF-1A	KAWF-1A_2BII	K12BII6	10	8.48E-16	8.48E-11	0.01	0.06	0.010	0.60	6.50	0.90	6.00	10.5	7.3	7.7	1.5	5	Ht	0.81	
KAWF-1A	KAWF-1A_2BII	K1A2BII1	32	1.38E-15	4.32E-11	0.01	0.06	0.010	0.25	1.72	0.21	1.38	6.9	12.1	12.7	2.9	5	Ht	0.81	

KAWF-1A	KAWF-1A_2BII	K1A2BII2	37	3.48E-15	9.41E-11	0.02	0.14	0.010	0.58	3.67	0.20	1.37	6.3	12.0	12.6	1.9	5	Ht	0.81	
KAWF-1A	KAWF-1A_2BII	K1A2BII3	59	6.25E-15	1.06E-10	0.05	0.35	0.010	0.93	5.86	0.22	1.50	6.3	8.7	9.1	1.1	5	Ht	0.81	
KAWF-1A	KAWF-1A_5BB	K1A5BB1	71	1.25E-15	1.76E-11	0.04	0.06	0.000	0.52	0.83	0.05	0.31	1.6	4.6	5.1	1.4	10	Gt		
KAWF-1A	KAWF-1A_5BII	K1A5BII1	48	3.26E-15	6.79E-11	0.03	0.23	0.010	0.67	4.77	0.30	2.00	7.1	7.0	7.7	1.6	10	Gt	0.21	8.6
KAWF-1A	KAWF-1A_5BII	K1A5BII2	66	4.91E-15	7.44E-11	0.05	0.26	0.010	0.69	4.00	0.16	1.08	5.8	8.7	9.6	1.7	10	Gt	0.21	8.6
KAWF-1A	KAWF-1A_5BII	K1A5BII4	35	2.23E-15	6.37E-11	0.02	0.13	0.000	0.45	3.70	0.14	0.91	8.2	8.8	9.7	2.2	10	Gt	0.21	8.6
KAWF-1A	KAWF-1A_5BII	K1A5BII5	28	3.61E-15	1.29E-10	0.04	0.22	0.010	1.56	7.83	0.29	1.94	5.0	7.0	7.7	1.5	10	Gt	0.21	8.6
KAWF-1A	KAWF-1A_5CII	K1A5CII2	55	6.82E-16	1.24E-11	0.02	0.01	0.000	0.45	0.14	0.03	0.19	0.3	4.7	5.2	1.0	10	Gt	0.00	0.3
KAWF-1A	KAWF-1A_5CII	K1A5CII3	102	1.33E-15	1.31E-11	0.05	0.02	0.000	0.46	0.15	0.04	0.24	0.3	4.9	5.4	0.9	10	Gt	0.00	0.3
KAWF-1A	KAWF-1A_5CII	K1A5CII4	66	9.93E-16	1.50E-11	0.03	0.02	0.000	0.38	0.26	0.04	0.25	0.7	6.3	6.9	1.3	10	Gt	0.00	0.3
KAWF-1A	KAWF-1A_5CII	K1A5CII5	70	1.72E-15	2.46E-11	0.03	0.04	0.000	0.46	0.54	0.05	0.35	1.2	7.8	8.6	1.4	10	Gt	0.00	0.3
KAWF-1A	KAWF-1A_5CII	K1A5CII6	46	9.61E-16	2.09E-11	0.02	0.02	0.000	0.53	0.36	0.04	0.25	0.7	6.3	6.9	1.3	10	Gt	0.00	0.3
KAWF-1A	KAWF-1A_5D	K1A5D1	49	2.51E-15	5.12E-11	0.02	0.08	0.000	0.47	1.61	0.08	0.52	3.4	11.2	12.3	2.0	10	Gt-Ht-mix	0.26	2.8
KAWF-1A	KAWF-1A_5D	K1A5D2	30	1.76E-15	5.86E-11	0.01	0.05	0.000	0.43	1.51	0.08	0.52	3.5	13.9	15.3	2.6	10	Gt-Ht-mix	0.26	2.8
KAWF-1A	KAWF-1A_5D	K1A5D3	54	1.48E-15	2.74E-11	0.02	0.07	0.000	0.36	1.30	0.07	0.46	3.6	7.6	8.4	1.4	10	Gt-Ht-mix	0.26	2.8
KAWF-1A	KAWF-1A_5D	K1A5D4	33	1.10E-15	3.32E-11	0.02	0.05	0.000	0.46	1.48	0.08	0.56	3.2	7.6	8.4	1.5	10	Gt-Ht-mix	0.26	2.8
KAWF-2	KAWF-2_1BA	K21BA1	74	8.04E-15	1.09E-10	0.15	1.06	0.027	1.99	14.29	0.36	2.39	7.2	3.8	4.2	0.7	10	Gt	0.00	19.8
KAWF-2	KAWF-2_1BA	K21BA2	28	3.93E-15	1.40E-10	0.04	0.49	0.007	1.45	17.48	0.24	1.62	12.1	4.7	5.2	0.9	10	Gt	0.00	19.8
KAWF-2	KAWF-2_1BA	K21BA3	49	5.60E-15	1.14E-10	0.09	0.75	0.025	1.85	15.25	0.51	3.42	8.2	3.9	4.3	0.7	10	Gt	0.00	19.8
KAWF-2	KAWF-2_1BA	K21BA4	25	2.55E-15	1.02E-10	0.05	0.29	0.010	1.93	11.74	0.41	2.72	6.1	4.0	4.4	0.8	10	Gt	0.00	19.8
KAWF-2	KAWF-2_1BB	K21BB1	26	3.44E-15	1.32E-10	0.07	0.55	0.010	2.63	21.18	0.22	1.46	8.1	3.2	3.5	0.6	10	Gt-Ht-mix	0.47	18.5
KAWF-2	KAWF-2_1BB	K21BB2	34	3.98E-15	1.17E-10	0.10	0.48	0.010	3.04	14.25	0.28	1.83	4.7	3.4	3.7	0.6	10	Gt-Ht-mix	0.47	18.5
KAWF-2	KAWF-2_1BB	K21BB3	19	2.41E-15	1.27E-10	0.06	0.54	0.018	3.22	28.56	0.97	6.48	8.9	2.4	2.6	0.5	10	Gt-Ht-mix	0.47	18.5
KAWF-2	KAWF-2_1E	K21E2	48	7.00E-15	1.46E-10	0.04	0.60	0.020	0.73	12.40	0.50	3.32	16.9	7.4	7.8	1.0	5	Ht	0.86	
KAWF-2	KAWF-2_1E	K2i1E3	51	7.14E-15	1.40E-10	0.04	0.58	0.020	0.77	11.42	0.41	2.76	14.8	7.7	8.1	1.0	5	Ht	0.86	
KAWF-2	KAWF-2_1E	K2i1E4	58	1.25E-14	2.15E-10	0.13	1.43	0.040	2.21	24.70	0.61	4.04	11.2	4.9	5.1	0.6	5	Ht	0.86	
KAWF-2	KAWF-2_1E	K2i1E5	84	2.14E-14	2.55E-10	0.14	2.29	0.050	1.62	27.21	0.60	4.00	16.8	5.8	6.1	0.7	5	Ht	0.86	
KAWF-2	KAWF-2_1E	K2i1E6	82	1.47E-14	1.80E-10	0.11	1.84	0.050	1.31	22.42	0.61	4.07	17.1	5.0	5.3	0.6	5	Ht	0.86	
KAWF-2	KAWF-2_1EII	K1EII5	24	5.35E-15	2.23E-10	0.03	0.49	0.010	1.20	20.50	0.55	3.66	17.1	6.8	7.1	0.9	5	Ht		
KAWF-2	KAWF-2_1EII	K21EII1	47	8.25E-15	1.76E-10	0.06	1.19	0.020	1.26	25.36	0.42	2.79	20.1	4.5	4.7	0.6	5	Ht		
KAWF-2	KAWF-2_1EII	K21EII3	30	4.46E-15	1.49E-10	0.02	0.52	0.020	0.53	17.46	0.54	3.61	33.1	6.1	6.4	0.9	5	Ht		
KAWF-2	KAWF-2_1EII	K21EII4	23	5.04E-15	2.19E-10	0.01	0.41	0.010	0.64	17.96	0.54	3.57	28.0	8.3	8.7	1.2	5	Ht		
KAWF-2	KAWF-2_1HA	K21HA1	56	3.44E-15	6.13E-11	0.04	0.41	0.010	0.74	7.25	0.17	1.11	9.8	4.6	4.8	0.7	5	Gt-Ht-mix		
KAWF-2	KAWF-2_1HA	K21HA2	55	3.56E-15	6.48E-11	0.05	0.63	0.010	0.88	11.47	0.17	1.15	13.1	3.4	3.6	0.5	5	Gt-Ht-mix		
KAWF-2	KAWF-2_1HA	K21HA4	81	4.91E-15	6.06E-11	0.06	0.70	0.010	0.70	8.62	0.16	1.08	12.3	4.3	4.5	0.6	5	Gt-Ht-mix		
KAWF-2	KAWF-2_1HA	K21HA6	29	1.34E-15	4.63E-11	0.02	0.28	0.005	0.70	9.53	0.17	1.11	13.7	2.9	3.0	0.3	5	Gt-Ht-mix		
KAWF-2	KAWF-2_1HC	K21HC1	55	2.50E-15	4.54E-11	0.05	0.25	0.000	0.99	4.60	0.02	0.15	4.6	4.0	4.4	1.0	10	Gt		
KAWF-2	KAWF-2_1HC	K21HC2	56	8.48E-15	1.51E-10	0.11	0.71	0.010	2.04	12.67	0.27	1.78	6.2	5.6	6.2	1.0	10	Gt		
KAWF-2	KAWF-2_1J	K21J1	118	9.82E-15	8.32E-11	0.20	1.34	0.030	1.72	11.36	0.25	1.65	6.6	3.4	3.6	0.4	5	Ht	0.68	19.0
KAWF-2	KAWF-2_1J	K21J10	74	5.18E-15	6.99E-11	0.17	0.69	0.020	2.33	9.31	0.27	1.82	4.0	2.9	3.0	0.3	5	Ht	0.68	19.0
KAWF-2	KAWF-2_1J	K21J2	75	4.91E-15	6.54E-11	0.09	0.76	0.020	1.19	10.17	0.21	1.41	8.5	3.5	3.7	0.5	5	Ht	0.68	19.0
KAWF-2	KAWF-2_1J	K21J3	80	6.69E-15	8.37E-11	0.14	0.89	0.020	1.75	11.09	0.28	1.85	6.4	3.6	3.8	0.5	5	Ht	0.68	19.0
KAWF-2	KAWF-2_1J	K21J4	46	2.54E-15	5.53E-11	0.06	0.45	0.010	1.23	9.82	0.23	1.53	8.0	2.9	3.0	0.5	5	Ht	0.68	19.0
KAWF-2	KAWF-2_1J	K21J5	40	2.99E-15	7.47E-11	0.04	0.57	0.010	0.96	14.28	0.29	1.91	14.9	3.2	3.4	0.5	5	Ht	0.68	19.0
KAWF-2	KAWF-2_1J	K21J6	35	1.38E-15	3.94E-11	0.05	0.36	0.008	1.46	10.33	0.22	1.45	7.1	1.9	2.0	0.2	5	Ht	0.68	19.0
KAWF-2	KAWF-2_1J	K21J7	60	3.34E-15	5.57E-11	0.08	0.57	0.013	1.29	9.51	0.21	1.42	7.4	2.9	3.0	0.3	5	Ht	0.68	19.0
KAWF-2	KAWF-2_1J	K21J8	84	6.07E-15	7.22E-11	0.16	0.97	0.023	1.85	11.54	0.27	1.80	6.3	2.9	3.0	0.3	5	Ht	0.68	19.0
KAWF-2	KAWF-2_1J	K21J9	43	2.37E-15	5.52E-11	0.05	0.38	0.007	1.23	8.90	0.17	1.12	7.3	3.1	3.3	0.4	5	Ht	0.68	19.0
KAWF-2	KAWF-2_3A	K23A2	61	3.42E-15	5.60E-11	0.09	0.77	0.006	1.51	12.60	0.10	0.67	8.4	2.3	2.4	0.3	5	Ht	0.51	21.1
KAWF-2	KAWF-2_3A	K23A3	85	8.32E-15	9.79E-11	0.18	1.25	0.012	2.14	14.68	0.14	0.94	6.9	3.2	3.4	0.4	5	Ht	0.51	21.1
KAWF-2	KAWF-2_3A	K23A4	101	1.15E-14	1.14E-10	0.21	1.55	0.018	2.08	15.34	0.18	1.19	7.4	3.7	3.9	0.4	5	Ht	0.51	21.1

(*continued on next page*)

Table 3 (*continued*)1.

Sample	Subsample	Aliquot	Weight	^{4}He	^{4}He	^{238}U	^{232}Th	^{147}Sm	^{238}U	^{232}Th	^{147}Sm	Sm (total)	Th/U	Raw age	Corrected age	Error corrected age	Diffusion correction factor	Predominant mineral	RHG	Goethite Fe-Al-substitution
			μg	mol	mol/g	ng	ng	ng	ppm	ppm	ppm	ppm		Ma	Ma	Ma	%			mol%
KAWF-2	KAWF-2_3B	K23B1	50	7.68E-15	1.54E-10	0.06	0.99	0.005	1.27	19.73	0.09	0.61	15.5	4.8	5.0	0.6	5	Ht	0.77	12.1
KAWF-2	KAWF-2_3B	K23B2	85	5.57E-15	6.55E-11	0.08	1.11	0.018	0.94	13.10	0.21	1.40	13.9	3.0	3.2	0.4	5	Ht	0.77	12.1
KAWF-2	KAWF-2_3B	K23B3	102	1.03E-14	1.01E-10	0.11	1.43	0.004	1.08	14.04	0.04	0.26	13.0	4.3	4.5	0.5	5	Ht	0.77	12.1
KAWF-2	KAWF-2_3B	K23B4	118	1.51E-14	1.28E-10	0.15	2.15	0.010	1.29	18.22	0.09	0.58	14.1	4.2	4.4	0.5	5	Ht	0.77	12.1
KAWF-2	KAWF-2_3B	K23B5	135	1.22E-14	9.02E-11	0.14	0.97	0.001	1.07	7.20	0.01	0.07	6.7	6.0	6.3	0.7	5	Ht	0.77	12.1
KAWF-2	KAWF-2_3D	K23D2	121	1.12E-14	9.22E-11	0.17	1.88	0.030	1.37	15.57	0.24	1.63	11.4	3.5	3.7	0.4	5	Ht		
KAWF-2	KAWF-2_3D	K23D3	55	4.91E-15	8.92E-11	0.06	0.66	0.010	1.10	12.03	0.19	1.27	11.0	4.3	4.5	0.6	5	Ht		
KAWF-2	KAWF-2_3D	K23D6	48	3.52E-15	7.34E-11	0.05	0.49	0.010	1.11	10.24	0.17	1.13	9.2	3.8	4.0	0.6	5	Ht		
KAWF-2	KAWF-2_3D	K23D7	56	4.91E-15	8.76E-11	0.08	0.91	0.010	1.42	16.21	0.24	1.58	11.4	3.2	3.4	0.4	5	Ht		
KAWF-2	KAWF-2_3DB	K23DB1	37	3.03E-15	8.20E-11	0.07	0.72	0.010	2.02	19.52	0.22	1.45	9.7	2.3	2.5	0.5	10	Gt		
KAWF-2	KAWF-2_3DB	K23DB2	61	8.03E-15	1.32E-10	0.10	1.04	0.010	1.57	17.02	0.23	1.52	10.8	4.2	4.6	0.8	10	Gt		
KAWF-2	KAWF-2_3DB	K23DB3	67	9.82E-15	1.46E-10	0.17	1.93	0.030	2.48	28.76	0.46	3.07	11.6	2.9	3.2	0.5	10	Gt		
KAWF-2	KAWF-2_3DB	K23DB4	43	4.91E-15	1.14E-10	0.11	1.43	0.010	2.48	33.24	0.25	1.66	13.4	2.1	2.3	0.4	10	Gt		
KAWF-2	KAWF-2_3DIII	K23DIII1	121	3.03E-15	2.51E-11	0.21	2.00	0.040	1.75	16.52	0.31	2.09	9.4	< 0.8	< 0.8			Ht		
KAWF-2	KAWF-2_3DIII	K23DIII2	109	9.37E-15	8.60E-11	0.15	1.79	0.030	1.40	16.40	0.25	1.67	11.7	3.0	3.2	0.4	5	Ht		
KAWF-2	KAWF-2_3DIII	K23DIII3	62	4.46E-15	7.20E-11	0.07	0.82	0.020	1.10	13.20	0.25	1.69	12.1	3.3	3.5	0.5	5	Ht		
KAWF-2	KAWF-2_3DIII	K23DIII5	20	2.10E-15	1.05E-10	0.05	0.53	0.010	2.33	26.35	0.36	2.43	11.3	2.3	2.4	0.4	5	Ht		
KAWF-2	KAWF-2_3DIII	K23DIII6	31	2.19E-15	7.05E-11	0.05	0.57	0.010	1.70	18.30	0.30	2.02	10.8	2.2	2.3	0.4	5	Ht		
KAWF-2	KAWF-2_5AII	K25AII3	35	1.75E-15	5.00E-11	0.09	0.13	0.010	2.48	3.67	0.35	2.31	1.5	2.8	3.1	0.6	10	Gt	0.00	13.7
KAWF-2	KAWF-2_5AII	K25AII4	72	1.90E-15	2.65E-11	0.09	0.18	0.010	1.29	2.49	0.17	1.12	1.9	2.6	2.9	0.5	10	Gt	0.00	13.7
KAWF-2	KAWF-2_5AII	K25AII5	55	5.35E-16	9.73E-12	0.18	0.22	0.024	3.31	3.94	0.43	2.87	1.2	< 0.8	< 0.8			Gt	0.00	13.7
KAWF-3	KAWF-3_4A	K34A2	57	8.99E-16	1.58E-11	0.08	0.26	0.010	1.40	4.50	0.10	0.68	3.2	1.2	1.3	0.2	10	Gt		
KAWF-3	KAWF-3_4A	K34A3	88	2.24E-15	2.54E-11	0.11	0.31	0.010	1.30	3.51	0.11	0.71	2.7	2.2	2.4	0.4	10	Gt		
KAWF-3	KAWF-3_4A	K34A4	39	1.23E-15	3.15E-11	0.06	0.28	0.010	1.63	7.19	0.17	1.12	4.4	1.8	2.0	0.3	10	Gt		
KAWF-3	KAWF-3_4A	K34A7	54	5.63E-16	1.04E-11	0.03	0.03	0.000	0.64	0.55	0.08	0.52	0.9	2.5	2.8	0.6	10	Gt		
KAWF-4A	KAWF-4A_2A	K4A2A1	92	1.03E-14	1.12E-10	0.04	0.95	0.010	0.46	10.31	0.06	0.42	22.3	7.1	7.5	0.9	5	Ht	0.83	
KAWF-4A	KAWF-4A_2A	K4A2A2	84	1.29E-14	1.54E-10	0.06	1.09	0.010	0.77	12.96	0.08	0.56	16.8	7.3	7.7	0.9	5	Ht	0.83	
KAWF-4A	KAWF-4A_2A	K4A2A3	85	1.12E-14	1.31E-10	0.05	1.04	0.010	0.58	12.23	0.13	0.87	20.9	7.0	7.4	0.8	5	Ht	0.83	
KAWF-4A	KAWF-4A_2A	K4A2A4	65	7.58E-15	1.17E-10	0.04	1.63	0.000	0.62	25.01	0.06	0.40	40.5	3.2	3.4	0.4	5	Ht	0.83	
KAWF-4A	KAWF-4A_2A	K4A2A5	68	5.80E-15	8.53E-11	0.04	0.62	0.000	0.61	9.12	0.05	0.31	15.1	5.6	5.9	0.7	5	Ht	0.83	
KAWF-4A	KAWF-4A_3A	K4A3A2	65	2.63E-15	4.05E-11	0.05	0.03	0.010	0.74	0.54	0.09	0.57	0.7	8.6	9.5	2.1	10	Gt		
KAWF-4A	KAWF-4A_3A	K4A3A3	102	5.35E-15	5.25E-11	0.09	0.04	0.010	0.85	0.43	0.09	0.62	0.5	10.2	11.2	2.1	10	Gt		
KAWF-4A	KAWF-4A_3A	K4A3A4	33	1.47E-15	4.46E-11	0.02	0.01	0.000	0.71	0.32	0.10	0.66	0.5	10.7	11.8	3.2	10	Gt		
KAWF-4A	KAWF-4A_3A	K4A3A5	97	3.97E-15	4.09E-11	0.13	0.12	0.010	1.30	1.24	0.09	0.57	1.0	4.7	5.2	1.0	10	Gt		
KAWF-4A	KAWF-4A_3AII	K4A3AII1	40	2.81E-15	7.03E-11	0.04	0.03	0.000	0.96	0.84	0.12	0.78	0.9	11.1	12.2	2.7	10	Gt	0.02	5.6
KAWF-4A	KAWF-4A_3AII	K4A3AII3	49	2.23E-15	4.55E-11	0.03	0.07	0.000	0.69	1.34	0.09	0.62	1.9	8.3	9.1	2.1	10	Gt	0.02	5.6
KAWF-4A	KAWF-4A_3AII	K4A3AII4	69	3.93E-15	5.69E-11	0.05	0.05	0.010	0.77	0.68	0.21	1.40	0.9	11.4	12.5	2.5	10	Gt	0.02	5.6
KAWF-4A	KAWF-4A_3AII	K4A3AII6	32	1.74E-15	5.44E-11	0.04	0.06	0.010	1.12	1.72	0.20	1.32	1.5	6.6	7.3	1.7	10	Gt	0.02	5.6
KAWF-4A	KAWF-4A_3AII	K4A3AII8	70	3.61E-15	5.16E-11	0.08	0.09	0.010	1.18	1.23	0.11	0.71	1.0	6.5	7.2	1.4	10	Gt	0.02	5.6
KAWF-4B	KAWF-4B_1G	K4B1G1	47	2.39E-15	5.09E-11	0.09	0.46	0.010	1.84	9.85	0.19	1.26	5.3	2.3	2.4	0.3	5	Ht	0.50	19.4
KAWF-4B	KAWF-4B_1G	K4B1G2	62	3.23E-15	5.21E-11	0.14	0.65	0.010	2.19	10.47	0.21	1.40	4.8	2.1	2.2	0.2	5	Ht	0.50	19.4
KAWF-4B	KAWF-4B_1G	K4B1G3	63	3.18E-15	5.05E-11	0.09	0.60	0.010	1.47	9.49	0.18	1.23	6.5	2.5	2.6	0.3	5	Ht	0.50	19.4
KAWF-4B	KAWF-4B_1G	K4B1G5	90	4.44E-15	4.93E-11	0.16	0.93	0.020	1.73	10.39	0.24	1.63	6.0	2.2	2.3	0.2	5	Ht	0.50	19.4
KAWF-4B	KAWF-4B_1G	K4B1G6	84	3.89E-15	4.64E-11	0.12	0.86	0.020	1.46	10.23	0.20	1.32	7.0	2.2	2.3	0.2	5	Ht	0.50	19.4
KAWF-4B	KAWF-4B_1H	K4B1H1	160	1.25E-14	7.81E-11	0.29	2.81	0.040	1.79	17.55	0.25	1.66	9.8	2.5	2.6	0.3	5	Ht	0.83	
KAWF-4B	KAWF-4B_1H	K4B1H2	39	2.01E-15	5.15E-11	0.09	0.42	0.010	2.20	10.70	0.21	1.38	4.9	2.0	2.1	0.4	5	Ht	0.83	

KAWF-4B	KAWF-4B_1H	K4B1H3	66	4.91E-15	7.44E-11	0.09	0.98	0.010	1.39	14.82	0.22	1.44	10.7	2.9	3.0	0.4	5	Ht	0.83	
KAWF-4B	KAWF-4B_1H	K4B1H4	46	2.23E-15	4.85E-11	0.07	0.58	0.010	1.58	12.54	0.22	1.48	8.0	2.0	2.1	0.4	5	Ht	0.83	
KAWF-4B	KAWF-4B_1H	K4B1H5	36	1.52E-15	4.21E-11	0.04	0.34	0.010	1.21	9.47	0.17	1.14	7.8	2.3	2.4	0.5	5	Ht	0.83	
KAWF-4B	KAWF-4B_1H	K4B1H6	23	1.65E-15	7.18E-11	0.05	0.53	0.005	2.19	23.06	0.23	1.55	10.5	1.7	1.8	0.2	5	Ht	0.83	
KAWF-4B	KAWF-4B_1H	K4B1H7	45	1.95E-15	4.34E-11	0.09	0.58	0.010	1.90	12.79	0.23	1.53	6.7	1.6	1.7	0.2	5	Ht	0.83	
KAWF-5A	KAWF-5A_1A	K5A1A1	91	5.33E-15	5.86E-11	0.08	0.78	0.020	0.86	8.52	0.20	1.35	9.9	3.8	4.0	0.4	5	Ht	0.75	19.2
KAWF-5A	KAWF-5A_1A	K5A1A2	63	3.71E-15	5.88E-11	0.04	0.40	0.010	0.59	6.40	0.16	1.09	10.9	5.2	5.5	0.6	5	Ht	0.75	19.2
KAWF-5A	KAWF-5A_1A	K5A1A5	78	6.46E-15	8.29E-11	0.05	0.57	0.020	0.65	7.32	0.21	1.40	11.2	6.4	6.7	0.7	5	Ht	0.75	19.2
KAWF-5A	KAWF-5A_1A	K5A1A8	74	5.80E-15	7.83E-11	0.06	0.56	0.020	0.85	7.62	0.25	1.63	9.0	5.5	5.8	0.6	5	Ht	0.75	19.2
KAWF-5A	KAWF-5A_1B	K5A1B1	31	4.28E-16	1.38E-11	0.00	0.11	0.010	0.08	3.67	0.18	1.21	47.8	2.7	2.8	1.5	5	Ht	0.83	
KAWF-5A	KAWF-5A_1B	K5A1B2	56	5.80E-16	1.04E-11	0.00	0.16	0.000	0.05	2.78	0.06	0.42	55.0	2.6	2.7	1.1	5	Ht	0.83	
KAWF-5A	KAWF-5A_1B	K5A1B3	47	7.58E-16	1.61E-11	0.01	0.20	0.010	0.24	4.24	0.16	1.06	17.8	2.4	2.5	0.9	5	Ht	0.83	
KAWF-5A	KAWF-5A_1B	K5A1B5	52	1.18E-15	2.27E-11	0.02	0.22	0.005	0.40	4.25	0.10	0.69	10.7	3.0	3.2	0.4	5	Ht	0.83	
KAWF-5A	KAWF-5A_1B	K5A1B6	40	1.50E-15	3.75E-11	0.01	0.16	0.004	0.34	3.98	0.10	0.66	11.6	5.4	5.7	0.6	5	Ht	0.83	
KAWF-5A	KAWF-5A_2A	K5A2A1	53	1.56E-15	2.95E-11	0.08	0.45	0.010	1.50	8.50	0.30	2.00	5.8	1.6	1.8	0.4	10	Gt		
KAWF-5A	KAWF-5A_2A	K5A2A2	42	1.43E-15	3.40E-11	0.07	0.34	0.010	1.60	8.00	0.30	2.00	5.0	1.8	2.0	0.4	10	Gt		
KAWF-5A	KAWF-5A_2A	K5A2A3	81	2.14E-15	2.64E-11	0.14	0.65	0.020	1.70	8.10	0.30	2.00	4.7	1.3	1.4	0.3	10	Gt		
KAWF-5A	KAWF-5A_2A	K5A2A4	63	3.84E-15	6.09E-11	0.08	0.33	0.020	1.30	5.20	0.30	2.00	4.1	4.5	5.0	0.8	10	Gt		
KAWF-5A	KAWF-5A_2A	K5A2A5	55	8.64E-16	1.57E-11	0.03	0.16	0.000	0.59	2.91	0.07	0.47	4.9	2.3	2.5	0.6	10	Gt		
KAWF-5A	KAWF-5A_2B	K5A2B1	74	6.25E-15	8.44E-11	0.05	0.22	0.000	0.70	3.00	0.00	0.00	4.4	11.1	11.7	1.3	5	Gt-Ht-mix		
KAWF-5A	KAWF-5A_2B	K5A2B2	90	1.70E-15	1.88E-11	0.08	0.62	0.030	0.90	6.80	0.40	2.67	7.6	1.4	1.5	0.2	5	Gt-Ht-mix		
KAWF-5A	KAWF-5A_2B	K5A2B3	32	3.66E-15	1.14E-10	0.07	0.18	0.010	2.10	5.60	0.50	3.33	2.7	6.3	6.6	0.8	5	Gt-Ht-mix		
KAWF-5A	KAWF-5A_2B	K5A2B4	26	1.43E-15	5.50E-11	0.02	0.12	0.010	0.74	4.60	0.23	1.53	6.2	5.6	5.8	0.9	5	Gt-Ht-mix		
KAWF-5A	KAWF-5A_2C	K5A2C1	36	2.50E-15	6.94E-11	0.04	0.23	0.020	1.10	6.40	0.60	4.00	5.9	5.0	5.3	0.7	5	Ht		
KAWF-5A	KAWF-5A_2C	K5A2C2	25	1.87E-15	7.50E-11	0.01	0.08	0.000	0.50	3.30	0.00	0.00	6.6	10.9	11.4	1.6	5	Ht		
KAWF-5A	KAWF-5A_2C	K5A2C3	20	5.35E-16	2.68E-11	0.01	0.15	0.000	0.40	7.50	0.20	1.33	18.0	2.4	2.5	0.6	5	Ht		
KAWF-5A	KAWF-5A_3AII	K5A3AII1	87	1.20E-14	1.38E-10	0.08	0.34	0.000	0.93	3.89	0.05	0.32	4.2	13.7	15.1	2.5	10	Gt	0.00	4.8
KAWF-5A	KAWF-5A_3AII	K5A3AII2	49	8.03E-15	1.64E-10	0.13	0.17	0.010	2.75	3.42	0.14	0.93	1.2	8.4	9.2	1.6	10	Gt	0.00	4.8
KAWF-5A	KAWF-5A_3AII	K5A3AII3	35	8.16E-15	2.33E-10	0.12	0.10	0.010	3.35	2.98	0.19	1.28	0.9	10.7	11.8	2.0	10	Gt	0.00	4.8
KAWF-5A	KAWF-5A_3AII	K5A3AII4	58	8.92E-15	1.54E-10	0.14	0.14	0.010	2.39	2.41	0.12	0.79	1.0	9.5	10.5	1.8	10	Gt	0.00	4.8
KAWF-5A	KAWF-5A_3AII	K5A3AII5	56	1.04E-14	1.86E-10	0.18	0.17	0.007	3.17	3.06	0.12	0.83	1.0	8.9	9.8	1.5	10	Gt	0.00	4.8
KAWF-5A	KAWF-5A_3AII	K5A3AII6	40	9.46E-15	2.36E-10	0.12	0.14	0.006	3.07	3.50	0.14	0.92	1.1	11.2	12.3	1.9	10	Gt	0.00	4.8
KAWF-5A	KAWF-5A_3AII	K5A3AII7	48	6.02E-15	1.25E-10	0.11	0.16	0.005	2.29	3.30	0.11	0.75	1.4	7.6	8.4	1.3	10	Gt	0.00	4.8
KAWF-5B	KAWF-5B_1B	K5B1B1	63	8.05E-15	1.28E-10	0.12	0.10	0.006	1.93	1.61	0.10	0.64	0.8	10.3	10.8	1.2	5	Gt-Ht-mix	0.51	4.5
KAWF-5B	KAWF-5B_1B	K5B1B2	86	1.39E-14	1.61E-10	0.28	0.15	0.006	3.23	1.77	0.07	0.45	0.5	8.2	8.6	0.9	5	Gt-Ht-mix	0.51	4.5
KAWF-5B	KAWF-5B_1B	K5B1B3	78	2.63E-15	3.37E-11	0.16	0.14	0.006	2.05	1.82	0.08	0.51	0.9	2.5	2.6	0.3	5	Gt-Ht-mix	0.51	4.5
KAWF-5B	KAWF-5B_1B	K5B1B5	111	5.40E-15	4.86E-11	0.13	0.17	0.010	1.15	1.50	0.09	0.60	1.3	6.0	6.3	0.7	5	Gt-Ht-mix	0.51	4.5
KAWF-5B	KAWF-5B_2AII	K5B2AII1	110	1.96E-14	1.78E-10	0.34	0.08	0.010	3.08	0.75	0.12	0.81	0.2	10.1	11.1	1.8	10	Gt	0.13	3.8
KAWF-5B	KAWF-5B_2AII	K5B2AII2	100	2.81E-14	2.81E-10	0.46	0.48	0.020	4.59	4.81	0.17	1.15	1.0	9.1	10.0	1.6	10	Gt	0.13	3.8
KAWF-5B	KAWF-5B_2AII	K5B2AII4	50	1.47E-14	2.94E-10	0.21	0.22	0.010	4.17	4.45	0.23	1.51	1.1	10.6	11.7	1.9	10	Gt	0.13	3.8
KAWF-5B	KAWF-5B_2AII	K5B2AII5	57	1.47E-14	2.58E-10	0.19	0.18	0.010	3.39	3.09	0.14	0.93	0.9	11.5	12.7	2.0	10	Gt	0.13	3.8
KAWF-5B	KAWF-5B_2AII	K5B2AII6	87	1.96E-14	2.26E-10	0.32	0.10	0.010	3.71	1.17	0.09	0.62	0.3	10.5	11.6	1.8	10	Gt	0.13	3.8
KAWF-5B	KAWF-5B_3B	K5B3B1	48	7.14E-15	1.49E-10	0.08	0.26	0.000	1.60	5.33	0.08	0.53	3.3	9.4	10.3	1.8	10	Gt	0.00	5.0
KAWF-5B	KAWF-5B_3B	K5B3B2	57	1.47E-14	2.58E-10	0.18	0.38	0.010	3.10	6.59	0.11	0.75	2.1	10.1	11.1	1.8	10	Gt	0.00	5.0
KAWF-5B	KAWF-5B_3B	K5B3B3	69	9.82E-15	1.42E-10	0.15	0.43	0.010	2.11	6.16	0.11	0.71	2.9	7.6	8.4	1.4	10	Gt	0.00	5.0
KAWF-5B	KAWF-5B_3B	K5B3B4	85	2.14E-14	2.52E-10	0.30	0.76	0.010	3.52	8.92	0.11	0.73	2.5	8.3	9.1	1.4	10	Gt	0.00	5.0
KAWF-5B	KAWF-5B_3B	K5B3B5	52	1.75E-14	3.37E-10	0.21	0.35	0.007	3.96	6.69	0.14	0.95	1.7	11.3	12.4	1.9	10	Gt	0.00	5.0
KAWF-5B	KAWF-5B_3B	K5B3B6	52	1.37E-14	2.64E-10	0.22	0.41	0.006	4.33	7.92	0.11	0.74	1.8	7.9	8.7	1.4	10	Gt	0.00	5.0

6.2. (U-Th)/He ages, mineralogy and chemistry variation: insight for dissolution and recrystallisation processes

The comparison of the mineralogy and mineral chemistry with the age data gives insight into the evolution of the duricrust system. The oldest ages (30–25 Ma), obtained on subsamples from samples CDR-02 and CDR-01, are composed of hematite with none or very few goethite (see Table 3, Figs. 7 and 9B). These subsamples have (compared to the other subsamples) low U concentrations and very low to intermediate Th concentrations (see Figs. 5 and 9C). Goethite starts to precipitate since ca. 25–20 Ma (CDR-04A_3B) but is more common since ca. 14 to 13 Ma (KAWF-5 and KAWF-4, Fig. 9B). These early goethite subsamples are very Al poor (2–6 mol%) and contain only small amounts of hematite (Figs. 7 and 9D). Most of them have high U and low to intermediate Th concentrations (see yellow squares in Figs. 5, 6F and 6G). Since ca. 13–10 Ma, hematite and goethite are more intimately mixed (Fig. 7C) and goethite gets increasingly enriched in Al. The subsamples with ages < 5 Ma are predominantly composed of goethite (Fig. 9B) and these young goethite subsamples contain the highest amounts of Al-substitution (Fig. 9D). From 10-8 Ma on, U and Th concentrations get more diverse and increase in some subsamples (Figs. 5B, 5C and 9C).

The observed temporal evolution of the Al-rich hematite and goethite minerals seems to highlight important insight into the weathering processes. The Al-content and stability of hematite and goethite are strongly linked to the activity of water, the elements (Si, Al, Fe) in solution, the minerals they are associated with (kaolinite, gibbsite, quartz), the temperature and the grain size as shown by Tardy and Nahon (1985); Trolard and Tardy (1987) and Tardy (1997) who studied in detail Al-goethite and Al-hematite in ferricretes (iron crusts) and bauxites. On the scale of a lateritic weathering profile, Al-substitutions in goethite and hematite increase from the bottom to the top (Fitzpatrick and Schwertmann, 1982; Fritsch et al., 2005). When percolating fluids are rich in silica, Al-substitution in hematite and goethite is low and kaolinite forms. Tardy and Nahon (1985) propose that primary hematite

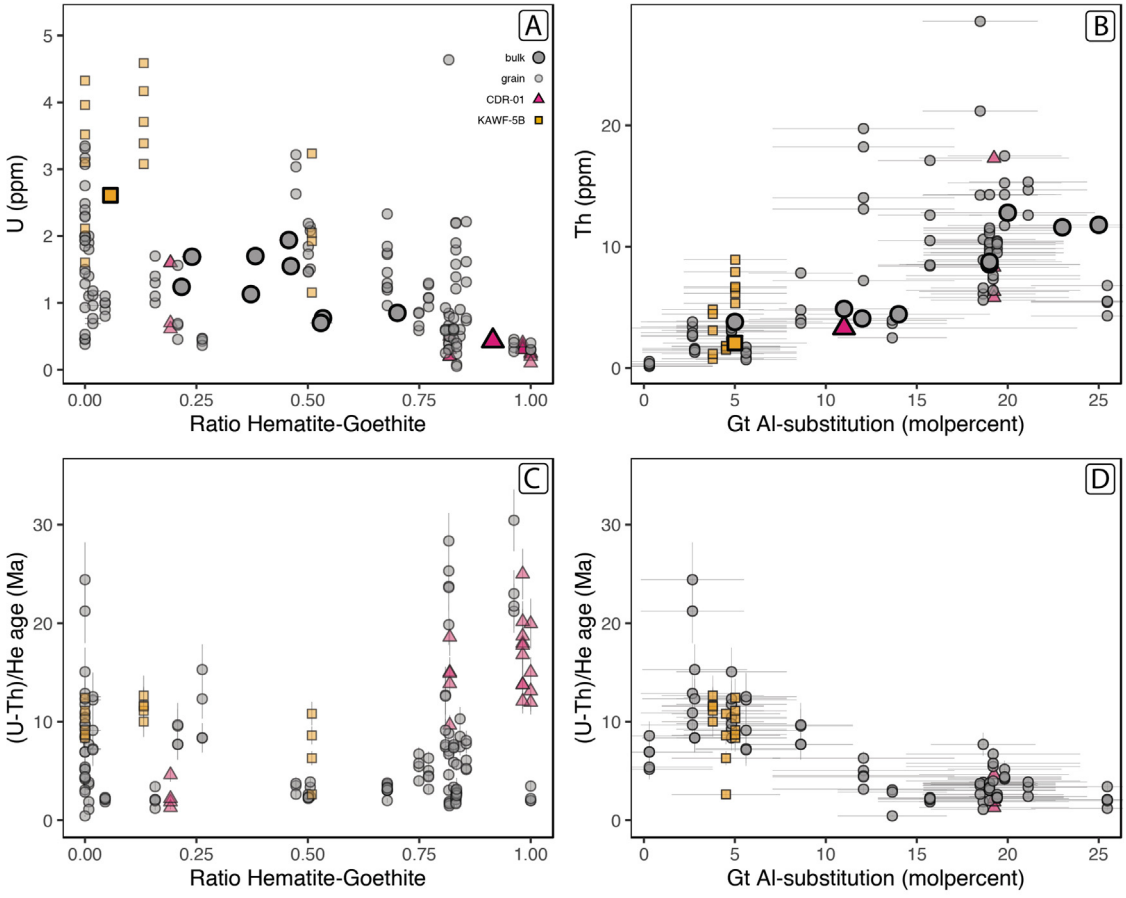

Fig. 7. Relation of mineralogy and (U-Th)/He data for the analyzed samples and subsample. (A): Ratio hematite-goethite, calculated as hematite (wt%)/(hematite(wt%) + goethite (wt%)), versus U concentration in bulk samples and dated grains. (B) shows the Th concentration of the bulk samples and dated grains versus the Al-substitution in goethite for samples and subsamples containing more than 20% goethite. (C) presents the obtained (U-Th)/He ages versus the ratio hematite-goethite, (D) shows (U-Th)/He ages versus Al-substitution in goethite for subsamples containing more than 20% goethite. Pink triangles correspond to sample CDR-01, yellow squares to sample KAWF-5B, grey circles to all other samples. Note that mineralogical data was only obtained for a subset of the dated subsamples.

forms mainly in small pore spaces associated with kaolinite. When conditions get undersaturated and kaolinite gets unstable and is slowly replaced by hematite, the hematite gets richer in Al. Al-rich goethite forms in the first stages of the rehydration of Al-rich hematite, the highest Al-substitutions in goethite occur with the maximum dissolution of kaolinite. When percolating fluids are Si-poor and Al-rich, Al-goethite precipitates together with gibbsite. Tardy and Nahon (1985) report 2–20 mol% Al-substitution in goethite when the latter is associated with kaolinite in ferricretes and 18–27 mol% Al-substitution when it is associated with gibbsite in bauxites. For bauxites, Bardossy and Aleva (1990) describe high Al-substitution in primary goethite and hematite (i.e. formed with gibbsite /

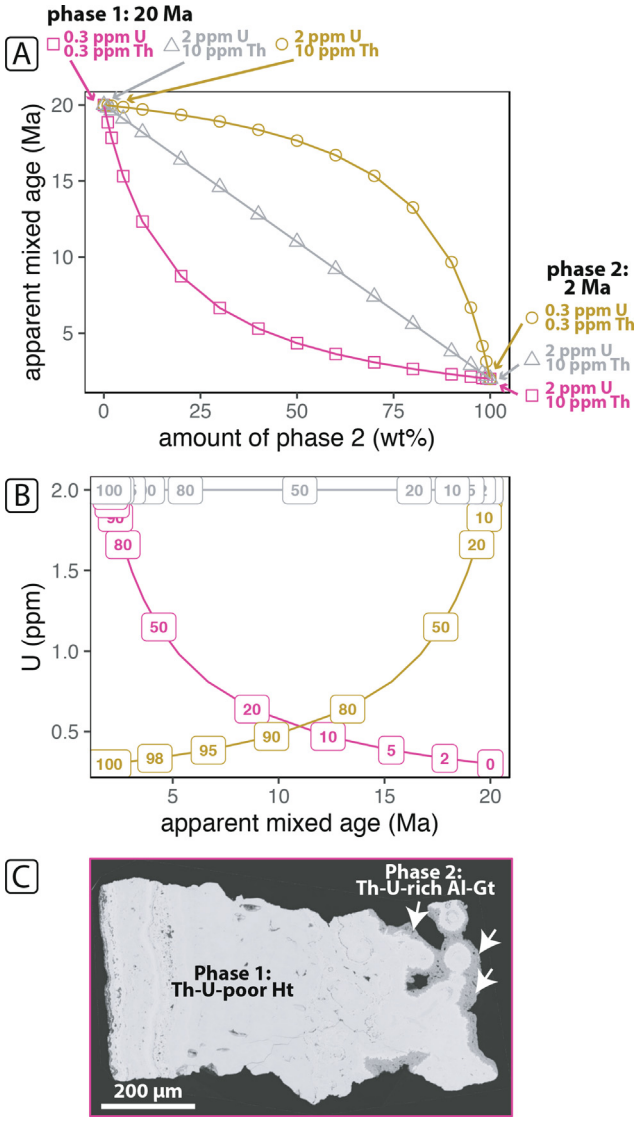

Fig. 8. Theoretical phase mixing scenarios of two phases with different ages, 20 Ma and 2 Ma, and different actinide concentrations. (A) shows the mixed apparent ages which would be measured as a function of the percentage of phase 2. Actinide concentrations for all phases and scenarios are indicated in the corresponding colors. The evolution of the age varies strongly in between the different scenarios. When actinide concentrations are lower in phase 1 than in phase 2 (pink rectangles), the age drops quickly even with low amounts of phase 2. When phase 1 is richer in actinides than phase 2 (yellow circles), the age drops slowly in the beginning and very fast at the end. For equal concentrations in both phases (grey triangles), the relation between age and proportion of phase 2 is linear. B shows the apparent mixed ages relative to the total U concentrations, colors are as in A. The labels indicate the percentage of phase 2 in the mixing. For scenario 1 (pink rectangles) the addition of 10% of phase 2 leads to drop of age from 20 to 10 Ma whereas in scenario 2 (yellow circles) an amount of 60% of phase 2 lead only to a minor drop from 20 Ma to 18 Ma. The graph for Th vs mixed age looks very similar and can be found together with the Th/U graph in Fig. A13 of the Electronic Supplement. (C) shows an example of a grain composed mainly of Th and U poor Hematite but which shows a small Gt rim (see white arrows). We suppose that these rims observed in some of the grains of subsample CDR-01B_3 are composed of late stage U and Th rich Al Gt and led to the dispersed ages of this subsample which correlate with U and Th. Assumed endmember ages and actinide concentrations resemble those of scenario 1.

boehmite) and low Al-substitution in secondary goethite and hematite such as fissure fillings or crusts.

This allows some important interpretations regarding the conditions of sample formation. The first hematite subsamples, which precipitated since 30 Ma, formed while kaolinite was stable, possibly even in equilibrium with the latter, in line with the mechanism proposed by Tardy and Nahon (1985). The kaolinite minerals were completely dissolved later and only their phantoms remain (Fig. 4C and 4D). The oldest goethite subsamples are Al-poor with Al-substitutions < 6 mol% (Fig. 9D), indicating stability with kaolinite and absence of gibbsite. Only since ca. 8 Ma Al-rich goethite precipitates, and the Al-contents in goethite increase towards younger ages (Fig. 9D). High Al-substitutions in goethite can be found in coatings of small pisoliths and the outermost coatings, i.e. where rehydration happens, as well as in the matrix where goethite is associated with gibbsite. The sample textures indicate many dissolution and reprecipitation cycles. This might also lead to a local enrichment of Al if the more mobile Fe is lixiviated and the less mobile Al reprecipitates at the same place. The amount of Fe in the solution can either be completely removed from the system or reprecipitate elsewhere in form of very pure, Al-poor goethite (for example KAWF-1A_5CII).

The Th and U concentrations of the dated grains give equally some information on the precipitation conditions of the Fe-minerals. Th is a very immobile element and, as can be seen in Fig. 7B, shows a very similar behavior as Al. The first subsamples show rather low concentrations of Th < 10 ppm (Figs. 5C and 9C, median Th concentration for grains > 10 Ma = 1.7 ppm Th). Since 10 Ma, Th concentrations and also Th/U ratios start to increase (median Th concentration for grains < 10 Ma = 7.3 ppm Th). The highest Th concentrations (10–33 ppm Th) can be found in small pisoliths which are in the process of rehydration and in the outermost rehydration coatings. The lowest Th concentrations (<0.5 ppm) can be found in the very pure, Al-poor botryoidal goethite and hematite of subsamples KAWF-1A_5CII and CDR-01_3 (Fig. 6C, Table 3). While Al can come either from the dissolution of kaolinite or dissolution/reprecipitation cycles of Fe minerals, the Th enrichment and the increase of the Th/U ratio we can observe since 10 Ma are probably due to dissolution/reprecipitation cycles of Fe minerals as kaolinite does not incorporate significant quantities of Th (Braun et al., 1993). The increase in Th (and Al) indicates therefore that there is an increase of dissolution/reprecipitation cycles of Fe minerals since 10 Ma (Fig. 9).

On the contrary, U shows a different behavior than Th. U concentrations are not linked to the Al-content of goethite but seem to be linked to the amount of goethite compared to hematite, indicating that U is mainly contained in goethite (Fig. 7A). Under oxidizing conditions U forms Uranyl, which is much more mobile than Th and is transported with the fluids. The strong affinity of U for iron oxides is well documented as well in adsorption as in coprecipitation contexts (Hsi and Langmuir, 1985; Manceau et al., 1992; Bruno et al., 1995). Thus, Fe minerals precipitated directly from the fluids with a high water activity might be more prone to be U-rich. This could explain why goethite is generally U richer and hematite, which forms with relatively low water activity, either in small pores or from dehydration of Gt, tends to be U poorer.

6.3. Timing of lateritization and bauxitization and relation with local geomorphology

Low-temperature thermochronological studies from rocks from the basement of the Guiana Shield in north eastern French Guiana indicate that the rocks are exhumed close to the surface at ca. 90 Ma (Derycke et al., 2021). This age can be regarded as maximum age constraint for the onset of weathering processes. The (U-Th)/He ages

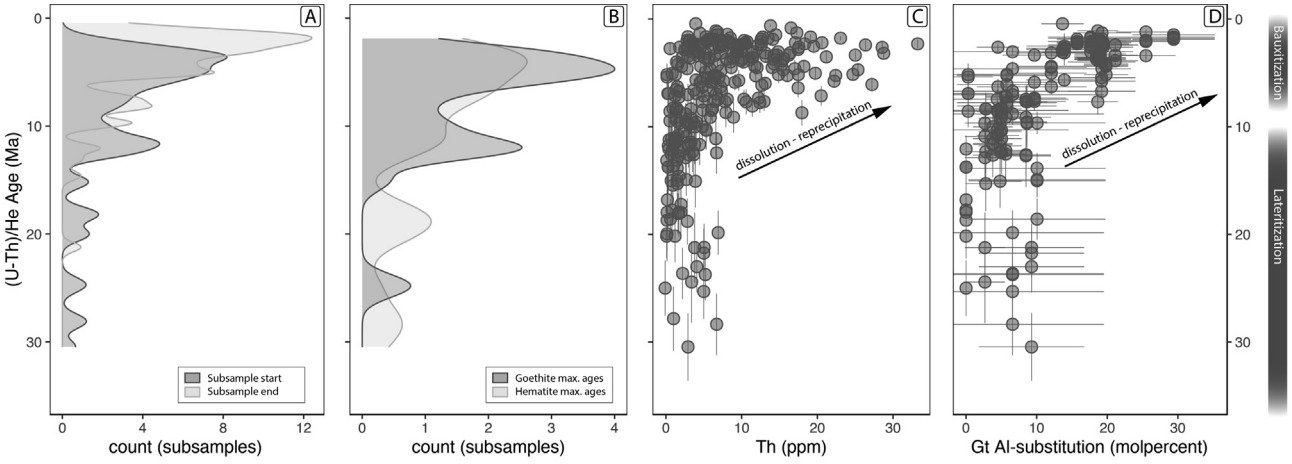

Fig. 9. (A) Shows Kernel density estimates of the maximum (dark gray) and minimum (bright gray) ages of our dated subsamples. (B) shows Kernel density estimates of the maximum ages of hematite (bright gray) and goethite (dark gray) subsamples. Very mixed subsamples (predominant mineral in Table 3 = hematite-goethite-mix) are not represented. (C) shows Th concentrations vs (U-Th)/He ages for all dated grains. (D) shows (U-Th)/He ages versus Al-substitution in goethite for subsamples analysed by micro-XRD with more than 20% goethite. Al-substitutions are mean values by subsample whereas all (U-Th)/He ages for these subsamples are plotted.

obtained in our study show that surface weathering on Kaw mountain started at least at the beginning of the Oligocene (oldest ages found in our samples). However, these ages have to be considered as minimum age constraint for the onset of weathering. To form a lateritic profile with a duricrust and (more or less) well-crystallized hematite and goethite, it needs a favorable climate and time (Beauvais and Colin, 1993; Vasconcelos et al., 2015). The age of the oldest duricrusts will thus not correspond to the onset of weathering.

The (U-Th)/He results do not provide any information on what happened in between 90 and 30 Ma. It is possible that older Fe minerals exist in the duricrust of Kaw mountain but that we did not sample them. The different age distributions in our samples show how much the samples vary in terms of age and composition. Furthermore, it is very likely that older Fe minerals were not preserved as they got dissolved later on. Tardy (1997) explains that in an evolving duricrusted lateritic profile, the duricrust is formed lower, at the interface with the fluctuating water table, while it is degraded/dismantled higher in the profile at the interface with the soil cover. Owing to this degradation/dismanteling process, Fe migrates downwards and the duricrust gets rejuvenated at its bottom (e.g. Beauvais (1999) and Beauvais (2009) who described this degradation process resulting in a secondary ferruginisation front migrating downward in lateritic profiles in Central Africa). Therefore, lateritic duricrust gets younger at its bottom and older at its top. This constant rejuvenation of the duricrust is then one reason why old ages might not be preserved in an evolving duricrust system.

The overall age distribution (Fig. 10) of our results which shows a more or less exponential decrease towards older ages and resembles in its general shape those of other authors (Monteiro et al., 2014, 2018; dos Santos Albuquerque et al., 2020) could result from (more or less)

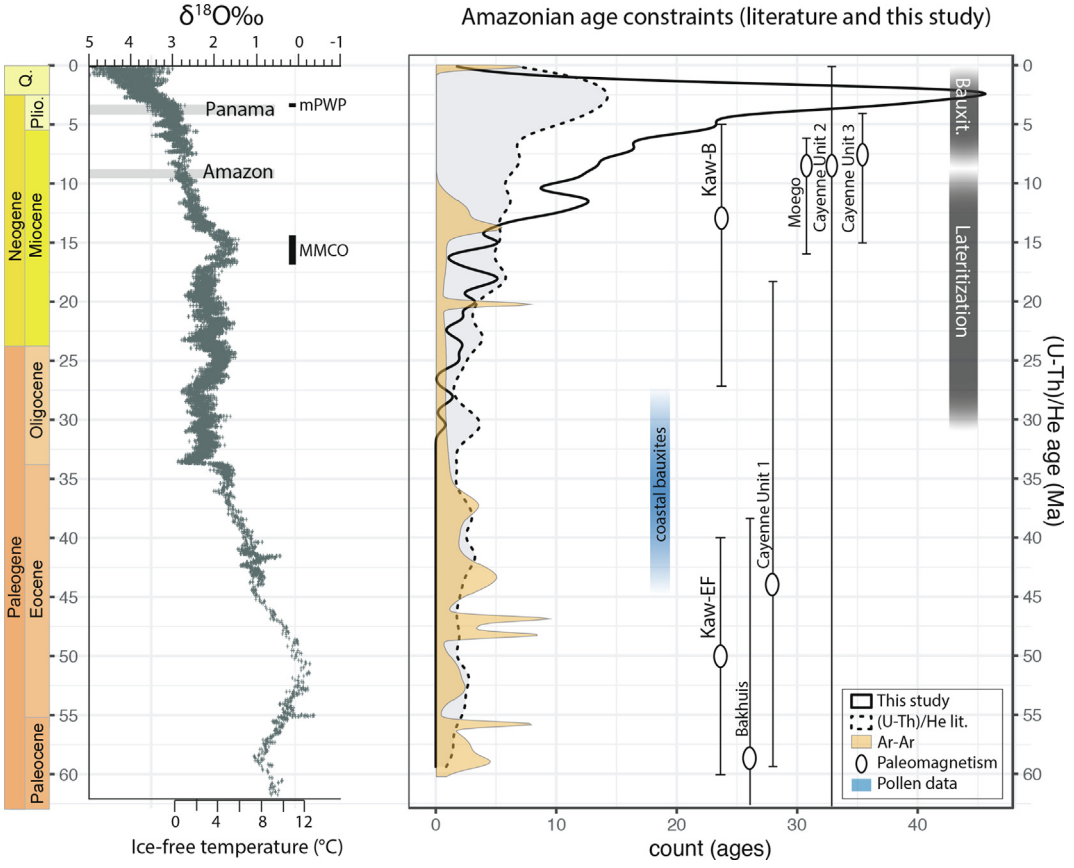

Fig. 10. Compilation of available climate data, main geologic events in Amazonia, published geochronological data and our new data for the last 60 Myr. $\delta^{18}O$ data from Zachos et al. (2008) is a proxy for the global temperature, MMCO = Middle Miocene Climate Optimum, mPWP = mid-Pliocene Warm Period. Age constraints for laterites and bauxites in Amazonia: Black solid line: Kernel density distribution of our age data. Literature data: the grey dashed Kernel density curve shows the available (U-Th)/He ages of supergene Fe- and Mn minerals from the Amazon craton from (Shuster et al., 2012; Allard et al., 2018; Monteiro et al., 2018; dos Santos Albuquerque et al., 2020). Note that only ages < 60 Ma are shown. Data from Shuster et al. (2005) is not plotted as their samples are included in the dataset of Monteiro et al. (2018). Orange density curve: probability density plot of the ^{39}Ar-^{40}Ar data of Vasconcelos et al. (1994) and Ruffet et al. (1996) on the Southern part of the Amazon craton. Where available, plateau ages where used, otherwise isochron ages. Ellipses with vertical error bars: paleomagnetism ages of Théveniaut and Freyssinet (2002) for different sites in French Guiana (including Kaw) and Suriname. Note that the location of "KAW-EF" is at ca. 300 m elevation and location of "KAW-B" at ca. 220 m. The blue bar shows the supposed age of the coastal bauxites in Suriname and Guyana (Hammen and Wymstra, 1964; Bardossy and Aleva, 1990).

continuous weathering with permanent dissolution and reprecipitation cycles under relatively constant conditions. However, our petrological, mineralogical and geochemical results allow a deeper insight and imply an important change in the weathering conditions. From our results, a lateritic system with precipitation of ferruginous duricrust has been set in place at the beginning of the Oligocene. Weathering probably continued during the Oligocene and Early Miocene but, from the few ages we obtain between 30 and 14 Ma (probably many of them being mixed ages), it is impossible to identify discrete events. Subsample onsets (i.e. maximum ages) are at 30–27 Ma (CDR-02), 25–24 Ma (CDR-01 and CDR-04C), 20–18 Ma, around 15 Ma and, more significantly, from ~ 14 to 13 Ma on (Fig. 9A). The maximum age peak at ~ 12 Ma, that postdates the Middle Miocene Climate Optimum (MMCO, 17–14.5 Ma (Flower, 1999; Herold et al., 2011)) by 2–3 Myr, could indicate very favorable weathering conditions (Fig. 9). As explained in Section 6.2, these old subsamples crystallized while kaolinite was stable without incorporating major amount of Al, indicating the presence of a "classical"/ ferruginous lateritic system without formation of gibbsite and / or bauxite (Fig. 9). The distribution of hematite and goethite within this period of ferruginous lateritization, with a predominance of hematite from 30 to 14 Ma and Al-poor goethite appearing significantly only since ~ 14 Ma (Fig. 9B), indicates, that the climate might have developed from hotter and/or more arid seasonally contrasted monsoonal climate with preferential precipitation of hematite to more humid (and/or eventually cooler) seasonally contrasted monsoonal climate with preferential precipitation of goethite (Trolard and Tardy, 1987; Tardy and Roquin, 1998).

The 10–8 Ma period seems to record a change towards more intense weathering conditions which peak at 6–2 Ma. Under these intense weathering conditions kaolinite got unstable, Fe-mineral recycling became faster and the formerly ferruginous laterite was bauxitized. Whether weathering was continuous or characterized by discrete events during the last 10 Myr is not possible to say from our data. Both a continuous intensification of weathering since 10 Ma with a peak between 6 and 2 Ma as well as a short-lasting bauxitization event at ca. 3–2 Ma associated with strong mineral recycling could produce the observed results. The intense phase mixing makes a differentiation of the two processes impossible.

Ages > 15 Ma are obtained exclusively in samples collected on the northern flank of the mountain ridge (Fig. 5A). This flank is more exposed to the predominant wind directions and is closer to the sea, possibly leading to higher precipitations. Bardossy and Aleva (1990) observe at other bauxite sites more alteration on elevated luv-sides than on lee-sides. Spatial distribution of ages > 15 Ma only on NE flank could either be a sampling effect or indicate that conditions favorable for Fe-duricrust formation were set in place earlier on the NE flank than on the SW flank. With the available sampling material, this question cannot be answered.

There is no significant difference between the samples collected at the top and those coming from the flanks of the ridge. However, KAWF-1, which was sampled from a giant detached block, shows some different features compared to the other samples, notably the abundance of kaolinite, the scarcity of gibbsite and young ages < 5 Ma. This could indicate a disconnection, i.e. break off, from the overall duricrust system at the beginning of the bauxitization phase through dissolution of an important amount of material just below the duricrust. The stair-like morphology observed on the flanks of Kaw mountain (Choubert, 1956), as well as the caves which exist below the duricrust at several places, might be related to the same phenomenon which could thus be synchronous to the bauxitization at the end of Neogene.

6.4. Regional and climatic context of the lateritization and bauxitization of Kaw Mountain

6.4.1. Comparison with available age data: highlighting the climate signals

Fig. 10 compares the results obtained in this study with available geochronological data from Amazonia. While all existing (U-Th)/He data correspond to sites faraway (>1000 km) from our study area, the paleomagnetism data of Théveniaut and Freyssinet (2002) were obtained on Kaw mountain and nearby duricrusts in French Guiana and Suriname. For Kaw, the authors obtain ages of ca. 50 ± 10 Ma, 13–10 Ma and very recent ages. A Mid to Late Miocene age obtained on a sample from lower elevations (220 m) of Kaw mountain is very similar to the age peak we observed in our dataset at ca. 14–12 Ma. Three other samples from Kaw of Théveniaut and Freyssinet (2002) yield magnetic poles which fall in between the 10 Ma paleopole and the recent magnetic pole (Fig. 10). While the authors assign these results to recent reworking on top of the duricrust, it is possible that this signal is related to the intense weathering phase we observe in our samples in the late Neogene. Their results for the low elevation units in the Cayenne area (Cayenne Units 2 and 3, Fig. 10) and from the Surinamese Moengo deposit with values of ca. 10–8 Ma show an overlap with our data. Due to the large uncertainty of paleomagnetism ages however, a more detailed comparison is not possible.

The available (U-Th)/He and ^{40}Ar-^{39}Ar data from supergene Fe and Mn oxides from Amazonia (Vasconcelos et al., 1994; Ruffet et al., 1996; Shuster et al., 2005, 2012; Allard et al., 2018; Monteiro et al., 2018; dos Santos Albuquerque et al., 2020) presented in Fig. 10 derive from areas more than 1000 km away from Kaw mountain and located mainly South of the Amazon River. Different from our data, most of the aforementioned studies comprise much older ages spanning over large parts of the Cenozoic up to the Paleozoic (dos Santos Albuquerque et al., 2020). Although the compilation of all (U-Th)/He data (Fig. 10) shows an increase in age density since the Pliocene, this feature is much less pronounced in the literature data when compared to our dataset. Age density curves are obviously biased by the number of aliquots dated per subsample and the chosen subsamples and should therefore not be overinterpreted. Nevertheless,

the comparison shows the importance of the Late Neogene bauxitization event for our samples. In any case, the comparably older ages obtained from the high elevation samples (ca. 700 m) from the Carajás area (Vasconcelos et al., 1994; Ruffet et al., 1996; Shuster et al., 2005, 2012; Monteiro et al., 2018) are consistent with the geomorphological models, which sustain the idea of older surface ages on high elevation surfaces and younger ages in low elevation surfaces (Choubert, 1957; King, 1962; McConnell, 1968; Blancaneaux, 1981; Bardossy and Aleva, 1990; Briceño and Schubert, 1990).

The ^{40}Ar-^{39}Ar data by Vasconcelos et al. (1994) and Ruffet et al. (1996) show a peak at 15–10 Ma, similar to the peak we observe in our data at 14–12 Ma. Note that this peak is just shortly after the MMCO (17–14.5 Ma). The δ^{18}O isotope curve (Zachos et al., 2008) in Fig. 10 indicates a general temperature decrease since the MMCO. This is compatible with or observed hematite-goethite distribution (Fig. 9B) which could result either from a shift from more arid (ca. 30 to 14 Ma) to more humid climate (since $\sim$ 14 Ma) or from a decrease in temperature with higher temperatures from 30 to 14 Ma and lower temperatures since $\sim$ 14 Ma (Trolard and Tardy, 1987; Tardy and Roquin, 1998).

Despite of the general temperature decrease since the MMCO, periods of warm climate (with global mean temperatures 2–4 °C higher than those of preindustrial climate) existed during the Pliocene, notably during the Pliocene Climatic Optimum (ca. 4.4–4.0 Ma, Fedorov et al., 2013) and the mid-Pliocene Warm Period (mPWP, 3.3–3.0 Ma, (Haywood et al., 2013). During the mPWP the intertropical convergence zone was shifted northwards leading to a dryer South American Summer Monsoon over intertropical South America (Pontes et al., 2020) but eventually increasing precipitations north of the equator and accelerating weathering in the Guianas. Our proposed bauxitization could thus be linked to increased precipitation during the mPWP.

6.4.2. Comparison with other bauxites of the Amazonian craton

Most of the bauxites of the coastal plain in Guyana and Suriname are underlain and capped by sediments. Detailed sedimentological palynological studies of the under- and overlaying sediments (Hammen and Wymstra, 1964; Wymstra, 1971) allow the determination of a Late Eocene to Oligocene age of the bauxitization event. In the sediments of the coastal plain this phase is recognized as the so called "Bauxite Hiatus" (Wong, 1994). Other important hiatuses occur at the Cretaceous-Tertiary boundary and near the base of the Miocene (Wong, 1986; Wong, 1994), and palynological results indicate that large parts of the Miocene are missing in the sedimentary record (Wymstra, 1971; Wong, 1986), supporting the existence of several weathering episodes during the Cenozoic.

In contrast, no reliable age data exists for the generally uncovered bauxites formed on top of the basement rocks of the Guiana shield and on top of the Cretaceous-Paleogene sediments of the Amazonas basin. Bardossy and Aleva (1990) propose a Late Cretaceous or Early Tertiary origin for several of them, but also mention, that they often seem to have a polyphase origin and that bauxitization might largely postdate lateritization and continue today.

The Late Eocene to Oligocene age of the coastal bauxites in Suriname and Guyana overlaps with our oldest ages and underlines the geological significance of the latter. However, this raises the question why in the coastal belt bauxites are produced whereas at Kaw ferruginous laterites are developed. While unequal precipitation could be one reason, differences in the drainage capacities due to the different parental material could also be responsible for this different evolution, as Bardossy and Aleva (1990) have shown that drainage is one of the key parameters controlling bauxite formation, whereas parental rock composition plays a subordinate role (Schellmann, 1994). The bauxites of the coastal belt are generally on top of highly permeable arkosic sandstones which are possibly better drained than the shists of the Paramaca formation at Kaw. As explained in section 6.3, the (U-Th)/He ages of the Fe oxyhydroxides are minimum estimates for the onset of alteration. It is thus possible that lateritic (but not bauxitic) cover of Kaw mountain developed isochronal to the coastal bauxites in the neighboring country.

6.5. Implications for the regional climate and geology

Our results show that tropical climate, allowing the formation of laterite, exists at Kaw since at least 30 Ma. As the late Neogene bauxitization event had a strong impact on the preexisting Fe-duricrust, we cannot say if these conditions have lasted continuously since then or not. The peak of maximum subsample ages at 12–14 Ma suggests that favorable conditions existed during the Middle Miocene. From 30 to 12 Ma the climate might have been more seasonally contrasted tropical climate, as lateritic duricrust, but not bauxitic duricrust was formed. The distribution of hematite and goethite suggests that there might have been a transition from hotter and dryer to more humid and/or eventually cooler seasonally contrasted tropical climate during this period.

Bardossy and Aleva (1990) have shown that the formation of lateritic bauxites requires some specific conditions when compared to ferruginous laterites. These are notably a humid tropical monsoonal climate and very good drainage conditions. The shift to increasing bauxitic conditions observed in our samples potentially indicates change in local climate including better drainage conditions in the Late Neogene.

Due to the lack of lake sediments or carbonates little is known about the climatic variations in Amazonia throughout the last Myr. However, the major geological changes which affected the area throughout the Cenozoic, notably several uplift episodes of the Andes (Rodríguez Tribaldos et al., 2017) and the closure of the Panama isthmus (Coates, 1992; Bartoli et al., 2005), have potentially influenced the regional climate. While temperatures might have been more or less stable due to the position in tropical latitudes with variations mainly connected to global temperature variations, precipitation patterns might have changed more significantly. Studies of the current climate of the Gui-

anas show that the area is subject to a rather complex precipitation pattern with considerable small-scale variation whereas temperatures show less variation (Bovolo et al., 2012; Ringard et al., 2015). The intensity increase of weathering processes observed in our dataset since the end of the Neogene indicates probably an increase in precipitation. On the one hand, enhanced precipitation could be a local feature. Nowadays the area of Kaw mountain is the area with the highest precipitations in French Guiana. This pattern might have been set in place at the end of the Neogene. On the other hand, there could have been a more regional change in precipitation patterns in Amazonia possibly related to the closure of the Panama Isthmus at ca. 3.5–2.7 Ma (Coates, 1992; Bartoli et al., 2005) with influence on oceanic currents and wind pattern in the area or to the mid-Pliocene Warm Period. The results from Western Amazonia (Allard et al., 2018; Mathian et al., 2020) yielding similar weathering ages support this possibility.

Improvement of the drainage conditions (Bardossy and Aleva, 1990) could additionally have intensified the weathering processes at Kaw in the late Neogene. Due to the already developed weathering mantle, the permeability of the parental material was likely increased. Bardossy and Aleva (1990) describe that bauxites occur mainly on highly dissected plateaus, but the temporal relationship of incision and bauxitization is not totally clear. Augmented incision inducing better drainage could have been triggered by relative movements of the continent (uplift) or the sea level (drop). With the Miocene transcontinentalization of the Amazon river, sediments from the Andes started to deposit in the Amazon fan from around 11 Ma (Figueiredo et al., 2009; Hoorn et al., 2017). In a short period of time, mainly since 6.8 Ma and even more since 2.4 Ma, huge masses of sediments have been deposited in the fan (>4000 m), leading to an enormous weight pushing down the plate (Figueiredo et al., 2009). Flexural uplift owing to this sediment loading on the margin was suggested by Figueiredo et al. (2009) and Sapin et al. (2016). The bauxitization event, which could have lasted several Myr or less, could therefore be linked to increased uplift of the Guyana shield. A coupled process with uplift leading to locally increased precipitation due to change of the relief could also have possibly triggered the bauxitization process. Comparative studies at other sites would be needed in order to find an answer to this question.

7. CONCLUSIONS

Our new data shed light onto an area so far only poorly constrained by weathering geochronology. The lateritic bauxitic cover of Kaw Mountain (French Guiana) records weathering since at least the Oligocene. The oldest Fe minerals dated in this study formed during or after kaolinite formation under ferruginous lateritic (not aluminous lateritic) conditions ca. 30 Ma ago. Ferruginous lateritic conditions with precipitation of hematite and Al-poor goethite and stability of kaolinite prevailed during the Early and Middle Miocene. Precipitation of Fe-minerals became more common at 14–10 Ma. Increase in phase mixing, Fe-Al-substitution in goethite, Th concentration and Th/U ratio as well as gibbsite precipitation imply an intensification of the weathering conditions during the Late Miocene, the Pliocene and Early Pleistocene, starting at ca. 10 Ma with a peak at 6–2 Ma. We assume that this intensification of weathering is responsible for the bauxitization of the weathering surface of Kaw mountain. The Th and U rich Fe minerals formed during this late stage of intense weathering got mixed with the preexisting Fe minerals leading to a strong spreading of the bulk (U-Th)/He ages.

Comparison with nearby bauxites indicates that the onset of weathering at Kaw could have been synchronous to the formation of the coastal bauxites in Suriname and Guyana. The different intensity of the Paleogene weathering which produced bauxites on top of the sedimentary rocks in Suriname and Guyana and ferruginous lateritic cover on top of the basement rocks at Kaw might be due to the different drainage capacities of the parental material.

The Late Neogene bauxitization event that we observe in our data has not yet been described in the area. Bauxitization at Kaw could have been caused either by a regional or global change in precipitation, possibly by flexural uplift owing to sedimentary loading in the Amazon fan leading to increased incision and thus increased drainage, or a combination of these processes with uplift leading to changes in the local precipitation pattern. Finally, this study reveals that climatic signal hidden in ferruginous laterite and bauxite could be revealed by combining geochronological results with mineralogical and geochemical analyses.

Declaration of Competing Interest

The authors declare that they have no known competing financial interests or personal relationships that could have appeared to influence the work reported in this paper.

ACKNOWLEDGEMENTS

This work was funded and carried out in the framework of the French funding Agency ANR RECA-ANR-17-CE01-0012-01 project and the BRGM-TOTAL project Source-to-Sink. Frédéric Haurine and Pierre Burckel are warmly thanked for the ICP-MS analysis, Ludovic Delbes and Benoît Baptiste for support with XRD analyses and Imène Esteve for help with SEM analyses. The editor Jeffrey Catalano, Florian Hofmann and two anonymous reviewers helped to improve this manuscript with their constructive comments.

APPENDIX A. SUPPLEMENTARY DATA

Supplementary data containing 13 figures and 5 tables associated with this article can be found online at https://doi.org/10.1016/j.gca.2022.02.017.

REFERENCES

Aleva G. J. J. (1981) Essential differences between the Bauxite Deposits along the Southern and Northern Edges of the Guiana Shield, South America. *Econ. Geol.* **76**, 1142–1152.

Aleva G. J. J. (1984) Lateritization, bauxitization and cyclic landscape development in the Guiana Shield. In *Bauxite* (ed. L. Jacob). A.I.M.E, New York, USA, pp. 297–318.

Allard T., Gautheron C., Bressan Riffel S., Balan E., Soares B. F., Pinna-Jamme R., Derycke A., Morin G., Bueno G. T. and do Nascimento N. (2018) Combined dating of goethites and kaolinites from ferruginous duricrusts. Deciphering the Late Neogene erosion history of Central Amazonia. *Chem. Geol.* **479**, 136–150.

Baker P. A., Fritz S. C., Silva C. G., Rigsby C. A., Absy M. L., Almeida R. P., Caputo M., Chiessi C. M., Cruz F. W., Dick C. W., Feakins S. J., Figueiredo J., Freeman K. H., Hoorn C., Jaramillo C., Kern A. K., Latrubesse E. M., Ledru M. P., Marzoli A., Myrbo A., Noren A., Piller W. E., Ramos M. I. F., Ribas C. C., Trnadade R., West A. J., Wahnfried I. and Willard D. A. (2015) Trans-Amazon Drilling Project (TADP): Origins and evolution of the forests, climate, and hydrology of the South American tropics. *Sci. Drill.* **20**, 41–49.

Balan E., Allard T., Fritsch E., Sélo M., Falguères C., Chabaux F., Pierret M. C. and Calas G. (2005) Formation and evolution of lateritic profiles in the middle Amazon basin: Insights from radiation-induced defects in kaolinite. *Geochim. Cosmochim. Acta* **69**, 2193–2204.

Balout H., Roques J., Gautheron C., Tassan-Got L. and Mbongo-Djimbi D. (2017) Helium diffusion in pure hematite (α-Fe_2O_3) for thermochronometric applications: A theoretical multi-scale study. *Comput. Theor. Chem.* **1099**, 21–28.

Bardossy G. and Aleva G. J. J. (1990). *Lateritic Bauxites*. Elsevier Science, Amsterdam, The Netherlands.

Bartoli G., Sarnthein M., Weinelt M., Erlenkeuser H., Garbe-Schönberg D. and Lea D. W. (2005) Final closure of Panama and the onset of northern hemisphere glaciation. *Earth Planet. Sci. Lett.* **237**, 33–44.

Beauvais A. (2009) Ferricrete biochemical degradation on the rainforest-savannas boundary of Central African Republic. *Geoderma* **150**, 379–388.

Beauvais A. (1999) Geochemical balance of lateritization processes and climatic signatures in weathering profiles overlain by ferricretes in Central Africa. *Geochim. Cosmochim. Acta* **63**, 3939–3957.

Beauvais A. and Colin F. (1993) Formation and transformation processes of iron duricrust systems in tropical humid environment. *Chem. Geol.* **106**, 77–101.

Beauvais A., Ruffet G., Hénocque O. and Colin F. (2008) Chemical and physical erosion rhythms of the West African Cenozoic morphogenesis: The ^{39}Ar-^{40}Ar dating of supergene K-Mn oxides. *J. Geophys. Res. Earth Surf.* **113**, 1–15.

Beck H. E., Zimmermann N. E., McVicar T. R., Vergopolan N., Berg A. and Wood E. F. (2018) Present and future köppen-geiger climate classification maps at 1-km resolution. *Sci. Data* **5**, 1–12.

Berar J. F. and Baldinozzi G. (1998) XND code: From X-ray laboratory data to incommensurately modulated phases. *Rietveld Model. Complex Mater. CPD Newsl.* **20**, 3–5.

Bish D. L. and Von Dreele R. B. (1989) Rietveld refinement of non-hydrogen atomic positions in kaolinite. *Clays Clay Miner.* **37**, 289–296.

Blake R. L., Hessevick R. E., Zoltai T. and Finger L. W. (1966) Refinement of the hematite structure. *Am. Mineral. J. Earth Planet. Mater.* **51**, 123–129.

Blancaneaux P. (1981). *Essai sur le milieu naturel de la Guyane Française*. ORSTOM, Paris.

Bovolo C. I., Pereira R., Parkin G., Kilsby C. and Wagner T. (2012) Fine-scale regional climate patterns in the Guianas, tropical South America, based on observations and reanalysis data. *Int. J. Climatol.* **32**, 1665–1689.

Braun J. J., Pagel M., Herbilln A. and Rosin C. (1993) Mobilization and redistribution of REEs and thorium in a syenitic lateritic profile: A mass balance study. *Geochim. Cosmochim. Acta* **57**, 4419–4434.

Briceño H. O. and Schubert C. (1990) Geomorphology of the Gran Sabana, Guayana Shield, southeastern Venezuela. *Geomorphology* **3**, 125–141.

Bruno J., De Pablo J., Duro L. and Figuerola E. (1995) Experimental study and modeling of the U(VI)-Fe$(OH)_3$ surface precipitation/coprecipitation equilibria. *Geochim. Cosmochim. Acta* **59**, 4113–4123.

Carvalho A., Boulangé B., Melfi A. J. and Lucas Y. (1997) *Brazilian Bauxites*. eds. A. Carvalho, B. Boulangé, A. J. Melfi, and Y. Lucas, USP, FAPESP, ORSTOM, São Paulo, Paris.

Choubert B. (1957) Essai sur la morphologie de la Guyane. Imprimerie Nationale, Paris.

Choubert B. (1956) Les Gisements de bauxite de la Guyane Française. ORSTOM, Paris, p. 15.

Coates A. G. (1992) Closure of the Isthmus of Panama: the near-shore marine record of Costa Rica and western Panama. *Geol. Soc. Am. Bull.* **104**, 814–828.

Corbató C. E., Tettenhorst R. T. and Christoph G. G. (1985) Structure refinement of deuterated boehmite. *Clays Clay Miner.* **33**, 71–75.

Cordani U. G. and Teixeira W. (2007) Proterozoic accretionary belts in the Amazonian Craton. In *4-D Framework of Continental Crust: Geological Society of America Memoir 200* (eds. R. D. J. Hatcher, M. P. Carlson, J. H. McBride and J. Martínez-Catalán). Geological Society of America, Boulder, CO, pp. 297–320.

Cromer D. T. (1983) Calculation of anomalous scattering factors at arbitrary wavelengths. *J. Appl. Crystallogr.* **16**, 437.

Danišík M., Evans N. J., Ramanaidou E. R., McDonald B. J., Mayers C. and McInnes B. I. A. (2013) (U-Th)/He chronology of the Robe River channel iron deposits, Hamersley Province, Western Australia. *Chem. Geol.* **354**, 150–162.

Delor C., Lahondère D., Egal E., Lafon J. M., Cocherie A., Guerrot C., Rossi P., Truffert C., Théveniaut H., Phillips D. and Avelar V. G. de (2003) Transamazonian crustal growth and reworking as revealed by the 1:500,000-scale geological map of French Guiana (2nd edition). *Geol. la Fr.* **2-3-4**, 5–57.

Deng X. D., Li J. W. and Shuster D. L. (2017) Late Mio-Pliocene chemical weathering of the Yulong porphyry Cu deposit in the eastern Tibetan Plateau constrained by goethite (U–Th)/He dating: Implication for Asian summer monsoon. *Earth Planet. Sci. Lett.* **472**, 289–298.

Derycke A., Gautheron C., Barbarand J., Bourbon P., Aertgeerts G., Simon-Labric T., Sarda P., Pinna-Jamme R., Boukari C. and Haurine F. (2021) French Guiana margin evolution: From Gondwana break-up to Atlantic opening. *Terra Nov.*, 1–8.

Dublet G., Juillot F., Morin G., Fritsch E., Fandeur D. and Brown G. E. (2015) Goethite aging explains Ni depletion in upper units of ultramafic lateritic ores from New Caledonia. *Geochim. Cosmochim. Acta* **160**, 1–15.

Farley K. A. (2002) (U-Th) / He dating: techniques, calibrations, and applications. *Rev. Mineral. Geochem.* **47**, 819–844.

Farley K. A. (2018) Helium diffusion parameters of hematite from a single-diffusion-domain crystal. *Geochim. Cosmochim. Acta* **231**, 117–129.

Farley K. A., Wolf R. A. and Silver L. T. (1996) The effects of long alpha-stopping distances on (U-Th)/He ages. *Geochim. Cosmochim. Acta* **60**, 4223–4229.

Fedorov A. V., Brierley C. M., Lawrence K. T., Liu Z., Dekens P. S. and Ravelo A. C. (2013) Patterns and mechanisms of early Pliocene warmth. *Nature* **496**, 43–49.

Figueiredo J., Hoorn C., van der Ven P. and Soares E. (2009) Late Miocene onset of the Amazon River and the Amazon deep-sea fan: Evidence from the Foz do Amazonas Basin. *Geology* **37**, 619–622.

Fitzpatrick R. W. and Schwertmann U. (1982) Al-substituted goethite—An indicator of pedogenic and other weathering environments in South Africa. *Geoderma* **27**, 335–347.

Flower B. P. (1999) Warming without high CO_2?. *Nature* **399** 313–314.

Forsyth J. B., Hedley I. G. and Johnson C. E. (1968) The magnetic structure and hyperfine field of goethite (α-FeOOH). *J. Phys. C Solid State Phys.* **1**, 179.

Fritsch E., Morin G., Bedidi A., Bonnin D., Balan E., Caquineau S. and Calas G. (2005) Transformation of haematite and Al-poor goethite to Al-rich goethite and associated yellowing in a ferralitic clay soil profile of the middle Amazon Basin (Manaus, Brazil). *Eur. J. Soil Sci.* **56**, 575–588.

Gautheron C., Pinna Jamme R., Derycke, A. A., Hadi F., Sanchez C., Haurine F., Monvoisin G., Barbosa D., Delpech G., Maltese J., Sarda P. and Tassan-Got L. (2021) Analytical protocols and performance for apatite and zircon (U-Th)/He analysis on quadrupole and magnetic sector mass spectrometer systems between 2007 and 2020. *Geochronology*.

Gautheron C., Tassan-Got L., Ketcham R. A. and Dobson K. J. (2012) Accounting for long alpha-particle stopping distances in (U-Th-Sm)/He geochronology: 3D modeling of diffusion, zoning, implantation, and abrasion. *Geochim. Cosmochim. Acta* **96**, 44–56.

Gómez J., Schobbenhaus C., Montes N. E. and Compilers (2019) *Geological Map of South America 2019. Scale 1:5 000 000.*,

Groussin J. (2001) Le Climat Guyanais. In *Atlas illustré de la Guyane* (ed. J. Barret). Laboratoire de Cartographie de la Guyane; Institut d'Enseignement Superieur de Guyane. pp. 46–49.

Hammen van der T. and Wymstra T. A. (1964) A Palnyological study on the Tertiary and Upper Cretaceous of British Guiana. *Leidse Geol. Meded.* **30**, 183–241.

Hammersley A. P. (2016) FIT2D: a multi-purpose data reduction, analysis and visualization program. *J. Appl. Crystallogr.* **49**, 646–652.

Haywood A. M., Hill D. J., Dolan A. M., Otto-Bliesner B. L., Bragg F., Chan W. L., Chandler M. A., Contoux C., Dowsett H. J., Jost A., Kamae Y., Lohmann G., Lunt D. J., Abe-Ouchi A., Pickering S. J., Ramstein G., Rosenbloom N. A., Salzmann U., Sohl L., Stepanek C., Ueda H., Yan Q. and Zhang Z. (2013) Large-scale features of Pliocene climate: Results from the Pliocene Model Intercomparison Project. *Clim. Past* **9**, 191–209.

Heim J. A., Vasconcelos P. M., Shuster D. L., Farley K. A. and Broadbent G. (2006) Dating paleochannel iron ore by (U-Th)/He analysis of supergene goethite, Hamersley province, Australia. *Geology* **34**, 173–176.

Herold N., Huber M. and Müller R. D. (2011) Modeling the miocene climatic optimum. Part I: Land and atmosphere. *J. Clim.* **24**, 6353–6373.

Hofmann F., Reichenbacher B. and Farley K. A. (2017) Evidence for >5 Ma paleo-exposure of an Eocene-Miocene paleosol of the Bohnerz Formation, Switzerland. *Earth Planet. Sci. Lett.* **465**, 168–175.

Hofmann F., Treffkorn J. and Farley K. A. (2020) U-loss associated with laser-heating of hematite and goethite in vacuum during (U-Th)/He dating and prevention using high O_2 partial pressure. *Chem. Geol.*, 532.

Hoorn C., Bogotá-A G. R., Romero-Baez M., Lammertsma E. I., Flantua S. G. A., Dantas E. L., Dino R., do Carmo D. A. and Chemale F. (2017) The Amazon at sea: Onset and stages of the Amazon River from a marine record, with special reference to Neogene plant turnover in the drainage basin. *Glob. Planet. Change* **153**, 51–65.

Hoorn C., Roddaz M., Dino R., Soares E., Uba C., Ochoa-Lozano D., Mapes R. (2010) The Amazonian craton and its influence on past flunival systems (Mesozoic-Cenozoic, Amazonia). In *Amazonia: landscape and species evolution. A look into the past*. Hoorn C. and Wesselingh F.P. (Eds). Wiley-Blackwell. 103-122

Hoorn C., Wesselingh F. P., ter Steege H., Bermudez M. A., Mora A., Sevink J., Sanmartín I., Sanchez-Meseguer A., Anderson C. L., Figueiredo J. P., Jaramillo C., Riff D., Negri F. R., Hooghiemstra H., Lundberg J., Stadler T., Särkinen T. and Antonelli A. (2010b) Amazonia Through Time : Andean Uplift, Climate Change, Landscape Evolution and Biodiversity. *Science.* **330**, 927–931.

Horn M. S. C. F., Schwebdtfeger C. F. and Meagher E. P. (1972) Refinement of the structure of anatase at several temperatures. *Zeitschrift für Krist. Mater.* **136**, 273–281.

Hsi C.-K. D. and Langmuir D. (1985) Adsorption of uranyl onto ferric oxyhydroxides: Application of the surface complexation site-binding model. *Geochim. Cosmochim. Acta* **49**, 1931–1941.

Ketcham R. A., Gautheron C. and Tassan-Got L. (2011) Accounting for long alpha-particle stopping distances in (U-Th-Sm)/He geochronology: Refinement of the baseline case. *Geochim. Cosmochim. Acta* **75**, 7779–7791.

King L. C. (1962) Morphology of the Earth: A Study and Synthesis of World Scenery. Oliver and Boyd Publ. House, Edinburgh and London, p. 699 p..

Leprieur (1848) Exploration géologique du bassin de la Comté (Guyane Française). *Bull. la Société Géologique la Fr.* **5**, 251–254.

Lippolt H. J., Brander T. and Mankopf N. R. (1998) An attempt to determine formation ages of goethites and limonites by (U+Th)-^{4}He dating. *Neues Jahrb. Mineral. Monatshefte*, 11.

Manceau A., Charlet L., Boisset M. C., Didier B. and Spadini L. (1992) Sorption and speciation of heavy metals on hydrous Fe and Mn oxides. From microscopic to macroscopic. *Appl. Clay Sci.* **7**, 201–223.

Mathian M., Bueno G. T., Balan E., Fritsch E., Do Nascimento N. R., Selo M. and Allard T. (2020) Kaolinite dating from Acrisol and Ferralsol: A new key to understanding the landscape evolution in NW Amazonia (Brazil). *Geoderma* **370**.

McConnell R. B. (1968) Planation Surfaces in Guyana. *Geogr. J.* **134**, 506–520.

Meinhold G. (2010) Rutile and its applications in earth sciences. *Earth-Sci. Rev.* **102**, 1–28.

Mendes A. C., Truckenbrod W. and Nogueira A. C. R. (2012) Análise faciológica da formação Alter do Chão (Cretáceo, Bacia do Amazonas), próximo à cidade de Óbidos, Pará, Brasil. *Rev. Bras. Geociencias* **42**, 39–57.

Monsels D. A. and Van Bergen M. J. (2019) Bauxite formation on Tertiary sediments in the coastal plain of Suriname. *J. South Am. Earth Sci.* **89**, 275–298.

Monteiro H. S., Vasconcelos P. M., Farley K. A., Spier C. A. and Mello C. L. (2014) (U-Th)/He geochronology of goethite and the origin and evolution of cangas. *Geochim. Cosmochim. Acta* **131**, 267–289.

Monteiro H. S., Vasconcelos P. M. P., Farley K. A. and Lopes C. A. M. (2018) Age and evolution of diachronous erosion surfaces in the Amazon: Combining (U-Th)/He and cosmogenic ^{3}He records. *Geochim. Cosmochim. Acta* **229**, 162–183.

Nahon D. (1991) Introduction to the petrology of soils and chemical weathering. Wiley, New York, USA.

Palmer R. B. J. and Akhavan-Rezayat A. (1978) The stopping power of water, water vapour and aqueous tissue equivalent

solution for alpha particles over the energy range 0.5-8 MeV. *J. Phys. D. Appl. Phys.* **11**, 605–616.

Patterson S. H., Kurtz H. F., Olson J. C. and Neeley C. L. (1994) World Bauxite Resources - Geology and Resources of Aluminum. U.S. Geolo., U.S. Geological Survey, Washington.

Pidgeon R. T. (2003) Application of (U-Th)/ He Geochronology To Date Hematite and Other Iron Minerals Produced During Weathering. *Advances*, 321–323.

Pidgeon R. T., Brander T. and Lippolt H. J. (2004) Late Miocene (U+Th)-^{4}He ages of ferruginous nodules from lateritic duricrust, Darling Range, Western Australia. *Aust. J. Earth Sci.* **51**, 901–909.

Pontes G. M., Wainer I., Taschetto A. S., Sen Gupta A., Abe-Ouchi A., Brady E. C., Le Chan W., Chandan D., Contoux C., Feng R., Hunter S. J., Kame Y., Lohmann G., Otto-Bliesner B. L., Peltier W. R., Stepanek C., Tindall J., Tan N., Zhang Q. and Zhang Z. (2020) Drier tropical and subtropical Southern Hemisphere in the mid-Pliocene Warm Period. *Sci. Rep.* **10**, 1–11.

Prasad G. (1983) A review of the early Tertiary bauxite event in South America, Africa and India. *J. African Earth Sci.* **1**, 305–313.

Putzer H. (1984) The geological evolution of the Amazon basin and its mineral resources. In *The Amazon: Limnology and Landscape Ecology of a Mighty Tropical River and its Basin* (ed. H. Sioli). Dr W. Junk Publishers, Dordrecht, pp. 15–46.

Reiners P. W., Chan M. A. and Evenson N. S. (2014) (U-Th)/He geochronology and chemical compositions of diagenetic cement, concretions, and fracture-filling oxide minerals in mesozoic sandstones of the Colorado Plateau. *Bull. Geol. Soc. Am.* **126**, 1363–1383.

Riffel S. B., Vasconcelos P. M., Carmo I. O. and Farley K. A. (2015) Combined ^{40}Ar/^{39}Ar and (U-Th)/He geochronological constraints on long-term landscape evolution of the Second Paraná Plateau and its ruiniform surface features, Paraná, Brazil. *Geomorphology* **233**, 52–63.

Riffel S. B., Vasconcelos P. M., Carmo I. O. and Farley K. A. (2016) Goethite (U–Th)/He geochronology and precipitation mechanisms during weathering of basalts. *Chem. Geol.* **446**, 18–32.

Ringard J., Becker M., Seyler F. and Linguet L. (2015) Temporal and spatial assessment of four satellite rainfall estimates over French Guiana and north Brazil. *Remote Sens.* **7**, 16441–16459.

Rodríguez Tribaldos V., White N. J., Roberts G. G. and Hoggard M. J. (2017) Spatial and temporal uplift history of South America from calibrated drainage analysis. *Geochem. Geophys. Geosystems* **18**, 2321–12153.

Rudnick R. L. and Gao S. (2013) Composition of the Continental Crust, 2nd ed.,. Elsevier Ltd..

Ruffet G., Innocent C., Michard A., Féraud G., Beauvais A., Nahon D. and Hamelin B. (1996) A geochronological ^{40}Ar/^{39}-Ar and ^{87}Rb/^{87}Sr study of K-Mn oxides from the weathering sequence of Azul, Brazil. *Geochim. Cosmochim. Acta* **60**, 2219–2232.

Saalfeld H. and Wedde M. (1974) Refinement of the crystal structure of gibbsite, $Al(OH)_3$. *Zeitschrift für Krist. Mater.* **139**, 129–135.

dos Santos Albuquerque M. F., Horbe A. M. C. and Danišík M. (2020) Episodic weathering in Southwestern Amazonia based on (U–Th)/He dating of Fe and Mn lateritic duricrust. *Chem. Geol.* **553**, 119792.

Sapin F., Davaux M., Dall'asta M., Lahmi M., Baudot G. and Ringenbach J.-C. (2016) Post-rift subsidence of the French Guiana hyper-oblique margin: From rift-inherited subsidence to Amazon deposition effect. *Geol. Soc. Spec. Publ.* **431**, 125–144.

Schellmann W. (1994) Geochemical differentiation in laterite and bauxite formation. *Catena* **21**, 131–143.

Schulze D. G. (1984) The influence of aluminium on iron oxides. VIII. Unit-cell dimensions of Al-substituted goethites and estimation of Al from them. *Clays Clay Miner.* **32**, 36–44.

Shintani H., Sato S. and Saito Y. (1975) Electron-density distribution in rutile crystals. *Acta Crystallogr. Sect. B Struct. Crystallogr. Cryst. Chem.* **31**, 1981–1982.

Shuster D. L., Farley K. A., Vasconcelos P. M., Balco G., Monteiro H. S., Waltenberg K. and Stone J. O. (2012) Cosmogenic ^{3}He in hematite and goethite from Brazilian "canga" duricrust demonstrates the extreme stability of these surfaces. *Earth Planet. Sci. Lett.* **329–330**, 41–50.

Shuster D. L., Vasconcelos P. M., Heim J. A. and Farley K. A. (2005) Weathering geochronology by (U-Th)/He dating of goethite. *Geochim. Cosmochim. Acta* **69**, 659–673.

Snyder D. B. and Bish D. L. (1989) Quantitative anallysis. *Mineral. Soc. Am. Rev. Mineral.* **20**, 101–144.

Stanjek H. and Schwertmann U. (1992) The influence of aluminum on iron oxides. Part XVI: Hydroxyl and aluminum substitution in synthetic hematites. *Clays Clay Miner.* **40**, 347–354.

Sundell K. E., Saylor J. E., Lapen T. J. and Horton B. K. (2019) Implications of variable late Cenozoic surface uplift across the Peruvian central Andes. *Sci. Rep.* **9**, 1–12.

Tardy Y. (1997). *Petrology of Laterites and Tropical Soils*. Balkema, Rotterdam, The Netherlands.

Tardy Y., Kobilsek B. and Paquet H. (1991) Mineralogical composition and geographical distribution of African and Brazilian periatlantic laterites. The influence of continental drift and tropical paleoclimates during the past 150 million years and implications for India and Australia. *J. African Earth Sci.* **12**, 283–295.

Tardy Y. and Nahon D. (1985) Geochemistry of laterites, stability of Al-goethite, Al-hematite, and Fe^{3+}-Kaolinite in bauxites and ferricretes: an approach to the mechanism of concretion formation. *Am. J. Sci.* **285**, 865–903.

Tardy Y. and Roquin C. (1998). *Dérive des continents paléoclimats et altérations tropicales*. BRGM, Orléans, France.

Théveniaut H. and Freyssinet P. (1999) Paleomagnetism applied to lateritic profiles to assess saprolite and duricrust formation processes: The example of Mont Baduel profile (French Guiana). *Palaeogeogr. Palaeoclimatol. Palaeoecol.* **148**, 209–231.

Théveniaut H. and Freyssinet P. (2002) Timing of lateritization on the Guiana Shield synthesis of paleomagnetic results. *Palaeogeogr. Palaeoclimatol. Palaeoecol.* **178**, 91–117.

Toby B. H. (2006) R factors in Rietveld analysis: How good is good enough? *Powder Diffr.* **21**, 67–70.

Trolard F. and Tardy Y. (1987) The stabilities of gibbsite, boehmite, aluminous goethites and aluminous hematites in bauxites, ferricretes and laterites as a function of water activity, temperature and particle size. *Geochim. Cosmochim. Acta* **51**, 945–957.

Valeton I. (1972). *Bauxites, Developments in Soil Sciences*. Elsevier, Amsterdam, The Netherlands.

Valeton I. (1999) Saprolite-bauxite facies of ferralitic duricrust on paleosurfaces of former Pangaea. In *Palaeoweathering, Palaeosurfaces and Related Continental Deposits* (eds. M. Thiry and R. Simon-Coiçon). Blackwell Science Ltd., pp. 153–188.

Vasconcelos P. M. (1999) K-Ar and ^{40} Ar / ^{39} Ar Geochronology of weathering processes. *Annu. Rev. Earth Planet. Sci.* **27**, 183–229.

Vasconcelos P. M. and Carmo I. de O. (2018) Calibrating denudation chronology through 40Ar/39Ar weathering geochronology. *Earth-Science Rev.* **179**, 411–435.

Vasconcelos P. M., Farley K. A., Stone J., Piacentini T. and Fifield L. K. (2019) Stranded landscapes in the humid tropics: Earth's oldest land surfaces. *Earth Planet. Sci. Lett.* **519**, 152–164.

Vasconcelos P. M., Heim J. A., Farley K. A., Monteiro H. and Waltenberg K. (2013) $^{40}Ar/^{39}Ar$ and (U-Th)/He -$^{4}He/^{3}He$ geochronology of landscape evolution and channel iron deposit genesis at Lynn Peak. *Western Australia. Geochim. Cosmochim. Acta* **117**, 283–312.

Vasconcelos P. M., Reich M. and Shuster D. L. (2015) The paleoclimatic signatures of supergene metal deposits. *Elements* **11**, 317–322.

Vasconcelos P. M., Renne P. R., Brimhall G. H. and Becker T. A. (1994) Direct dating of weathering phenomena by^{40}Ar / ^{39}Ar and K-Ar analysis of supergene K-Mn oxides. *Geochim. Cosmochim. Acta* **58**, 1635–1665.

Vermeesch P., Seward D., Latkoczy C., Wipf M., Günther D. and Baur H. (2007) α-Emitting mineral inclusions in apatite, their effect on (U-Th)/He ages, and how to reduce it. *Geochim. Cosmochim. Acta* **71**, 1737–1746.

Wells M. A., Danišík M., McInnes B. I. A. and Morris P. A. (2019) (U-Th)/He-dating of ferruginous duricrust: Insight into laterite formation at Boddington. *WA. Chem. Geol.* **522**, 148–161.

Wolska E. and Schwertmann U. (1993) The mechanism of solid solution formation between goethite and diaspore. *Neues Jahrb. für Mineral. Monatshefte* **5**, 213–223.

Wong T. (1994) The Paleocene-Eocene succession in the Guiana Basin. *Bull. la Société belge Géologie* **T.103**, 281–291.

Wong T. E. (1986) Outline of the stratigraphy and the geological history of the Suriname coastal plain. *Geol. en Mijnb.* **65**, 223–241.

Wymstra T. A. (1971) *The palnyology of the Guiana coastal basin*. University of Amsterdam.

Zachos J. C., Dickens G. R. and Zeebe R. E. (2008) An early Cenozoic perspective on greenhouse warming and carbon-cycle dynamics. *Nature* **451**, 279–283.

Associate editor: Jeffrey G. Catalano